Title
A Multiscale Analysis of Dynamic Wetting

Author
Minaki, Hiroyuki

Publication Date
2013

Peer reviewed|Thesis/dissertation

A Multiscale Analysis of Dynamic Wetting

by

Hiroyuki Minaki

A dissertation submitted in partial satisfaction of the
requirements for the degree of
Doctor of Philosophy

in

Mechanical Engineering

in the

Graduate Division

of the

University of California, Berkeley

Committee in charge:

Professor Tarek Zohdi, Chair
Professor Shaofan Li
Professor George Johnson

Spring 2013

A Multiscale Analysis of Dynamic Wetting

Abstract

A Multiscale Analysis of Dynamic Wetting

by

Hiroyuki Minaki

Doctor of Philosophy in Mechanical Engineering

University of California, Berkeley

Professor Tarek Zohdi, Chair

A computational multiscale Finite Element Method on dynamic wetting and droplet spreading on various substrates at micron scale is proposed. The model is formulated in the framework of large deformation continuum mechanics, and two different implementations are proposed to maintain the strain dependence of the surface stress.

We set forth a multiscale soft contact model and its Finite Element Method formulation for dynamic wetting, which includes an atomistic-based Coarse Grained Contact Model between the liquid and solid without using Molecular Dynamics, and the surface tension model along the contact interface allows droplet spreading due to the surface energy difference.

By employing the proposed method, we have successfully simulated droplet spreading, and our results compare well with the theoretical, experimental and Molecular Dynamics results. The results of the numerical simulation show that the proposed method is an efficient and viable computational tool for simulation of dynamic wetting, and it successfully removes the singularity problems that plague in most of macroscale hydrodynamics analysis of dynamic wetting and droplet spreading in the past.

Contents

List of Figures

List of Tables

Acknowledgments

I would like to express my gratitude to Professor Shaofan Li and Professor Tarek Zohdi for being such a helpful and understanding advisers. Their guidance and oversight over this research have been indispensable to its successful and timely conclusion of this dissertation.

I would like to thank my committee member, Professor George Johnson, for reviewing this dissertation closely and offering the time to many valuable discussions.

In addition, gratefully acknowledged are Professor David Steigmann, Professor Daryl C. Chrzan and Professor Per-Olof Persson for their insights into the subject and their valuable comments and suggestions on the directions of this research.

Chapter 1

Introduction

1.1 Motivation

Wetting and droplet spreading of a liquid on a solid substrate is an interesting and important chemical physics phenomenon, which has many important applications in the fields of nanotechnology, semiconductor and hard disk drives, oil and petroleum, transportation, rubbers, polymers and plastics, chemicals such as insecticides and detergents, pharmaceutical and biotechnology, among many others.

Wetting is the process of a liquid or liquid and gas phases concurrently interacting with the surface of a solid substrate, resulting from intermolecular interactions when the three are brought together. The degree of wetting is referred to as wettability, which is determined by the intermolecular force balance between adhesive, cohesive, or contact forces. Wetting has scientific importance when studying contact, bonding, or adherence of two materials. Wetting and the surface tension or surface energy that control wetting are also responsible for other related physical phenomena, such as droplet spreading, capillary rise, surfactant assembly, and wet friction, etc.

There are three types of molecular interactions at atomic scale in determining the equilibrium shape of a liquid droplet on a solid substrate: the liquid-gas interaction, the liquid-solid interaction, and the solid-gas interaction. The corresponding interaction energy, i.e. γ^{LG}, γ^{LS} and γ^{SG}, are called surface energy. In principle, the droplet will remain a droplet when the solid-gas interaction is weak compared to the liquid-solid interaction. On the other hand, the droplet spreads when the solid-gas interaction is strong, in order to maximize the contact area between the liquid so that the potential energy of the system is minimum. These relationships are expressed as the Young Equation in the equilibrium state [97],

$$\cos\theta = \frac{\gamma^{SG} - \gamma^{LS}}{\gamma^{LG}}, \tag{1.1}$$

where θ is called the contact angle that is defined as the angle between a solid surface and liquid-gas interface, shown in Figure 1.1.

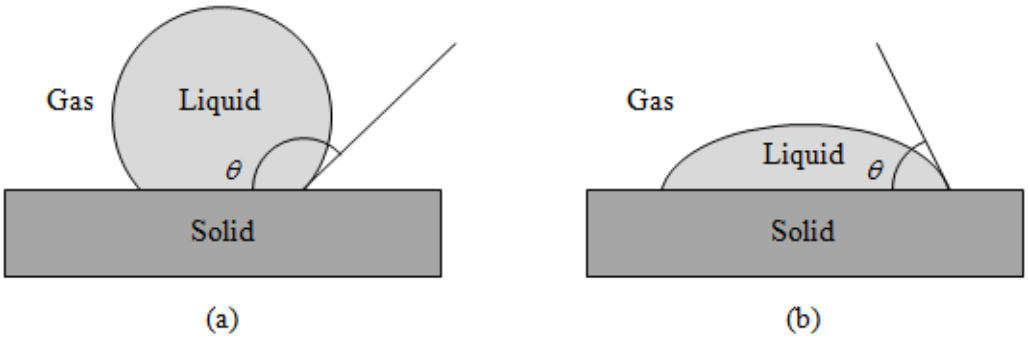

Figure 1.1: Wetting and droplet spreading: (a) Hydrophobic, (b) Hydrophilic.

One can see that the liquid droplet completely spreads out on the solid surface when the contact angle is equal to zero. The solid surface is considered as *hydrophillic* when the contact angle is smaller than 90°, and the solid surface is considered as *hydrophobic* when the contact angle is larger than 90°. In particular, the solid surface whose contact angle is larger than 150° is called superhydrophobic surface, which is extremely difficult to wet.

From a microscopic standpoint, wetting is due to the fact that molecular interaction between two different fluids on the free surface, or interface, which is a different environment than the same molecules within one fluid. Molecules of liquid considerably below the surface interact with each other by forces that are equal in all different directions. However, molecules near the surface have a greater attraction for each other than they do for molecules below the surface. This makes the liquid surface acting like a stretched membrane. Because of this membrane effect, each portion of the liquid surface exerts tension on adjacent portions of the surface or on objects that are in contact with the liquid surface. This tension force acts in the surface tangent plane of both the liquid and the solid, and its magnitude per unit length is defined as the surface tension [13], [72], [79], [83].

Molecular Dynamics [1], [14], [33], [69] has been used extensively as a simulation tool to study wetting and droplet spreading, and various simulations and modifications have been reported in the literature. Swol et al. [90] investigated a wetting transition at a fluid-wall interface for a system with strictly finite-range interactions by a constant-temperature Molecular Dynamics model. Sikkenk et al. [81] carried out computer simulations of a fluid adsorbed at a structured solid substrate with the Delft Molecular Dynamics Processor. Hautman et al. [35] show that two different surfaces exhibit qualitatively different wetting behavior which is characterized by a microscopic analog of the contact angle. Fan et al. [24] calculated the instantaneous contact angle from the microscopic structures of the droplet and the surface. Blake et al. [7] show that Molecular Dynamics allows a complete study of the dynamics of droplet spreading at the microscopic scale, for both complete and partial wetting regimes. However, most of these simulations focus on the scientific principles rather than engineering applications, because Molecular Dynamics is difficult to be applied to practical

applications in engineering design due to the computational expense, the time and size limitations.

For practical uses in engineering design, the Finite Element Method [4], [5], [36], [40] has also been applied to solve the wetting and droplet spreading problems. Fukai et al. [28] performed a theoretical study of the process of deformation of a spherical liquid droplet impinging upon a flat surface utilizing deforming finite elements and grid generation to simulate accurately the large deformations, as well as the domain nonuniformities characteristic of the spreading process. Madasu et al. [54] used the Arbitrary Lagrangian-Eulerian Finite Element Method and adaptive mesh motion to solve the problem of dynamic wetting on flexible substrates. Most hydrodynamics models of a moving contact line, which is defined as the intersection of the liquid-gas interface with the solid substrate, employ the non-slip boundary condition that leads to a singularity at the moving contact line, which forces the interface slip that in turn against the prior assumption. A number of theoretical investigations have been conducted to understand the number of the singularity and the contact line movement associated contact angle phenomena [18], [21], [22], [41], [59], [68], [89], [95]. The presence of this singularity poses great challenge in macroscale simulation of dynamic wetting and droplet spreading.

In this work, we present and study a systematic multiscale Finite Element Method on dynamic wetting and droplet spreading on various substrates. We set forth a multiscale soft contact model and its Finite Element Method formulation for dynamic wetting, which includes an atomistic-based Coarse Grained Contact Model [73], [74], [75], [76], [77] between the liquid and solid, and the surface tension model along the contact interface allows droplet spreading due to the surface energy difference. We develop a new multiscale method for wetting analysis, in which an accurate and efficient Coarse Grained Contact Model is adopted for studying the droplet spreading. By employing the proposed method, we have successfully simulated droplet spreading on a solid substrate, and our results compare well with the experiment, Molecular Dynamics and theoretical solutions. The results of the numerical simulation show that the proposed method is an efficient and viable computational tool for simulation of dynamic wetting at the macroscale, and it successfully removes the singularity problems that plague most previous macroscale hydrodynamics analyse of dynamic wetting and droplet spreading.

1.2 Examples

A wide variety of applications are concerned with wetting and droplet spreading. In engineering design, waterproofing is widely investigated in connection with coating based on hydrophobicity, for example, as shown in Figure 1.2 (a). Hydrophobicity creates a barrier of air on the surface, and it keeps clean the surface.

Superhydrophilicity is also commercialized in the engineering design, for example, the door mirror for cars, shown in Figure 1.2 (b). The coating spreads out rain droplets on the mirror surface into a thin film of water by a photo catalytic hydrophilic effect [34].

(a) (b)

Figure 1.2: (a) Waterproofing [1], (b) A door mirror: The left side is hydrophilic coating, and the right side is non-coating [2].

In bioengineering and the pharmaceutical industry, using wetting agent surfactants has become an effective approach to developing advanced or bio-inspired materials in drug delivery and targeting [99]. In fact, there are many other wetting phenomena in biology. An example of hydrophobicity in biology is the water strider, as shown in Figure 1.3 (a). Water striders are types of insects with the remarkable ability to stand effortlessly and walk quickly on water. The contact angle of water strider legs is grater than 120° [62]. Feng et al. [25] reported the watter repellency mechanism of water strider legs. Also, Suhr et al. [84] designed a robot that mimics the movement of the water strider.

Another example in biology and bioengineering involves the stem cell contact and spreading. Results with drug treatments of various cells on soft, stiff, and rigid matrices show a broad range of possible matrix-dependent drug responses, and cells on soft gels might be relatively unaffected in cell spreading or apoptosis induction, whereas cells on stiff substrates seem more sensitive to diverse drugs in terms of spreading [51], [52], [71], [99].

The ultimate objective of this research is to improve tire performance on wet and ice/snow roads, shown in Figure 1.4. In order to improve the tire performances, consideration of precise road conditions is required. In addition to the popular asphalt-paved road, there are various road conditions such as gravel, water, snow or ice covered conditions. The friction and adhesion between the tires and the road are strongly influenced by the wetting characteristic of the road and the tire. Cho et al. [10] reported the braking distance on the wet road is longer than the one on the dry road by 20%, and thus dynamic wetting has a strong influence on the friction between the wet surface and the tire. To understand the wetting phenomenon and its relation to wet friction and the hydrophobic property of tires, we can gain insight

[1]Image source: http://www.gadgetreview.com/2012/12/10-of-the-best-waterproof-iphone-5-cases.html
[2]Image source: http://item.rakuten.co.jp/auto-craft/10151997/

on vehicle/road wet friction in order to improve the tire performance on rainy days or other wet road conditions. In fact, contact on ice or snow covered roads is an important subject for the tire performance, because the road behaves both as a solid and as a liquid material depending on the temperature, pressure or other state variables. Since tire deformation is a macro-scale behavior, and the roughness of the road surfaces or the liquid-solid phase transition has nano-scale characteristics, the analysis of the interaction problem between the tire and the road requires a multi-scale analysis.

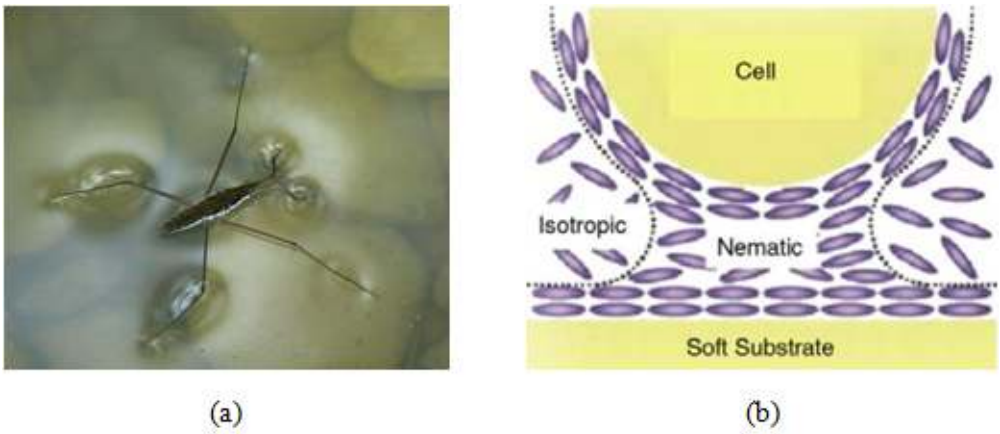

Figure 1.3: (a) A water strider [3], (b) A stem cell [99].

Figure 1.4: A tire [4].

[3]Image source: http://www.fcps.edu/islandcreekes/ecology/common_water_strider.htm
[4]Image source: http://www.gregoryhyundai.com/bridgestone-tires.cfm

1.3 Scope of the Dissertation

The next Chapter of this dissertation outlines a new surface tension model based on the definition of surface tension in the macroscopic regime, that is: the surface tension is the force along a line of unit length, where the force is parallel to the surface but perpendicular to the line. In particular, we focus on developing a finite element-based surface tension model.

In Chapter 3, we formulate and solve the wetting and droplet spreading problems on the rigid substrate based on the proposed surface tension model. Results for problems in equilibrium are consistent with the Young equation [97]. The implementations of the Finite Element Method in both two and three dimensions are also discussed.

In Chapter 4, we present a Galerkin weak formulation of the surface tension model based on the surface stress and surface deformation. Because the above method considers only the surface energy, it can be applied to only the rigid substrate. To simulate various deformable substrate, we construct a Galerkin weak form that takes into account the surface stress.

In Chapter 5, several constitutive models are illustrated, Here we first discuss the Cauchy-Born rule, [3], [23], [86], [98], which relates the stress state of a uniformly deformed crystalline solid to the change of lattice vectors. As the mesoscale constitutive models of the surface stress, we shall discuss the Gurtin-Murdoch surface elasticity model and the Surface Cauchy-Born rule [61], [63], [64], [65].

In Chapter 6, we introduce the Coarse Grained Contact Model as the contact method between the liquid and solid, and the efficient and high accuracy method which is the analytical integration method of the master body is investigated.

The last task, addressed in Chapter 7, is the validation of the proposed methods by numerical analysis compared with the experiment, Molecular Dynamics and theoretical solution. Also, the restrictions of the proposed method are investigated.

Finally, conclusions are drawn in Chapter 8.

Chapter 2

Surface Tension Models

In this chapter, we introduce a surface tension model for the Finite Element Method (FEM). In continuum mechanics, surface traction, which is a force vector on a cross-section divided by cross-section area, is applied to surfaces [26], [55], [87]. In this dissertation, we call this method as the surface traction method. To develop a multiscale computational method to solve dynamic wetting and droplet spreading problems at macroscale, a surface tension model for the Finite Element Method is proposed.

2.1 A Galerkin Finite Element Method Formulation in Continuum Mechanics

Before we discuss the FEM surface tension model, we briefly present the theory of a Galerkin Finite Element Method formulation in continuum mechanics [4], [5], [36], [40]. Consider a smooth deformable continuum body, as shown in Figure 2.1, that occupies the region Ω, with the boundary $\partial\Omega = \Gamma_u \cup \Gamma_q$ of the region Ω, where Γ_u is the Dirichlet boundary, and Γ_q is the Neumann boundary. The strong form of the equation of motion can

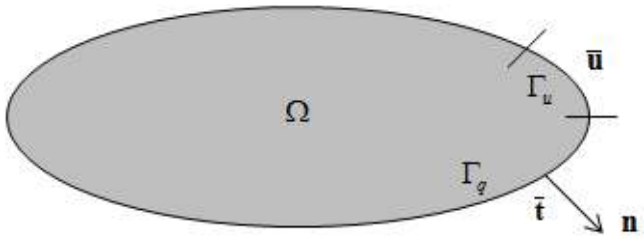

Figure 2.1: A smooth deformable continuum body that occupies the region Ω, with the boundary $\partial\Omega = \Gamma_u \cup \Gamma_q$ of the region Ω, where Γ_u is the Dirichlet boundary, and Γ_q is the Neumann boundary.

be expressed as

$$\begin{array}{rcll} div\boldsymbol{\sigma} + \rho\mathbf{b} & = & \rho\ddot{\mathbf{u}} & \text{in } \Omega, \\ \boldsymbol{\sigma}\cdot\mathbf{n} & = & \bar{\mathbf{t}} & \text{on } \Gamma_q, \\ \mathbf{u} & = & \bar{\mathbf{u}} & \text{on } \Gamma_u, \\ \mathbf{u}(0) & = & \mathbf{u}_0 & \text{in } \Omega, \\ \mathbf{v}(0) & = & \mathbf{v}_0 & \text{in } \Omega, \end{array} \tag{2.1}$$

where $\boldsymbol{\sigma}$ is the Cauchy stress, ρ is the mass density, $\mathbf{b}$ is the body force, $\mathbf{u}$ is the displacement, $\mathbf{n}$ is the normal vector, $\bar{\mathbf{t}}$ and $\bar{\mathbf{u}}$ are the prescribed surface traction and displacement fields, and $\mathbf{u}_0$ and $\mathbf{v}_0$ are the prescribed initial displacement and velocity.

The weak form of Equation (2.1) can be written as

$$\int_{\Omega_0} \mathbf{w}\cdot\rho_0\ddot{\mathbf{u}}d\Omega_0 = -\int_{\Omega_0} Div\mathbf{w} : \mathbf{P}d\Omega_0 + \int_{\Omega_0}\mathbf{w}\cdot\rho_0\mathbf{b}d\Omega_0 + \int_{\Gamma_{0q}}\mathbf{w}\cdot\bar{\mathbf{T}}d\Gamma_0, \tag{2.2}$$

where $\mathbf{w}$ is a vector test function, which belongs the Hilbert space $H^1(\Omega)$ and satisfies homogeneous boundary condition on the Dirichlet boundary Γ_u, ρ_0 is the density in the reference configuration, $\mathbf{P} = J\boldsymbol{\sigma}\mathbf{F}^{-T}$ is the first Piola-Kirchhoff stress, and $\bar{\mathbf{T}}$ is the pull-back traction vector on the reference boundary. This formulation is the so-called Galerkin weak formulation. Here, we define the single, double and triple contraction as

$$\mathbf{a}\cdot\mathbf{b} = \sum_i a_i b_i, \tag{2.3}$$

$$\mathbf{A} : \mathbf{B} = \sum_i\sum_j A_{ij}B_{ij}, \tag{2.4}$$

and

$$\mathcal{C}\vdots\mathcal{D} = \sum_i\sum_j\sum_k C_{ijk}D_{ijk}, \tag{2.5}$$

where $\mathbf{a}$ and $\mathbf{b}$ are vectors, $\mathbf{A}$ and $\mathbf{B}$ second order tensors, $\mathcal{C}$ and $\mathcal{D}$ third order tensors.

Both the displacement and the test function are given in terms of FEM interpolation functions by

$$\mathbf{u}(\mathbf{X}) = \sum_{i=1}^{nnode} N^i(\mathbf{X})\,\mathbf{d}^i \tag{2.6}$$

and

$$\mathbf{w}(\mathbf{X}) = \sum_{i=1}^{nnode} N^i(\mathbf{X})\,\mathbf{w}^i, \tag{2.7}$$

where *nnode* is the total number of element nodes, N^i is the FEM shape function for the i-th node, $\mathbf{d}^i$ and $\mathbf{w}^i$ are the nodal displacement and virtual displacement for the i-th node. If the FEM shape functions N^i for $\mathbf{u}$ and $\mathbf{w}$ are chosen to be the same, this approximation is

called as the Bubnov-Galerkin formulation. Applying Equation (2.6) and (2.7) to Equation (2.2), the preceding weak form becomes

$$\begin{aligned}\sum_{e=1}^{nelem}\sum_{i=1}^{nnode}\sum_{j=1}^{nnode}\mathbf{w}^i\cdot\int_{\Omega_{0e}}\rho_0 N^i N^j\ddot{\mathbf{d}}^j d\Omega_0 = &-\sum_{e=1}^{nelem}\sum_{i=1}^{nnode}\mathbf{w}^i\cdot\int_{\Omega_{0e}}\mathbf{P}\frac{\partial N^i}{\partial\mathbf{X}}d\Omega_0\\ &+\sum_{e=1}^{nelem}\sum_{i=1}^{nnode}\mathbf{w}^i\cdot\int_{\Omega_{0e}}\rho_0 N^i\mathbf{b}d\Omega_0\\ &+\sum_{e=1}^{nelem}\sum_{i=1}^{nnode}\mathbf{w}^i\cdot\int_{\Gamma_{0eq}}N^i\bar{\mathbf{T}}d\Gamma_0,\end{aligned}\tag{2.8}$$

where *nelem* is the total number of elements, and $\Omega_0 e$ is the volume of element e in the reference configuration. Due to the arbitrariness of the virtual displacement $\mathbf{w}^i$, Equation (2.8) can be cast into the following equation,

$$\mathbf{M}\ddot{\mathbf{d}} = \mathbf{F}^{ext} - \mathbf{F}^{int},\tag{2.9}$$

where

$$\mathbf{M} = \sum_{e=1}^{nelem}\sum_{i=1}^{nnode}\sum_{j=1}^{nnode}\int_{\Omega_{0e}}\rho_0 N^i N^j d\Omega_0,\tag{2.10}$$

$$\mathbf{F}^{int} = \sum_{e=1}^{nelem}\sum_{i=1}^{nnode}\int_{\Omega_{0e}}\mathbf{P}\frac{\partial N^i}{\partial\mathbf{X}}d\Omega_0,\tag{2.11}$$

$$\mathbf{F}^{ext} = \sum_{e=1}^{nelem}\sum_{i=1}^{nnode}\int_{\Omega_{0e}}\rho_0 N^i\mathbf{b}d\Omega_0 + \sum_{e=1}^{nelem}\sum_{i=1}^{nnode}\int_{\Gamma_{0eq}}N^i\bar{\mathbf{T}}d\Gamma_0.\tag{2.12}$$

Equation (2.9) is the Lagrangian Finite Element Method formulation of continuum dynamics problems. The staggered leap-frog method is applied in the FEM time integration,

$$\ddot{\mathbf{d}}_n = \mathbf{M}^{-1}\left(\mathbf{F}_n^{ext} - \mathbf{F}_n^{int}\right),\tag{2.13}$$

$$\dot{\mathbf{d}}_{n+1/2} = \dot{\mathbf{d}}_{n-1/2} + \Delta t\ddot{\mathbf{d}}_n,\tag{2.14}$$

$$\mathbf{d}_{n+1} = \mathbf{d}_n + \Delta t\dot{\mathbf{d}}_{n+1/2},\tag{2.15}$$

where n is the time step, and Δt is the time increment.

2.2 The Surface Traction Method

Generally, the surface traction, which is a force vector on a cross-section divided by cross-section area, is applied to surfaces [26], [55], [87]. Here this method is called the

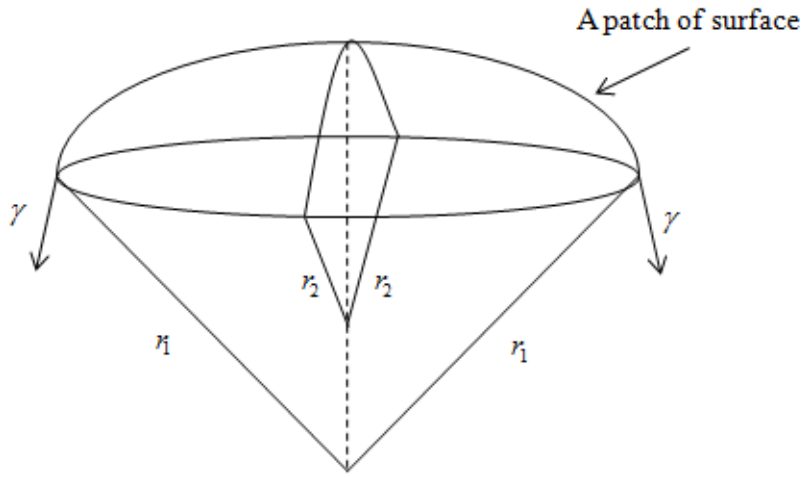

Figure 2.2: A patch of surface.

surface traction method in this dissertation. Consider a patch of surface of a fluid with radius r_1 and r_2. The surface tension $\boldsymbol{\gamma}$ acts on the circumference. The inner and outer pressure are denoted as p_i and p_o respectively. Then, the force balance equation of the patch of surface can be written as

$$p_i - p_o = \gamma \nabla \cdot \mathbf{n} \tag{2.16}$$

where $\mathbf{n}$ is the unit normal vector of the surface. The unsigned total curvature κ of the surface is equal to the divergence of the normal vector [67],

$$\begin{aligned} \kappa &= \frac{1}{r_1} + \frac{1}{r_2} \\ &= |\nabla \cdot \mathbf{n}| . \end{aligned} \tag{2.17}$$

Then, the force balance equation becomes

$$p_i - p_o = \gamma \kappa \tag{2.18}$$

Equation (2.18) is called the Young-Laplace equation. It states that the inner pressure is always greater than the outer pressure, since the surface energy and the curvature are positive, and the pressure difference is zero only if the curvature is zero, i.e. when the surface is flat.

The surface traction vector $\mathbf{t}$ is defined as

$$\mathbf{t} = \boldsymbol{\sigma} \cdot \mathbf{n}, \tag{2.19}$$

where $\boldsymbol{\sigma}$ is the Cauchy stress, and $\mathbf{n}$ is the normal vector of the surface. Here, we consider only hydrostatic pressure as the inner and outer stress, i.e. $\boldsymbol{\sigma} = -p\mathbf{I}$. Then, the surface

traction vector becomes

$$\mathbf{t} = -\left(p_i - p_o\right)\mathbf{n}. \tag{2.20}$$

By substituting Equation (2.18) into Equation (2.20), we obtain the relation between the surface energy and the surface traction vector,

$$\mathbf{t} = -\gamma\kappa\mathbf{n}. \tag{2.21}$$

Once we obtain the curvature and the normal vectors, we can compute the surface traction vector. By applying Equation (2.21) as the prescribed surface traction to the Finite Element Method formulation, Equation (2.9), the surface tension can be incorporated into the Finite Element Method formulation. Equation (2.21) can be modified to viscous fluid [9], [48], [49],

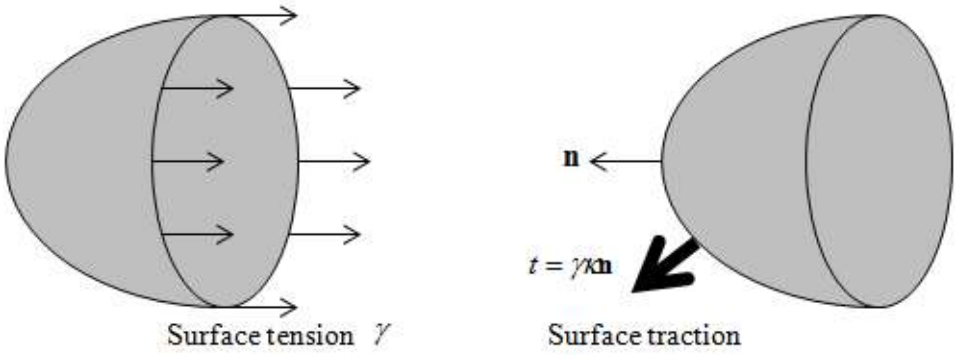

Figure 2.3: The surface traction which is equivalent to the surface tension.

$$\mathbf{t} = -\gamma\kappa\mathbf{n} + \nabla_S\gamma, \tag{2.22}$$

where $\nabla_s = \nabla\gamma - \mathbf{n}\left(\mathbf{n}\cdot\nabla\gamma\right)$ is the surface gradient. However, Equation (2.21) is often used for viscous fluid as an approximation due to its simplicity.

In case that the normal vector in the reference configuration $\mathbf{N}$ is known, Nanson's formula can be used to compute the normal vector,

$$\mathbf{n}da = J\mathbf{F}^{-T}\mathbf{N}dA, \tag{2.23}$$

where da and dA are the area in the current and reference configurations respectively, $\mathbf{F}$ is the deformation gradient tensor, and $J = \det\mathbf{F}$ is the volume ratio. From Nanson's formula, the following relationship between the normal vector in the current and that of the reference configuration is obtained as

$$\mathbf{n} = \sqrt{\mathbf{N}\cdot\mathbf{C}^{-1}\mathbf{N}}\mathbf{F}^{-T}\mathbf{N}, \tag{2.24}$$

where $\mathbf{C}$ is the right Cauchy-Green tensor, which is defined as

$$\mathbf{C} = \mathbf{F}^T\mathbf{F}. \tag{2.25}$$

By substituting Equation (2.24) into Equation (2.17), the following equation is obtained, see Appendix A,

$$\kappa = \frac{\mathbf{F}^T\mathcal{G}\vdots(\mathbf{C}^{-1}\mathbf{N}\otimes\mathbf{C}^{-1}\mathbf{N}\otimes\mathbf{C}^{-1}\mathbf{N}) - \nabla_{\mathbf{X}}\mathbf{N} : (\mathbf{C}^{-1}\mathbf{N}\otimes\mathbf{C}^{-1}\mathbf{N})}{(\mathbf{N}\cdot\mathbf{C}^{-1}\mathbf{N})^{3/2}} - \left(\mathbf{n}^T\mathcal{G}\right) : \mathbf{C}^{-1} + \sqrt{\mathbf{N}\cdot\mathbf{C}^{-1}\mathbf{N}}\mathbf{C}^{-1} : \nabla_{\mathbf{X}}\mathbf{N}, \tag{2.26}$$

where $\mathcal{G}$ is the second order deformation gradient tensor, defined as

$$\mathcal{G} = \frac{\partial^2\mathbf{x}}{\partial\mathbf{X}\otimes\partial\mathbf{X}}. \tag{2.27}$$

The computational method of the higher order deformation gradient tensors in the Finite Element Method is discussed in Appendix B.

2.3 The Finite Element Method Based Surface Tension Model

The surface traction method requires the normal vector and the curvature in the current configuration. To compute these values analytically, it is necessary to compute the deformation gradient tensor and the derivatives of the deformation gradient tensor. These processes are computationally expensive. To improve computational efficiency and to extend to dynamic wetting model, here a new simple surface tension model for the Finite Element Method is introduced.

Surface tension is defined as the force along a line of unit length, where the force is parallel to the surface but perpendicular to the line [56], shown in Figure 2.4. Note that the

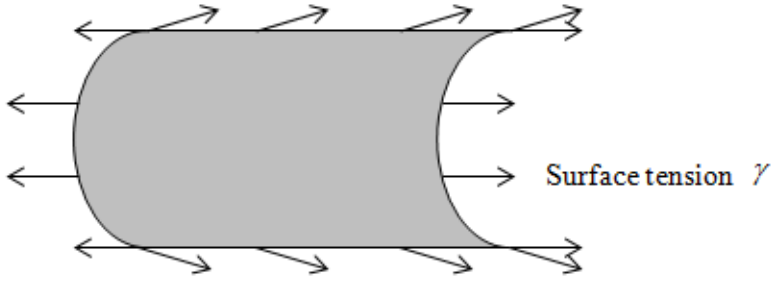

Figure 2.4: Surface tension acts on a surface patch in three dimensions.

direction of the surface tension is depicted as an internal force in Figure 2.4. Based on this

definition, we apply the surface tension as the nodal external force to the surface patch of the Lagrangian Finite Element Method. Equation (2.9) is modified to

$$\mathbf{M}\ddot{\mathbf{d}} = \mathbf{F}^{ext} - \mathbf{F}^{int} + \mathbf{F}^{srf}, \tag{2.28}$$

where $\mathbf{F}^{srf}$ are the additional nodal forces which come from the surface tension, called the surface tension force. Note that the direction of the surface tension force in Equation (2.29) must be in the opposite direction from Figure 2.4, since the surface tension force is applied as an external force to the Finite Element Method formulation.

Consider a plane body of unit thickness, the surface tension $[N/m]$ is simply the force $[N]$. Thus, we apply the surface tension as the external force to each node of the surface patch, and the direction is parallel to the edge of the surface patch, shown in Figure 2.5. By

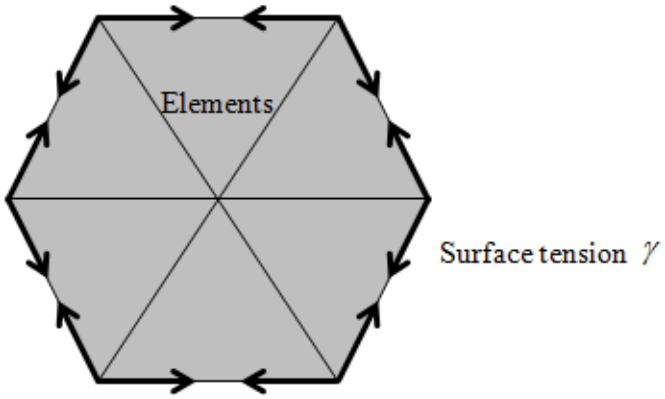

Figure 2.5: The proposed FEM surface tension model in two dimensions.

taking the summation of surface tension forces at each node, we obtain the resultant forces. Because two surface tension forces act in the opposite directions when the surface is flat, the resultant force is zero on a flat surface, shown in Figure 2.6. It is consistent with the surface traction method, and the proposed FEM surface tension model needs to calculate the tangential direction of a surface patch and take the summation of the surface tension forces in two dimensions. When the positions of two nodes of the surface patch are $\mathbf{x}_1$ and $\mathbf{x}_2$, the direction of the surface tension forces at node $\mathbf{x}_1$ and $\mathbf{x}_2$ are give by $(\mathbf{x}_2 - \mathbf{x}_1) / |\mathbf{x}_2 - \mathbf{x}_1|$ and $(\mathbf{x}_1 - \mathbf{x}_2) / |\mathbf{x}_2 - \mathbf{x}_1|$. For example, in case of Figure 2.6, surface tension forces at node 1 and

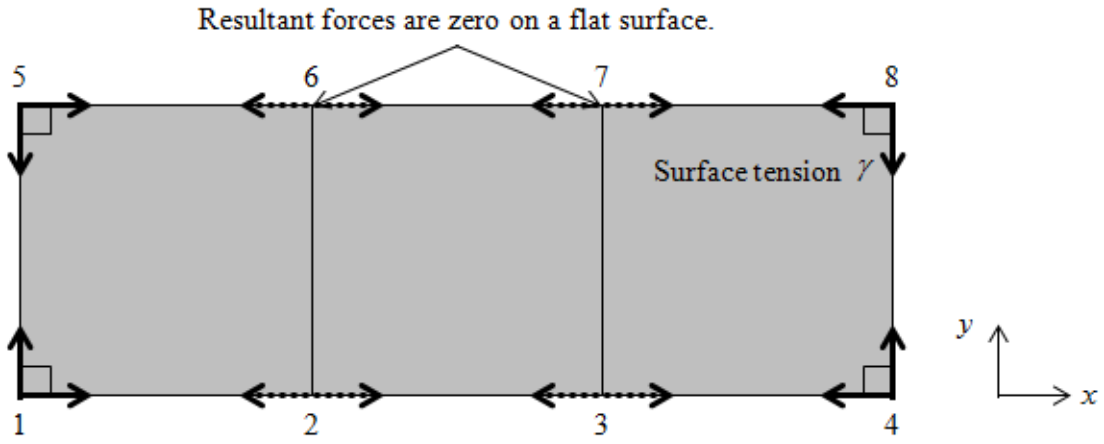

Figure 2.6: Resultant surface tension forces on a flat surface.

2 are given by

$$\mathbf{F}^{srf,1} = \gamma \frac{\mathbf{x}_2 - \mathbf{x}_1}{|\mathbf{x}_2 - \mathbf{x}_1|} + \gamma \frac{\mathbf{x}_5 - \mathbf{x}_1}{|\mathbf{x}_5 - \mathbf{x}_1|} \tag{2.29}$$

$$= \gamma \begin{pmatrix} 1 \\ 0 \end{pmatrix} + \gamma \begin{pmatrix} 0 \\ 1 \end{pmatrix} \tag{2.30}$$

$$= \gamma \begin{pmatrix} 1 \\ 1 \end{pmatrix}, \tag{2.31}$$

and

$$\mathbf{F}^{srf,2} = \gamma \frac{\mathbf{x}_1 - \mathbf{x}_2}{|\mathbf{x}_2 - \mathbf{x}_1|} + \gamma \frac{\mathbf{x}_3 - \mathbf{x}_2}{|\mathbf{x}_3 - \mathbf{x}_2|} \tag{2.32}$$

$$= \gamma \begin{pmatrix} -1 \\ 0 \end{pmatrix} + \gamma \begin{pmatrix} 1 \\ 0 \end{pmatrix} \tag{2.33}$$

$$= \begin{pmatrix} 0 \\ 0 \end{pmatrix}. \tag{2.34}$$

In three dimensions, it is necessary to multiply the half of the edge length, since the unit of the surface tension is the force per length $[N/m]$, and there are two nodes in each edge for linear elements. The direction of surface tension forces can be obtained by following way. First, we compute normal vector of the patch at node $\mathbf{x}_1$ by the cross product. In the case of Figure 2.7, the normal vector is obtained as

$$\mathbf{n} = \frac{(\mathbf{x}_2 - \mathbf{x}_1)}{|\mathbf{x}_2 - \mathbf{x}_1|} \times \frac{(\mathbf{x}_4 - \mathbf{x}_1)}{|\mathbf{x}_4 - \mathbf{x}_1|}. \tag{2.35}$$

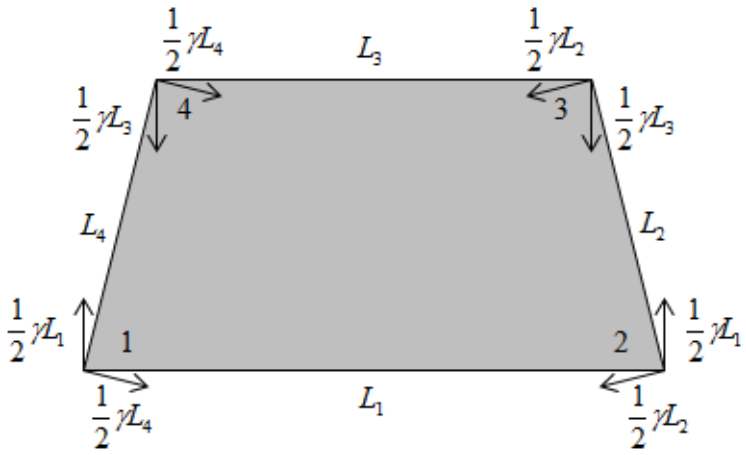

Figure 2.7: The direction of surface tension forces in three dimensions.

Equation (2.36) can be replaced by Equation (2.24) when the normal vector in the reference configuration is known. Then, the inner product of the direction of the surface tension force $\mathbf{e}$ and vector $\mathbf{x}_2 - \mathbf{x}_1$ is zero, because the surface tension is perpendicular to the line. In addition, the cross product of $(\mathbf{x}_2 - \mathbf{x}_1) / |\mathbf{x}_2 - \mathbf{x}_1|$ and $\mathbf{e}$ is $\mathbf{n}$, since the surface tension is parallel to the surface. Thus, the direction of the surface tension force $\mathbf{e}$ can be obtained by computing the cross product of $\mathbf{n}$ and $(\mathbf{x}_2 - \mathbf{x}_1) / |\mathbf{x}_2 - \mathbf{x}_1|$,

$$\mathbf{e} = \mathbf{n} \times \frac{(\mathbf{x}_2 - \mathbf{x}_1)}{|\mathbf{x}_2 - \mathbf{x}_1|}. \tag{2.36}$$

When there is no torsion in a surface patch, the direction of the surface tension at each node in an edge are the same. However, since there may exist torsion after the deformation, we should compute the direction of the surface tension at each node in an edge for consistency with the neighbor surface patch. Finally, in three dimensions, the proposed FEM surface tension model needs to calculate the normal vector of a surface patch at each node, the direction of the surface tension and the length of the edge.

Chapter 3

A Dynamic Wetting Model

In this chapter, an overview of a dynamic wetting model based on the proposed FEM surface tension model is presented. First, we discuss the resultant force at the contact line (the intersection of the liquid-gas interface with the solid substrate), which leads to the same result as that of the Young Equation [97] in equilibrium state. Also, we discuss implementations of the dynamic wetting model.

3.1 The Resultant Force at the Contact Line

Distributed forces at the contact line are illustrated in Figure 3.1. In figure 3.1, γ_{LG}^{L} is

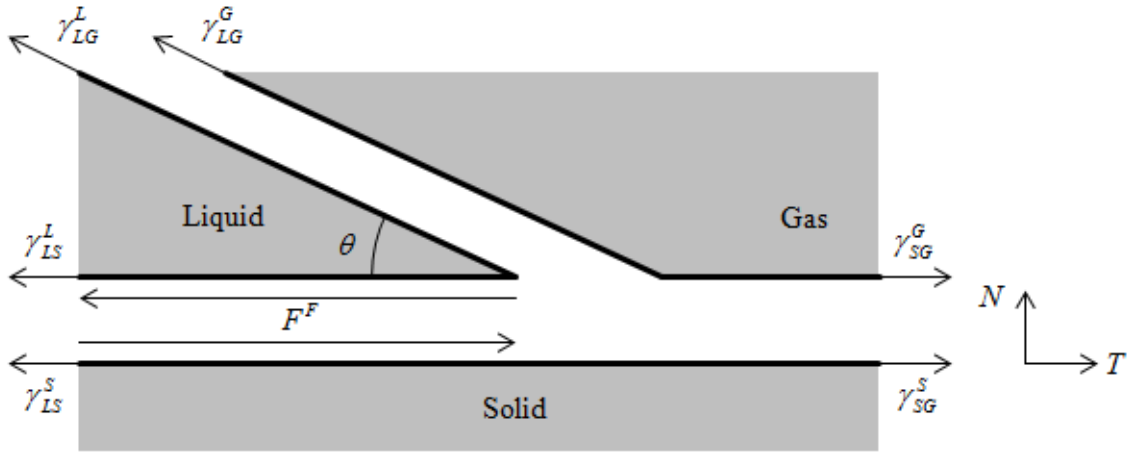

Figure 3.1: Illustration of distributed forces at the contact line.

the surface tension of the liquid between the liquid and gas, γ_{LS}^{L} is the surface tension of the liquid between the liquid and solid, γ_{LS}^{S} is the surface tension of the solid between the

liquid and solid, γ_{SG}^{S} is the surface tension of the solid between the solid and gas, γ_{LG}^{G} is the surface tension of the gas between the liquid and gas, γ_{SG}^{G} is the surface tension of the gas between the solid and gas, θ is the contact angle, F^F is the friction force between the liquid and solid, and T and N denote the tangential and normal direction of the solid surface.

On the liquid surface, the resultant force at the contact line in the tangential direction F_T^L is given by

$$F_T^L = -\gamma_{LS}^{L} - \gamma_{LG}^{L}\cos\theta - F^F. \tag{3.1}$$

Similarly, the resultant forces at the contact line in the tangential direction on the solid surface F_T^S and the gas surface F_T^G are given by

$$F_T^S = -\gamma_{LS}^{S} + \gamma_{SG}^{L} + F^F, \tag{3.2}$$

and

$$F_T^G = -\gamma_{LG}^{G}\cos\theta + \gamma_{SG}^{G}. \tag{3.3}$$

Thus, the resultant force at the contact line in the tangential direction is

$$\begin{aligned} F_T &= F_T^L + F_T^S + F_T^G && (3.4)\\ &= \left(\gamma_{SG}^{S} + \gamma_{SG}^{G}\right) - \left(\gamma_{LG}^{L} + \gamma_{LG}^{G}\right)\cos\theta - \left(\gamma_{LS}^{L} + \gamma_{LS}^{S}\right) && (3.5)\\ &= \gamma_{SG} - \gamma_{LG}\cos\theta - \gamma_{LS}, && (3.6) \end{aligned}$$

where

$$\begin{aligned} \gamma_{LG} &= \gamma_{LG}^{L} + \gamma_{LG}^{G}, && (3.7)\\ \gamma_{LS} &= \gamma_{LS}^{L} + \gamma_{LS}^{S}, && (3.8)\\ \gamma_{SG} &= \gamma_{SG}^{S} + \gamma_{SG}^{G}. && (3.9) \end{aligned}$$

Since the friction forces on the liquid and solid surface are of the same magnitude but in the opposite direction, the friction forces are balanced to be zero. Equation (3.6) is exactly the same as the Young equation $\gamma_{SG} - \gamma_{LG}\cos\theta - \gamma_{LS} = 0$ [97] when the system is at equilibrium state, i.e. the resultant force F_T is zero.

On the other hand, the resultant force at the contact line in the normal direction on the liquid surface F_N^L, the solid surface F_N^S, and the gas surface F_N^G are given by

$$F_N^L = \gamma_{LG}^{L}\sin\theta, \tag{3.10}$$

$$F_N^S = 0, \tag{3.11}$$

and

$$F_N^G = \gamma_{LG}^{G}\sin\theta. \tag{3.12}$$

Thus, the resultant force at the contact line in the normal direction is given by

$$\begin{aligned} F_N &= F_N^L + F_N^S + F_N^G && (3.13)\\ &= \left(\gamma_{LG}^{L} + \gamma_{LG}^{G}\right)\sin\theta && (3.14)\\ &= \gamma_{LG}\sin\theta. && (3.15) \end{aligned}$$

3.2 Implementations of the Dynamic Wetting Model

Figure 3.2 illustrates surface patches at the contact line in a setting of the two dimensional Finite Element Method that is introduced in Chapter 2. Dynamic wetting analysis by

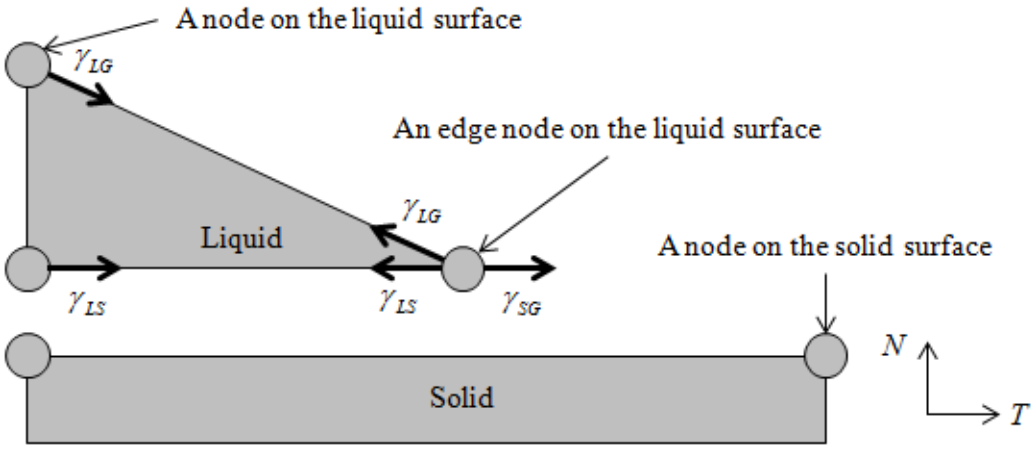

Figure 3.2: Surface patches at the contact line in the two dimensional Finite Element Method.

Molecular Dynamics is often used to model the gas. However, we do not model the gas due to the following reasons. First, the deformation of the gas is quite large, because the density of the gas is very small compared to the liquid and the solid. To capture the deformation of the gas is too difficult for the Lagrangian Finite Element Method. Second, the effect of the deformation of the gas to the deformation of the liquid and the solid is quite small because the liquid and the solid are very stiff compared to the gas.

The surface energy between the liquid and gas γ_{LG} is applied to surface patches of the liquid which are in contact with the gas based on the proposed FEM surface tension model, see Section 2.3. The surface tension between the liquid and gas at the contact line $\boldsymbol{\gamma}_{LG}$ is given by

$$\boldsymbol{\gamma}_{LG} = \begin{pmatrix} -\gamma_{LG}\cos\theta \\ \gamma_{LG}\sin\theta \end{pmatrix}, \tag{3.16}$$

where the coordinate system is the tangential and normal vector of the solid surface. Similarly, the surface energy between the liquid and solid γ_{LS} is applied to surface patches of the liquid which are in contact with the solid based on the proposed FEM surface tension model. The surface tension between the liquid and solid at the contact line $\boldsymbol{\gamma}_{LS}$ is given by

$$\boldsymbol{\gamma}_{LS} = \begin{pmatrix} -\gamma_{LS} \\ 0 \end{pmatrix}. \tag{3.17}$$

Since the stiffness (unit P_a) of the solid is several orders of magnitude greater than the surface energy per unit length (unit P_a), the solid deformation due to the surface energy may

be assumed to be negligible. Under such approximation, the surface energy is not applied to the solid surface, i.e. the deformation of the solid due to the surface energy is neglected.

To satisfy Equation (3.6), the surface energy between the solid and gas γ_{SG} must be applied to the contact line. We simply apply the surface energy between the solid and gas γ_{SG} to the edge node at the contact line in the tangential direction of the solid surface. Subsequently the surface tension $\boldsymbol{\gamma}_{SG}$ is given by

$$\boldsymbol{\gamma}_{SG} = \begin{pmatrix} \gamma_{SG} \\ 0 \end{pmatrix}. \tag{3.18}$$

Finally, the resultant force at the contact line $\mathbf{F}^{srf}$ is given by

$$\mathbf{F}^{srf} = \boldsymbol{\gamma}_{SG} + \boldsymbol{\gamma}_{LG} + \boldsymbol{\gamma}_{LS} \tag{3.19}$$

$$= \begin{pmatrix} \gamma_{SG} - \gamma_{LG}\cos\theta - \gamma_{LS} \\ \gamma_{LG}\sin\theta \end{pmatrix}. \tag{3.20}$$

Equation (3.20) is consistent with Equation (3.6) and (3.15).

Implementations of the Dynamic Wetting Model in Two Dimensions

In the case of the two dimensional Finite Element Method, a linear surface patch is constructed by two Finite Element Method nodes. Figure 3.3 shows three cases of the surface patch of the liquid in the two dimensional Finite Element Method.

- Case a, Figure 3.3 (a): Neither of two nodes are in contact with the solid surface. The surface energy between the liquid and gas γ_{LG} is applied to the surface patch, because the surface patch is fully in contact with the gas.
- Case b, Figure 3.3 (b): One of the nodes is in contact with the solid surface. The surface energy between the liquid and gas γ_{LG} is applied to the surface patch. In addition, the surface energy between the solid and gas γ_{SG} is applied to the node which is in contact with the solid surface in the tangential direction of the solid surface.
- Case c, Figure 3.3 (c): Both of the nodes are in contact with the solid surface. The surface energy between the liquid and solid γ_{LS} is applied to the surface patch, because this surface patch is fully in contact with the solid surface.

Implementations of the Dynamic Wetting Model in Three Dimensions

Figure 3.4 show triangular surface patches of the liquid in the three dimensional Finite Element Method. For a triangular surface patch, we need to consider four cases.

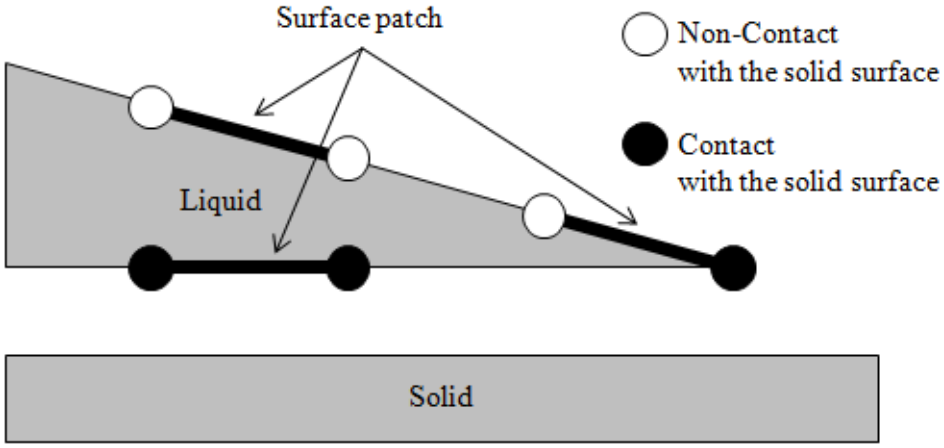

Figure 3.3: Three cases of the surface patch of the liquid in the two dimensional Finite Element Method: (a) Neither of two nodes are in contact with the solid surface, (b) One of the nodes is in contact with the solid surface, (c) Both of the nodes are in contact with the solid surface.

- Case a, Figure 3.4 (a): None of the three nodes are in contact with the solid surface. The surface energy between the liquid and gas γ_{LG} is applied to the all edges a, b and c based on the proposed FEM surface tension model (see Chapter 2), because the surface patch is fully in contact with the gas.

- Case b, Figure 3.4 (b): Only one of the nodes is in contact with the solid surface. The surface energy between the liquid and gas γ_{LG} is applied to the all edges, the same as Case a.

- Case c, Figure 3.4 (c): Two nodes are in contact with the solid surface. The surface energy between the liquid and gas γ_{LG} is applied to the all edges. In addition, the surface energy between the solid and gas γ_{SG} is applied to the edge a. The direction of γ_{SG} is shown in Figure 3.5, where $\mathbf{n}$ is the normal vector of the solid surface, and $\mathbf{x}_a$ is the unit vector of the edge a, and $\mathbf{x}$ is the direction of γ_{SG}. The direction of the surface energy between the solid and gas $\mathbf{e}$ can be obtained by the cross product,

$$\mathbf{e} = \mathbf{x}_a \times \mathbf{n}. \tag{3.21}$$

- Case d, Figure 3.4 (d): All nodes are in contact with the solid surface. The surface energy between the liquid and solid γ_{LS} is applied to the all edges, because the surface patch is fully in contact with the solid surface.

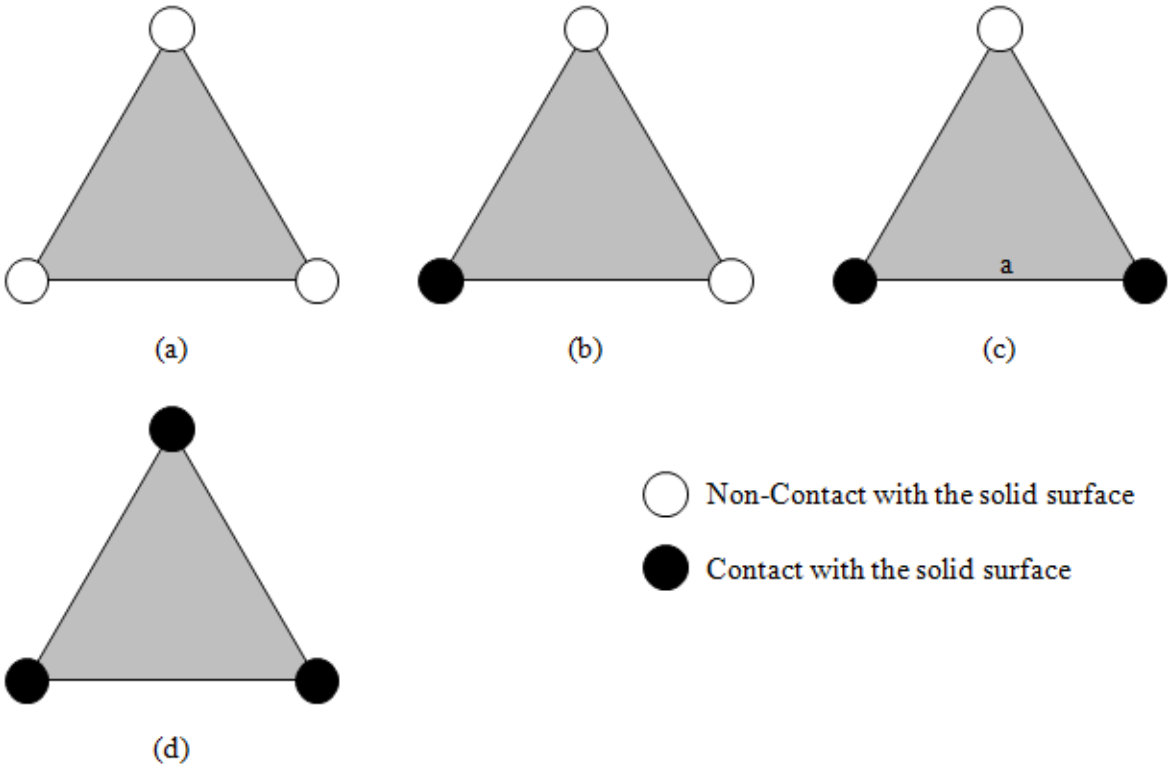

Figure 3.4: Triangular surface patches of the liquid in the three dimensional Finite Element Method: (a) None of the three nodes are in contact with the solid surface, (b) Only one of the nodes is in contact with the solid surface, (c) Two nodes are in contact with the solid surface, (d) All nodes are in contact with the solid surface.

Figure 3.6 show rectangular surface patches in the three dimensional Finite Element Method. For a rectangular surface patch, there are five cases.

- Case a, Figure 3.6 (a): None of the nodes are in contact with the solid surface.
  The surface energy between the liquid and gas γ_{LG} is applied to the all edges a, b, c and d based on the proposed FEM surface tension model (see Chapter 2), because the surface patch is fully in contact with the gas.

- Case b, Figure 3.6 (b): Only one of the nodes is in contact with the solid surface.
  The surface energy between the liquid and gas γ_{LG} is applied to the all edges, the same as Case a.

- Case c, Figure 3.6 (c): Two nodes are contact with the solid surface.
  The surface energy between the liquid and gas γ_{LG} is applied to the all edges. In

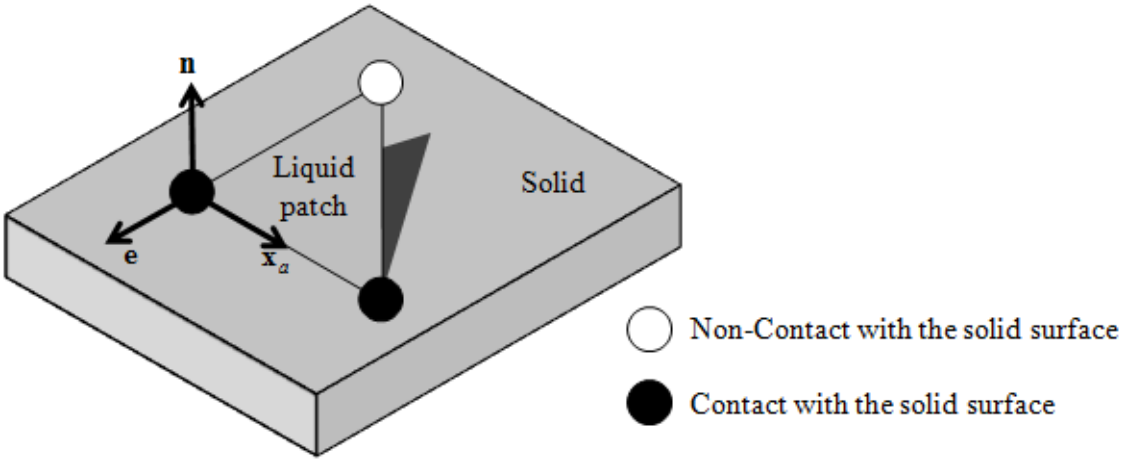

Figure 3.5: The direction of the surface tension between the solid and gas.

addition, the surface energy between the solid and gas γ_{SG} is applied to the edge a. The direction of γ_{SG} can be obtained by Equation (3.21).

- Case d, Figure 3.6 (d): Three nodes are in contact with the solid surface.
  The surface energy between the liquid and gas γ_{LG} is applied to the all edges. In addition, the surface energy between the solid and gas γ_{SG} is applied to the edge a and b. The direction of γ_{SG} can be obtained by Equation (3.21).

- Case e, Figure 3.6 (e): All nodes are in contact with the solid surface.
  The surface energy between the liquid and solid γ_{LS} is applied to the all edges, because the surface patch is fully in contact with the solid surface.

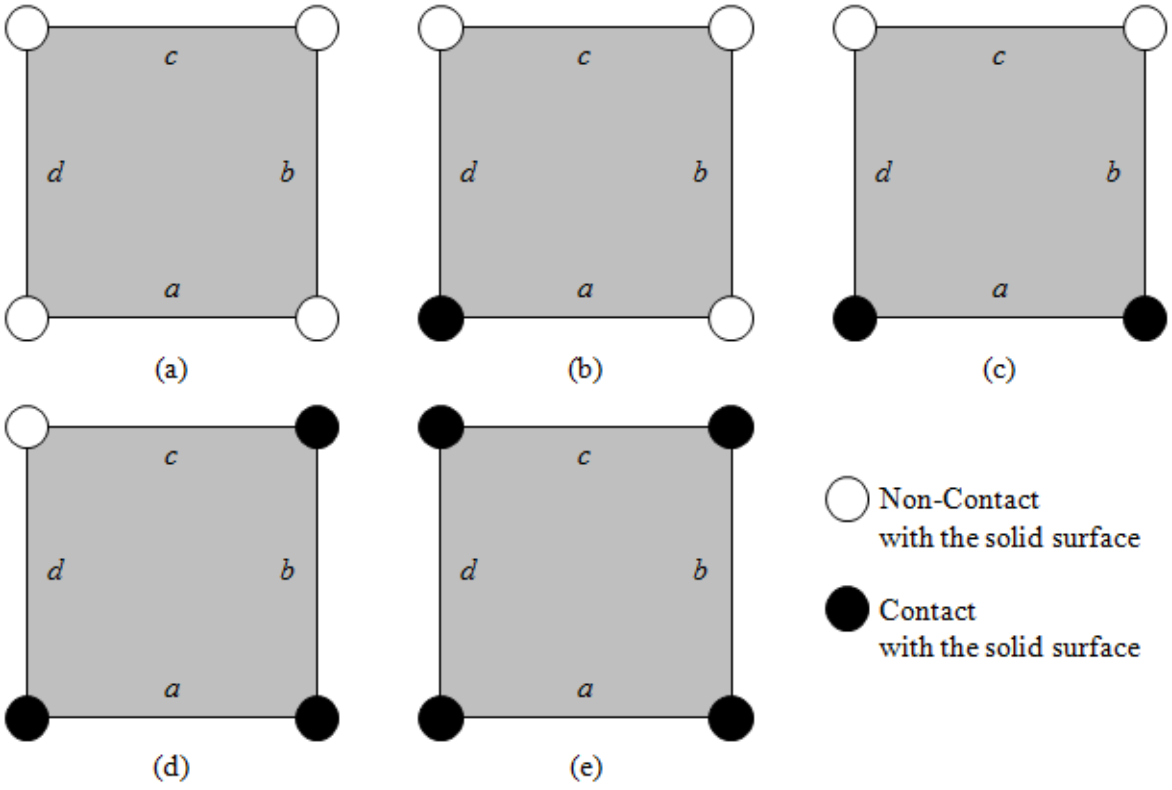

Figure 3.6: Rectangular surface patches of the liquid in the three dimensional Finite Element Method: (a) None of the nodes are in contact with the solid surface, (b) Only one of the nodes is in contact with the solid surface, (c) Two nodes are in contact with the solid surface, (d) Three nodes are in contact with the solid surface, (e) All nodes are in contact with the solid surface.

Chapter 4

A Galerkin Weak Formulation of Dynamic Wetting

In the previous chapter, we have presented the dynamic wetting model based on the proposed FEM surface tension model. Since the model is based on the surface tension model, only the surface energy is considered. To take into account the effect of the surface stress that is a function of both surface stress as well as the surface and bulk strains, in this chapter, we present a Galerkin weak formulation of the surface, and we apply it to solve the dynamic wetting problems. Moreover, Finite Element Method implementations are discussed for both two and three dimensions.

4.1 A Galerkin Weak Formulation of the Surface of a Liquid

The contact line in two dimensions is shown in Figure 4.1. The governing equation of the surface may be found in [80], and here it is modified to a special case as shown in Figure 4.1. In this case, the governing equation of the solid surface is

$$\mathbf{f}^{S,S} = div\boldsymbol{\sigma}^S + \mathbf{f}^F, \tag{4.1}$$

where $\mathbf{f}^{S,S}$ is the surface inertia force ($[N/m^2]$), $\boldsymbol{\sigma}^S$ is the surface stress ($[N/m]$), $\mathbf{f}^F$ is the friction force ($[N/m^2]$). Because the solid is assumed to be sufficiently stiff, there is essentially no deformation cased by the surface stress and friction force. Under this assumption, the surface inertia force can be neglected, i.e. $\mathbf{f}^{S,S} = \mathbf{0}$. Hence, Equation (4.1) becomes

$$\mathbf{0} = div\boldsymbol{\sigma}^S + \mathbf{f}^F. \tag{4.2}$$

The Galerkin weak formulation is obtained by the virtual work principle via the virtual displacement $\delta\mathbf{u} = \mathbf{w}$,

$$\mathbf{0} = \int_{\partial\Omega^S} \mathbf{w} \cdot div\boldsymbol{\sigma}^S ds + \int_{\partial\Omega^S} \mathbf{w} \cdot \mathbf{f}^F ds, \tag{4.3}$$

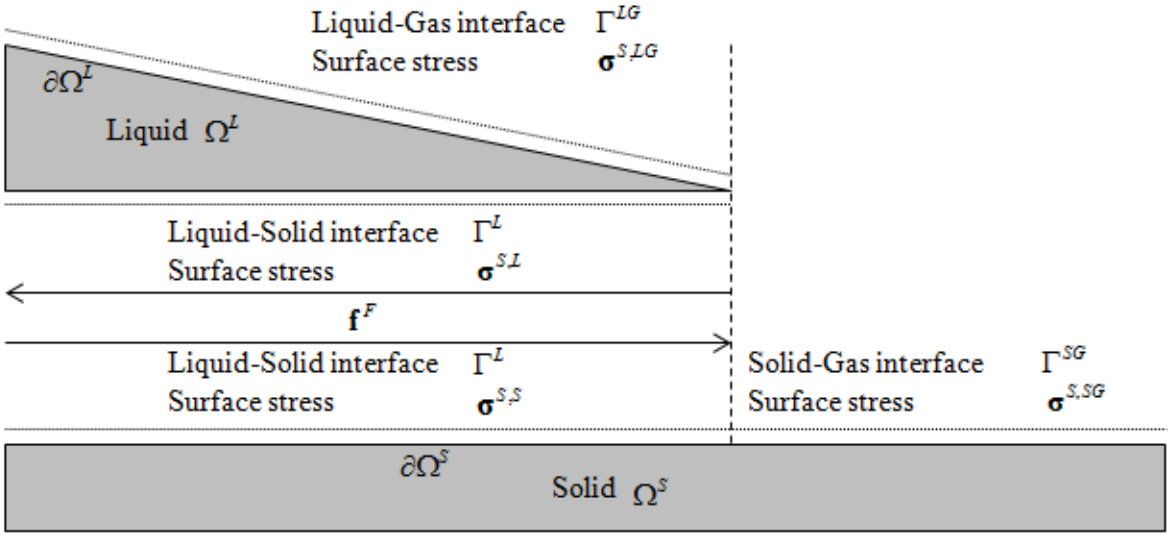

Figure 4.1: Illustration of the contact line.

where $\partial\Omega^S$ denotes the solid surface. Via integration by parts, we obtain the following equation,

$$\mathbf{0} = -\int_{\partial\Omega^S} div\mathbf{w} : \boldsymbol{\sigma}^S ds + \int_{\partial\Omega^S} \mathbf{w} \cdot \mathbf{f}^F ds, \tag{4.4}$$

where $\boldsymbol{\sigma}^S\mathbf{n} = \mathbf{0}$ on $\partial^2\Omega^S$ is assumed, in which $\mathbf{n}$ is the normal vector. Note that $\partial\Omega^S = \Gamma^{SG} \cup \Gamma^S$, where Γ^{SG} and Γ^S are the solid surface in contact with the gas and liquid, respectively. Thus, Equation (4.4) becomes

$$\mathbf{0} = -\int_{\Gamma^{SG}} div\mathbf{w} : \boldsymbol{\sigma}^{S,SG} ds - \int_{\Gamma^S} div\mathbf{w} : \boldsymbol{\sigma}^{S,S} ds + \int_{\Gamma^S} \mathbf{w} \cdot \mathbf{f}^F ds, \tag{4.5}$$

where $\boldsymbol{\sigma}^{S,SG}$ is the surface stress between the solid and gas, $\boldsymbol{\sigma}^{S,S}$ is the surface stress between the solid and liquid, and the friction force on the solid surface between the solid and gas is zero is applied.

On the other hand, the governing equation of the liquid surface is given by

$$\mathbf{f}^{S,L} = div\boldsymbol{\sigma}^S - \mathbf{f}^F, \tag{4.6}$$

where $\mathbf{f}^{S,L}$ is the surface inertia force ($[N/m^2]$). The friction force on the liquid surface is in opposite direction from the friction force on the solid surface, but the magnitude is the same. The Galerkin weak formulation is obtained by using the virtual displacement $\mathbf{w}$,

$$\int_{\partial\Omega^L} \mathbf{w} \cdot \mathbf{f}^{S,L} ds = \int_{\partial\Omega^L} \mathbf{w} \cdot div\boldsymbol{\sigma}^L ds - \int_{\partial\Omega^L} \mathbf{w} \cdot \mathbf{f}^F ds. \tag{4.7}$$

Similar to the solid surface, the following equation can be obtained by integration by parts,

$$\int_{\partial\Omega^L} \mathbf{w}\cdot\mathbf{f}^{S,L}ds = -\int_{\partial\Omega^L} div\mathbf{w} : \boldsymbol{\sigma}^S ds - \int_{\partial\Omega^L} \mathbf{w}\cdot\mathbf{f}^F ds. \tag{4.8}$$

Using the fact that $\partial\Omega^L = \Gamma^{LG} \cup \Gamma^L$, where Γ^{LG} and Γ^L are the liquid surface in contact with the gas and solid respectively,

$$\int_{\partial\Omega^L} \mathbf{w}\cdot\mathbf{f}^{S,L}ds = -\int_{\Gamma^{LG}} div\mathbf{w} : \boldsymbol{\sigma}^{S,LG} ds - \int_{\Gamma^L} div\mathbf{w} : \boldsymbol{\sigma}^{S,L} ds - \int_{\Gamma^L} \mathbf{w}\cdot\mathbf{f}^F ds, \tag{4.9}$$

where $\boldsymbol{\sigma}^S\mathbf{n} = \mathbf{0}$ on $\partial^2\Omega^L$ is assumed. The following equation is obtained by using the summation Equation (4.5) and (4.9),

$$\begin{aligned}\int_{\partial\Omega^L} \mathbf{w}\cdot\mathbf{f}^{S,L}ds = &-\int_{\Gamma^{SG}} div\mathbf{w} : \boldsymbol{\sigma}^{S,SG} ds - \int_{\Gamma^{LG}} div\mathbf{w} : \boldsymbol{\sigma}^{S,LG} ds \\ &- \int_{\Gamma^L} div\mathbf{w} : \boldsymbol{\sigma}^{S,L} ds - \int_{\Gamma^S} div\mathbf{w} : \boldsymbol{\sigma}^{S,S} ds \\ &- \int_{\Gamma^L} \mathbf{w}\cdot\mathbf{f}^F ds + \int_{\Gamma^S} \mathbf{w}\cdot\mathbf{f}^F ds.\end{aligned} \tag{4.10}$$

Since the contact areas $\Gamma^L = \Gamma^S$, we have

$$\begin{aligned}\int_{\partial\Omega^L} \mathbf{w}\cdot\mathbf{f}^{S,L}ds = &-\int_{\Gamma^{SG}} div\mathbf{w} : \boldsymbol{\sigma}^{S,SG} ds - \int_{\Gamma^{LS}} div\mathbf{w} : \boldsymbol{\sigma}^{S,LS} ds \\ &- \int_{\Gamma^{LG}} div\mathbf{w} : \boldsymbol{\sigma}^{S,LG} ds,\end{aligned} \tag{4.11}$$

where $\Gamma^{LS} = \Gamma^L = \Gamma^S$, and $\boldsymbol{\sigma}^{S,LS} = \boldsymbol{\sigma}^{S,L} + \boldsymbol{\sigma}^{S,S}$. Equation (4.11) is the Galerkin weak formulation of the dynamic wetting model for the surface elements.

4.2 A Finite Element Formulation of the Galerkin Weak Formulation of Dynamic Wetting

Consider the following FEM interpolation,

$$\mathbf{w} = \sum_{i=1}^{nnode} N^i \mathbf{w}^i, \tag{4.12}$$

where *nnode* is the number of nodes, N^i is the FEM shape function for the i-th node, and $\mathbf{w}^i$ is the nodal virtual displacement. The following equation can be obtained by substituting

Equation (4.12) into Equation (4.11),

$$\sum_{i=1}^{nnode} \mathbf{w}^i \cdot \int_{\partial\Omega^L} N^i \mathbf{f}^{S,L} ds = -\sum_{i=1}^{nnode} \mathbf{w}^i \cdot \int_{\Gamma^{SG}} \boldsymbol{\sigma}^{S,SG} \frac{\partial N^i}{\partial \mathbf{x}} ds - \sum_{i=1}^{nnode} \mathbf{w}^i \cdot \int_{\Gamma^{LS}} \boldsymbol{\sigma}^{S,LS} \frac{\partial N^i}{\partial \mathbf{x}} ds - \sum_{i=1}^{nnode} \mathbf{w}^i \cdot \int_{\Gamma^{LG}} \boldsymbol{\sigma}^{S,LG} \frac{\partial N^i}{\partial \mathbf{x}} ds. \tag{4.13}$$

Since the nodal virtual displacement, $\mathbf{w}^i$, is arbitrary, Equation (4.13) becomes

$$\mathbf{F}^{S,L} = -\sum_{i=1}^{nnode} \int_{\Gamma^{SG}} \boldsymbol{\sigma}^{S,SG} \frac{\partial N^i}{\partial \mathbf{x}} ds - \sum_{i=1}^{nnode} \int_{\Gamma^{LS}} \boldsymbol{\sigma}^{S,LS} \frac{\partial N^i}{\partial \mathbf{x}} ds - \sum_{i=1}^{nnode} \int_{\Gamma^{LG}} \boldsymbol{\sigma}^{S,LG} \frac{\partial N^i}{\partial \mathbf{x}} ds, \tag{4.14}$$

where

$$\mathbf{F}^{S,L} = \sum_{i=1}^{nnode} \int_{\partial\Omega^L} N^i \mathbf{f}^{S,L} ds \tag{4.15}$$

is the surface inertia force. Equation (4.15) is the Finite Element Method formulation of dynamic wetting on the liquid surface. Similar to the previous model in Chapter 3, we apply the surface inertia force to the bulk Finite Element Method formulation,

$$\mathbf{M}\ddot{\mathbf{d}} = \mathbf{F}^{ext} - \mathbf{F}^{int} + \mathbf{F}^{S,L}. \tag{4.16}$$

4.3 A Virtual Solid Surface

In the derivation of the Galerkin weak formulation, it is assumed that $\Gamma^S = \Gamma^L$. However, in the Finite Element Method, positions of liquid and solid nodes are generally different, because we do not prescribe non-slip boundary condition between the liquid and solid, thus, $\Gamma^S \neq \Gamma^L$. To solve this dilemma, a virtual solid surface is introduced. The two dimensional case of the virtual solid surface is illustrated in Figure 4.2. The positions of solid nodes on the virtual solid surface are exactly the same as that of liquid nodes on the liquid surface. The variables of solid nodes on the virtual solid surface are obtained from that of solid nodes on the solid surface by using the isoparametric interpolation and FEM shape functions.

The basic idea of the isoparametric interpolation is to construct the FEM shape functions of an irregular shape element in the physical domain by mapping it from an element of same kind with a regular domain, so that FEM interpolation has at least satisfied linear consistency. The interpolation can be expressed as

$$\mathbf{x} = \Phi(\boldsymbol{\xi}), \tag{4.17}$$

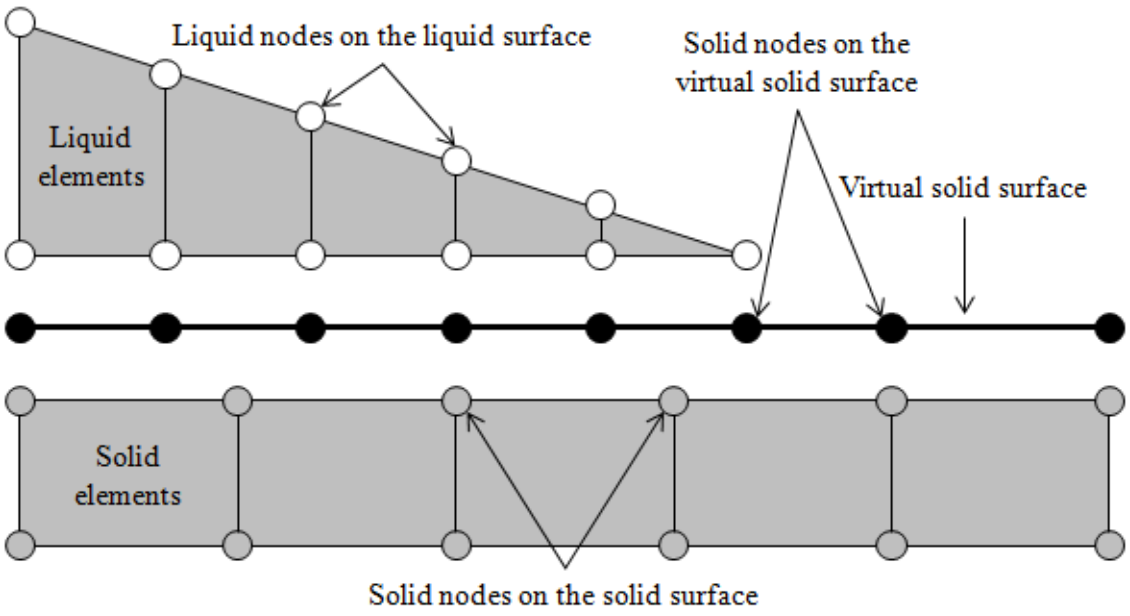

Figure 4.2: Virtual solid surface in two dimensions.

where $\mathbf{x}$ and $\boldsymbol{\xi}$ are the coordinates in the physical and natural domain respectively. A surface patch is an one dimensional element in two dimensional simulations, and it is a two dimensional element in three dimensional simulations. The variable inside the domain is interpolated as

$$f = \sum_{i}^{nnode} N^i(\boldsymbol{\xi})\, f^i, \tag{4.18}$$

where *nnode* is the number of nodes, $N^i(x)$ is the FEM shape function of the i-th node, and f^i is the nodal variable.

By using Equation (4.18), the natural coordinate can be obtained by inverting the following equation,

$$\mathbf{0} = \sum_{i}^{nnode} N^i(\boldsymbol{\xi})\, \mathbf{x}^i - \mathbf{x}. \tag{4.19}$$

In one dimensional elements, Equation (4.19) is a linear equation, and it can be solved directly,

$$0 = N^1(\xi)\, x^1 + N^2(\xi)\, x^2 \tag{4.20}$$

$$\xi = 2\frac{x - x_1}{x_2 - x_1} - 1. \tag{4.21}$$

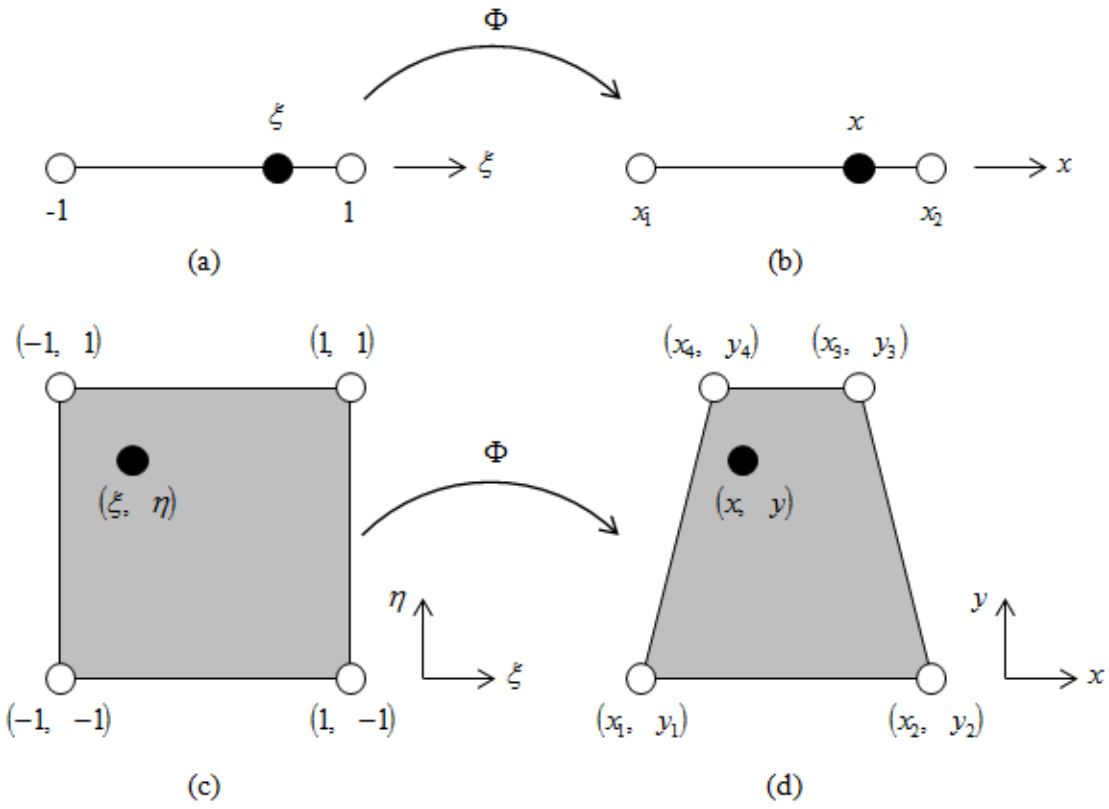

Figure 4.3: The isoparametric interpolation: (a) The natural domain in an one dimensional element, (b) The physical domain in an one dimensional element, (c) The natural domain in a two dimensional element, (d) The physical domain in a two dimensional element.

In general, Equation (4.19) cannot be solved directly for two dimensional quadrilateral elements, because it is a non-linear equation due to the bilinear term. The standard Newton-Raphson method can be applied to invert Equation (4.19),

$$\mathbf{F}\left(\boldsymbol{\xi}_I\right) \approx \mathbf{F}\left(\boldsymbol{\xi}_{I-1}\right) + \mathbf{F}'\left(\boldsymbol{\xi}_{I-1}\right)\left(\boldsymbol{\xi}_I - \boldsymbol{\xi}_{I-1}\right) \tag{4.22}$$

$$\boldsymbol{\xi}_I \approx \boldsymbol{\xi}_{I-1} - \mathbf{F}'^{-1}\left(\boldsymbol{\xi}_{I-1}\right)\mathbf{F}\left(\boldsymbol{\xi}_I\right), \tag{4.23}$$

where

$$\mathbf{F}\left(\boldsymbol{\xi}\right) = \sum_{i}^{nnode} N^i\left(\boldsymbol{\xi}\right)\mathbf{x}^i - \mathbf{x}, \tag{4.24}$$

and

$$\mathbf{F}'\left(\boldsymbol{\xi}\right) = \sum_{i}^{nnode} \frac{\partial N^i}{\partial \boldsymbol{\xi}}\left(\boldsymbol{\xi}\right)\mathbf{x}^i, \tag{4.25}$$

and $I = 1, 2, ..., N$ denotes the iteration number of the Newton-Raphson method. Since the Newton-Raphson method is the second order convergence, normally, the convergence takes only a few steps.

4.4 Finite Element Method Implementations of the Galerkin Weak Formulation of Dynamic Wetting in Two Dimensions

In this section, we discuss implementations of Equation (4.15) for the two dimensional Finite Element Method. The calculation of the surface stress will be discussed in Chapter 5. Here a surface patch is an one dimensional element for two dimensional simulations as shown in Figure 4.4. In Figure 4.4, $\mathbf{x}$ denotes the global coordinate, $\mathbf{x}'$ denotes the local

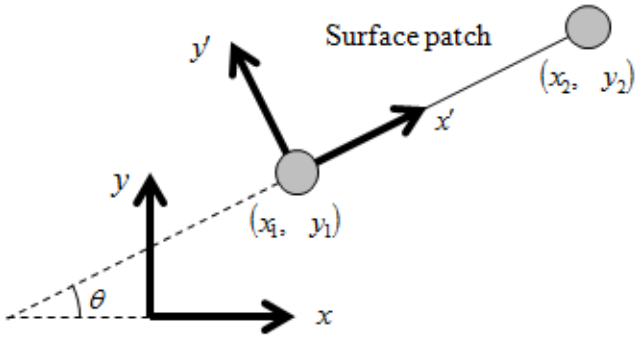

Figure 4.4: A surface patch in the two dimensional Finite Element Method.

coordinate that x' axis and y' axis are parallel and normal to the surface patch, and θ is the angle between x axis and x' axis. Then, the relationship between $\mathbf{x}$-axis and $\mathbf{x}'$-axis is given by

$$\mathbf{x}' = \mathbf{R}\mathbf{x}, \tag{4.26}$$

where

$$\mathbf{R} = \begin{pmatrix} \cos\theta & -\sin\theta \\ \sin\theta & \cos\theta \end{pmatrix} \tag{4.27}$$

$$= \frac{1}{L}\begin{pmatrix} x_2 - x_1 & y_1 - y_2 \\ y_2 - y_1 & x_2 - x_1 \end{pmatrix}, \tag{4.28}$$

where $L = |\mathbf{x}_2 - \mathbf{x}_1|$ is the length of the surface patch. The local coordinates of node i are given by

$$\mathbf{x}'_i = \mathbf{R}^T\mathbf{x}_i, \tag{4.29}$$

where $i = 1, 2$. Here, one dimensional FEM shape functions are used to compute the derivatives of FEM shape functions with respect to $\mathbf{x}'$, $\left[\frac{\partial N^i}{\partial \mathbf{x}'}\right]^T = \begin{bmatrix} \frac{\partial N^i}{\partial x'} & 0 \end{bmatrix}$, because y' components of $\mathbf{x}'_1$ and $\mathbf{x}'_2$ are zero. The derivatives of FEM shape functions with respect to $\mathbf{x}$, $\left[\frac{\partial N^i}{\partial \mathbf{x}}\right]^T = \begin{bmatrix} \frac{\partial N^i}{\partial x} & \frac{\partial N^i}{\partial y} \end{bmatrix}$, can be obtained by using the chain rule,

$$\frac{\partial {N^i}^T}{\partial \mathbf{x}} = \frac{\partial {N^i}^T}{\partial \mathbf{x}'} \frac{\partial \mathbf{x}'}{\partial \mathbf{x}}. \tag{4.30}$$

From equation (4.26), we have

$$\frac{\partial \mathbf{x}'}{\partial \mathbf{x}} = \mathbf{R}. \tag{4.31}$$

Thus, we obtain

$$\frac{\partial {N^i}^T}{\partial \mathbf{x}} = \frac{\partial {N^i}^T}{\partial \mathbf{x}'} \mathbf{R} \tag{4.32}$$

$$\frac{\partial N^i}{\partial \mathbf{x}} = \mathbf{R}^T \frac{\partial N^i}{\partial \mathbf{x}'}. \tag{4.33}$$

Once the surface stress is obtained, the Γ^{LG} and Γ^{LS} terms of Equation (4.14) can be then computed.

For the Γ^{SG} term of Equation (4.14), the solid-gas interface element is introduced. Figure 4.5 shows the solid-gas interface element in the two dimensional Finite Element Method. We

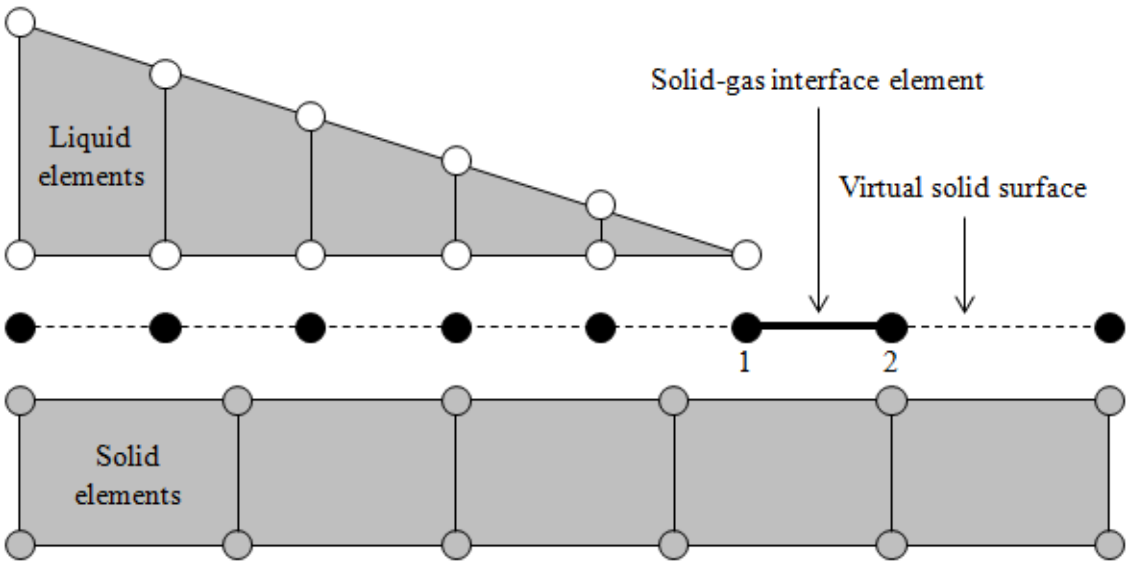

Figure 4.5: The solid-gas interface element in the two dimensional Finite Element Method.

only need the nodal force at node 1 in Figure 4.5, and the FEM shape function at node 1 is given by

$$N^1(x') = \frac{1}{L}(L - x'), \tag{4.34}$$

where L is the length of the solid-gas interface element, and x' is the local coordinate, $x' = 0$ at node 1 and $x' = L$ at node 2. The derivative of the FEM shape function with respect to $\mathbf{x}'$ is given by

$$\frac{\partial N^1}{\partial \mathbf{x}'} = \frac{1}{L}\begin{pmatrix} -1 \\ 0 \end{pmatrix}. \tag{4.35}$$

Thus, the term Γ^{SG} in Equation (4.14) can be written as

$$\int_{\Gamma^{SG}} \boldsymbol{\sigma}^{S,SG}\frac{\partial N^i}{\partial \mathbf{x}}ds = \int_{\Gamma^{SG}} \boldsymbol{\sigma}^{S,SG}\mathbf{R}^T\frac{1}{L}\begin{pmatrix} -1 \\ 0 \end{pmatrix}ds \tag{4.36}$$

$$\approx \frac{1}{2}\left\{\boldsymbol{\sigma}^{S,SG}(\mathbf{x}_1) + \boldsymbol{\sigma}^{S,SG}(\mathbf{x}_2)\right\}\mathbf{R}^T\begin{pmatrix} -1 \\ 0 \end{pmatrix}, \tag{4.37}$$

where the trapezoidal rule is used for the surface integration. In the case that $L \approx 0$, $\boldsymbol{\sigma}^{S,SG}(\mathbf{x}_1) \approx \boldsymbol{\sigma}^{S,SG}(\mathbf{x}_2)$. Finally, the term Γ^{SG} in Equation (4.15) is given by

$$\int_{\Gamma^{SG}} \boldsymbol{\sigma}^{S,SG}\frac{\partial N^1}{\partial \mathbf{x}}ds \approx \boldsymbol{\sigma}^{S,SG}(\mathbf{x}_1)\mathbf{R}^T\begin{pmatrix} -1 \\ 0 \end{pmatrix} \tag{4.38}$$

$$\approx \boldsymbol{\sigma}^{S,SG}(\mathbf{x}_1)\begin{pmatrix} -\cos\theta \\ \sin\theta \end{pmatrix}. \tag{4.39}$$

4.5 Finite Element Method Implementations of the Galerkin Weak Formulation of Dynamic Wetting in Three Dimensions

A surface patch is a two dimensional element for the three dimensional Finite Element Method, shown in Figure 4.6. In Figure 4.6, $\mathbf{x}$ denotes the global coordinate, $\mathbf{x}'$ denotes the local coordinate that x' is parallel to the unit vector $\mathbf{x}_{21} = (\mathbf{x}_2 - \mathbf{x}_1)/|\mathbf{x}_2 - \mathbf{x}_1|$, x'-y' plain is parallel to the surface patch, and z' axis is parallel to the normal vector of the surface patch $\mathbf{n}$. The unit vector of y' axis, $\mathbf{y}_1$, is obtained by

$$\mathbf{y}_1 = \frac{1}{|\mathbf{n} \times \mathbf{x}_{21}|}\mathbf{n} \times \mathbf{x}_{21}, \tag{4.40}$$

Then, the relationship between $\mathbf{x}$-axis and $\mathbf{x}'$-axis is given by

$$\mathbf{x}' = \mathbf{R}\mathbf{x}, \tag{4.41}$$

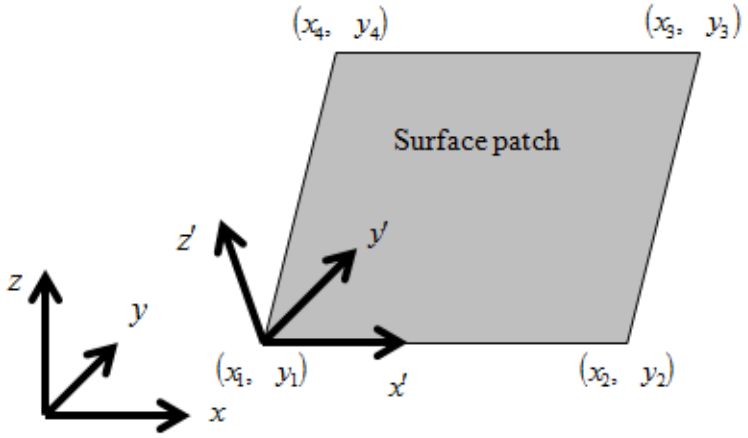

Figure 4.6: A surface patch in the three dimensional Finite Element Method.

where

$$\mathbf{R} = \begin{pmatrix} \mathbf{x}_{21} & \mathbf{y}_1 & \mathbf{n} \end{pmatrix}. \tag{4.42}$$

The local coordinates of node i, $i = 1, 2, 3, 4$, are given by

$$\mathbf{x}_i' = \mathbf{R}^T \mathbf{x}_i. \tag{4.43}$$

Two dimensional FEM shape functions can be applied to compute the derivatives of FEM shape functions with respect to $\mathbf{x}'$, $\left[\frac{\partial N^i}{\partial \mathbf{x}'}\right]^T = \begin{bmatrix} \frac{\partial N^i}{\partial x'} & \frac{\partial N^i}{\partial y'} & 0 \end{bmatrix}$, since z' components of $\mathbf{x}_i'$ is zero. The derivatives of FEM shape functions with respect to $\mathbf{x}$, $\left[\frac{\partial N^i}{\partial \mathbf{x}}\right]^T = \begin{bmatrix} \frac{\partial N^i}{\partial x} & \frac{\partial N^i}{\partial y} & \frac{\partial N^i}{\partial z} \end{bmatrix}$, can be obtained by using the chain rule, the same as the implementation in the two dimensional case.

The solid-gas interface element in the three dimensional Finite Element Method is shown in Figure 4.7. In Figure 4.7, L_1 is the length between node 1 and node 2, L_2 is the length between node 2 and node 3, and the shape of the solid-gas interface element is rectangular. We only need nodal forces at node 1 and 2 in Figure 4.7. FEM shape function at node 1 is given by

$$N^1(x', y') = \frac{1}{L_1 L_2}(L_1 - x')(L_2 - y'). \tag{4.44}$$

The derivative of the FEM shape function with respect to $\mathbf{x}'$ is given by

$$\frac{\partial N^1}{\partial \mathbf{x}'}(x', y') = \frac{1}{L_1 L_2} \begin{pmatrix} -(L_2 - y') \\ -(L_1 - x') \\ 0 \end{pmatrix}. \tag{4.45}$$

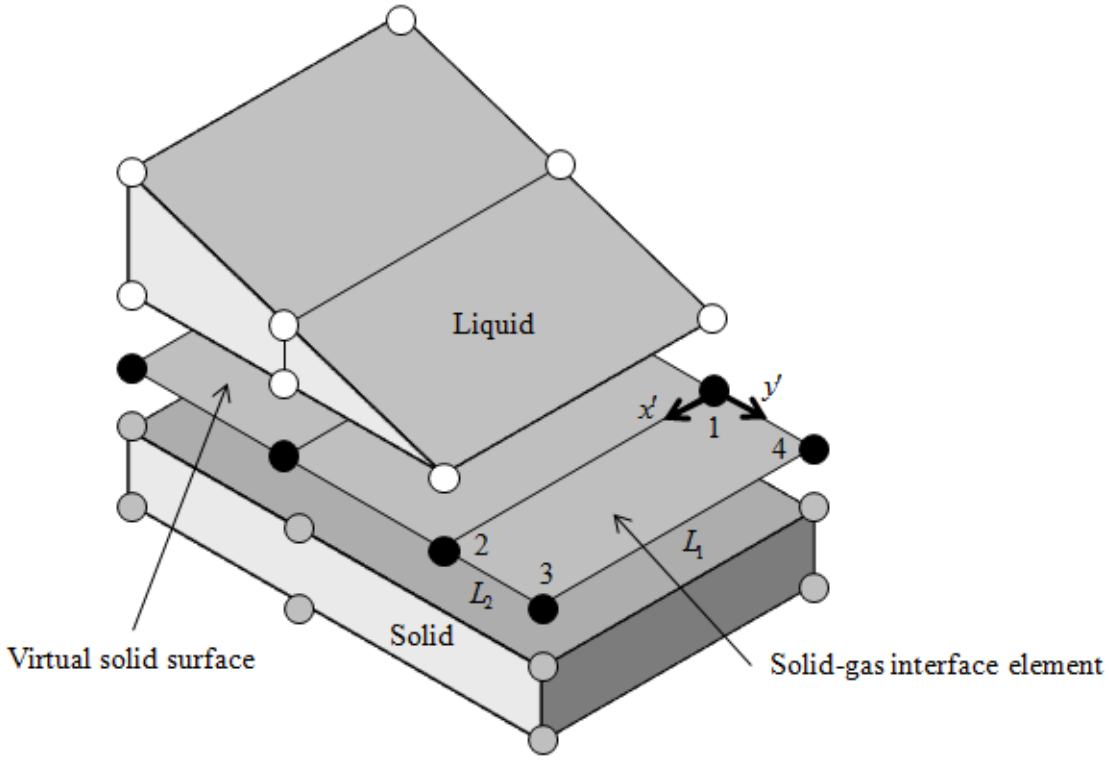

Figure 4.7: The solid-gas interface element in the three dimensional Finite Element Method.

Thus, the term Γ^{SG} in Equation (4.15) can be written as

$$\int_{\Gamma^{SG}} \boldsymbol{\sigma}^{S,SG} \frac{\partial N^i}{\partial \mathbf{x}} ds = \int_{\Gamma^{SG}} \boldsymbol{\sigma}^{S,SG} \mathbf{R}^T \frac{\partial N^1}{\partial \mathbf{x}'} (x', y')\, ds \tag{4.46}$$

$$\approx \frac{L_1 L_2}{4} \left\{ \boldsymbol{\sigma}^{S,SG}(\mathbf{x}_1)\, \mathbf{R}^T \frac{\partial N^1}{\partial \mathbf{x}'}(0,0) + \boldsymbol{\sigma}^{S,SG}(\mathbf{x}_2)\, \mathbf{R}^T \frac{\partial N^1}{\partial \mathbf{x}'}(L_1, 0) \right.$$

$$\left. \boldsymbol{\sigma}^{S,SG}(\mathbf{x}_3)\, \mathbf{R}^T \frac{\partial N^1}{\partial \mathbf{x}'}(L_1, L_2) + \boldsymbol{\sigma}^{S,SG}(\mathbf{x}_4)\, \mathbf{R}^T \frac{\partial N^1}{\partial \mathbf{x}'}(0, L_2) \right\} \tag{4.47}$$

$$\approx -\frac{1}{4} \left\{ \boldsymbol{\sigma}^{S,SG}(\mathbf{x}_1)\, \mathbf{R}^T \begin{pmatrix} L_2 \\ L_1 \\ 0 \end{pmatrix} + \boldsymbol{\sigma}^{S,SG}(\mathbf{x}_2)\, \mathbf{R}^T \begin{pmatrix} L_2 \\ 0 \\ 0 \end{pmatrix} \right.$$

$$\left. + \boldsymbol{\sigma}^{S,SG}(\mathbf{x}_4)\, \mathbf{R}^T \begin{pmatrix} 0 \\ L_1 \\ 0 \end{pmatrix} \right\}. \tag{4.48}$$

where the trapezoidal rule is applied to the surface integration. In the case that $L_2 \approx 0$,

$\boldsymbol{\sigma}^{S,SG}(\mathbf{x}_1) \approx \boldsymbol{\sigma}^{S,SG}(\mathbf{x}_4)$. Finally, the term Γ^{SG} in Equation (4.15) at node 1 is obtained as

$$\int_{\Gamma^{SG}} \boldsymbol{\sigma}^{S,SG} \frac{\partial N^1}{\partial \mathbf{x}} ds \approx -\frac{L_1}{2} \boldsymbol{\sigma}^{S,SG}(\mathbf{x}_1) \mathbf{R}^T \begin{pmatrix} 0 \\ 1 \\ 0 \end{pmatrix} \tag{4.49}$$

$$\approx -\frac{L_1}{2} \boldsymbol{\sigma}^{S,SG}(\mathbf{x}_1) \begin{pmatrix} x_{21y} \\ y_{1y} \\ n_y \end{pmatrix}. \tag{4.50}$$

Similarly, the term Γ^{SG} in Equation (4.15) at node 2 is given by

$$\int_{\Gamma^{SG}} \boldsymbol{\sigma}^{S,SG} \frac{\partial N^2}{\partial \mathbf{x}} ds \approx -\frac{L_1}{2} \boldsymbol{\sigma}^{S,SG}(\mathbf{x}_2) \mathbf{R}^T \begin{pmatrix} 0 \\ 1 \\ 0 \end{pmatrix} \tag{4.51}$$

$$\approx -\frac{L_1}{2} \boldsymbol{\sigma}^{S,SG}(\mathbf{x}_2) \begin{pmatrix} x_{21y} \\ y_{1y} \\ n_y \end{pmatrix}. \tag{4.52}$$

Chapter 5

Constitutive Models

5.1 The Newtonian Fluid Model

The Newtonian fluid is a fluid that the viscous stress is proportional to the shear strain rate. The formulation of the Newtonian fluid can be found in many references, for example, [2], [47], [60], [70], [78].

For viscous incompressible fluids, the Cauchy stress tensor $\boldsymbol{\sigma}$ can be decomposed into hydrostatic part and viscous part,

$$\boldsymbol{\sigma} = -p\mathbf{I} + \boldsymbol{\tau}, \tag{5.1}$$

where p is the hydrostatic pressure, and $\boldsymbol{\tau}$ is the viscous stress tensor. For the Newtonian fluids, the viscous stress tensor is related to the rate of deformation tensor $\mathbf{D}$,

$$\boldsymbol{\tau} = \mathbb{C} : \mathbf{D}, \tag{5.2}$$

where $\mathbb{C}$ is the forth order tensor of fluid properties.

For an isotropic fluid, the forth order tensor $\mathbb{C}$ can be expressed in terms of Lamé constants λ and μ,

$$\mathbb{C} = \lambda\mathbf{I} \otimes \mathbf{I} + 2\mu\mathbb{I}, \tag{5.3}$$

where $\mathbb{I}$ is the symmetric forth order identity tensor. Then, the viscous stress tensor is given by

$$\boldsymbol{\tau} = \lambda\,(tr\mathbf{D}) + 2\mu\mathbf{D}. \tag{5.4}$$

Because $tr\mathbf{D} = 0$ for an incompressible fluid, we obtain

$$\boldsymbol{\tau} = 2\mu\mathbf{D}. \tag{5.5}$$

The bulk modulus κ is defined as

$$\kappa = -V\frac{dp}{dV}, \tag{5.6}$$

where V is the volume. Alternatively, we can obtain the following expression by using density ρ,

$$\begin{aligned}\kappa &= -V\frac{\partial p}{\partial \rho}\frac{\partial \rho}{\partial V} \\ &= \rho\frac{\partial p}{\partial \rho}.\end{aligned} \tag{5.7}$$

After taking the integration, we have

$$p = \kappa \ln \frac{\rho}{\rho_0}, \tag{5.8}$$

where ρ_0 is the density in the reference configuration, and the pressure in the reference configuration is assumed to be zero. By using $\rho_0 = \rho J$, where J is the determinant of the deformation gradient tensor and can represent the volume ratio, we obtain the relationship between the pressure and the volume ratio,

$$p = -\kappa \ln J. \tag{5.9}$$

By substituting Equation (5.4) and (5.9) into Equation (5.1), we obtain the following constitutive model for the Newtonian fluid,

$$\boldsymbol{\sigma} = \kappa \left(\ln J\right) \mathbf{I} + 2\mu \mathbf{D}. \tag{5.10}$$

5.2 The Cauchy-Born Rule

The Cauchy-Born rule (see [3], [23], [86], and [98]) is suitable to model the uniform deformation of crystalline solid, and it links to the change of the lattice vectors.

Consider a crystalline solid that is consisting of n interacting atoms. The kinematics are represented by the vectors between two atoms i and j, which are $\mathbf{R}_{ij}$ and $\mathbf{r}_{ij}$ in the reference and current configuration,

$$\mathbf{R}_{ij} = \mathbf{R}_i - \mathbf{R}_j, \tag{5.11}$$

and

$$\mathbf{r}_{ij} = \mathbf{r}_i - \mathbf{r}_j. \tag{5.12}$$

The Cauchy-Born rule assumes that the deformation is locally homogeneous, i.e. the vectors $\mathbf{r}_{ij}$ resulting from the corresponding $\mathbf{R}_{ij}$ by the multiplication of the deformation gradient tensor $\mathbf{F}$,

$$\mathbf{r}_{ij} = \mathbf{F} \cdot \mathbf{R}_{ij}. \tag{5.13}$$

Equation (5.13) is the first order Cauchy-Born rule. The higher order Cauchy-Born rule, e.g. [29], [85], can be obtained by using Taylor series expansion. The second and third order

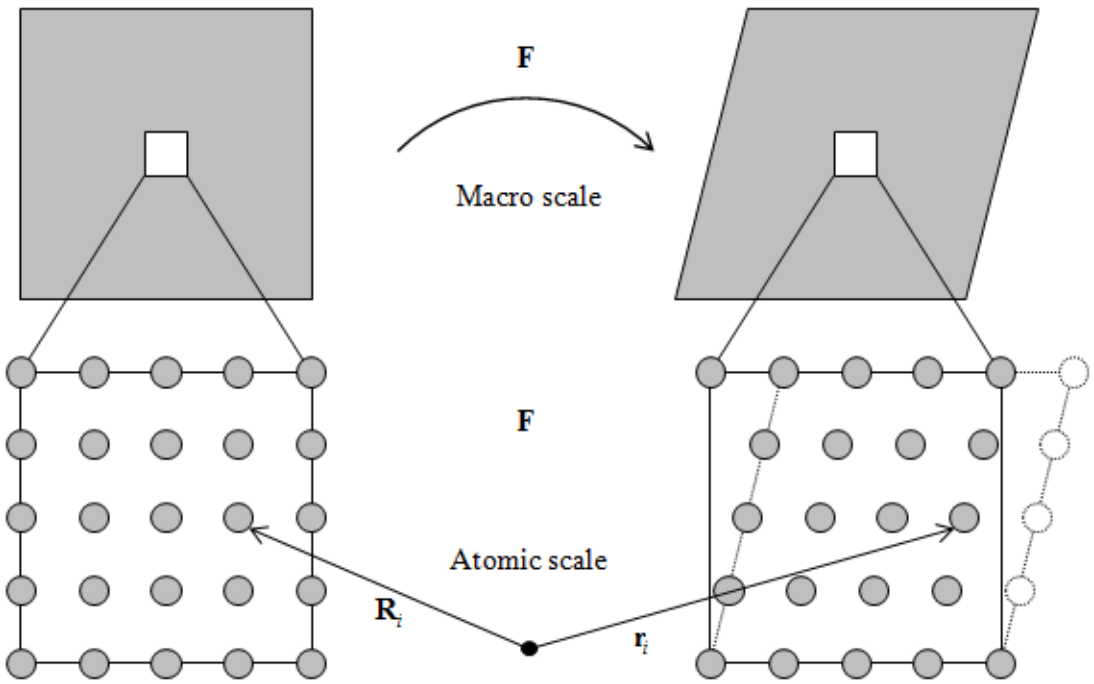

Figure 5.1: Locally homogeneous deformation in the atomic scale.

Cauchy-Born rules are given by

$$\mathbf{r}_{ij} = \mathbf{F} \cdot \mathbf{R}_{ij} + \frac{1}{2}\mathcal{G} : (\mathbf{R}_{ij} \otimes \mathbf{R}_{ij}), \tag{5.14}$$

and

$$\mathbf{r}_{ij} = \mathbf{F} \cdot \mathbf{R}_{ij} + \frac{1}{2}\mathcal{G} : (\mathbf{R}_{ij} \otimes \mathbf{R}_{ij}) + \frac{1}{6}\mathbb{H} \vdots (\mathbf{R}_{ij} \otimes \mathbf{R}_{ij} \otimes \mathbf{R}_{ij}), \tag{5.15}$$

where $\mathcal{G}$ and $\mathbb{H}$ are the higher order deformation gradient tensors,

$$\mathcal{G} = \frac{\partial^2 \mathbf{x}}{\partial \mathbf{X} \otimes \partial \mathbf{X}}, \tag{5.16}$$

and

$$\mathbb{H} = \frac{\partial^3 \mathbf{x}}{\partial \mathbf{X} \otimes \partial \mathbf{X} \otimes \partial \mathbf{X}}. \tag{5.17}$$

The calculation of the higher order deformation gradient tensor in the Finite Element Method is discussed in Appendix C.

The Pairwise Potential

It is useful to assume that the total energy E takes the form of a sum over pair bonds, like the Lennard-Jones potential,

$$E = \frac{1}{2}\sum_{i}^{n}\sum_{j\neq i}^{n}\phi\left(r_{ij}\right), \tag{5.18}$$

where $r_{ij} = |\mathbf{r}_{ij}|$ is the distance between atom i and j, and $\phi\left(r_{ij}\right)$ is the pairwise potential energy. Hence, the energy contribution of atom i is given by

$$E_i = \frac{1}{2}\sum_{j\neq i}^{n}\phi\left(r_{ij}\right). \tag{5.19}$$

For pair potential, the bonds between atoms are independent of each other.

The first Piola-Kirchhoff stress $\mathbf{P}$ can be obtained as the derivative of strain energy density W with respect to deformation gradient tensor,

$$\mathbf{P} = \frac{\partial W}{\partial \mathbf{F}} \tag{5.20}$$

$$= \frac{1}{\Omega_0}\frac{\partial E_i}{\partial \mathbf{F}}, \tag{5.21}$$

where Ω_0 is a representative volume in the reference configuration. The following expression can be obtained by substituting Equation (5.13) and (5.19) into Equation (5.21),

$$\mathbf{P} = \frac{1}{2\Omega_0}\sum_{j\neq i}^{n}\phi'\left(r_{ij}\right)\frac{\mathbf{r}_{ij}\otimes\mathbf{R}_{ij}}{r_{ij}}. \tag{5.22}$$

The higher order stresses can be expressed as follows,

$$\mathcal{Q} = \frac{1}{4\Omega_0}\sum_{j\neq i}^{n}\phi'\left(r_{ij}\right)\frac{\mathbf{r}_{ij}\otimes\mathbf{R}_{ij}\otimes\mathbf{R}_{ij}}{r_{ij}}, \tag{5.23}$$

and

$$\mathbb{T} = \frac{1}{12\Omega_0}\sum_{j\neq i}^{n}\phi'\left(r_{ij}\right)\frac{\mathbf{r}_{ij}\otimes\mathbf{R}_{ij}\otimes\mathbf{R}_{ij}\otimes\mathbf{R}_{ij}}{r_{ij}}. \tag{5.24}$$

The Cauchy stress is given as

$$\boldsymbol{\sigma} = \frac{1}{J}\mathbf{P}\cdot\mathbf{F}^T \tag{5.25}$$

$$= \frac{1}{2\Omega}\sum_{j\neq i}^{n}\phi'\left(r_{ij}\right)\frac{\mathbf{r}_{ij}\otimes\mathbf{r}_{ij}}{r_{ij}}. \tag{5.26}$$

The elastic tensor in the reference configuration is obtained as

$$\mathbb{C} = \frac{\partial \mathbf{S}}{\partial \mathbf{E}} \tag{5.27}$$

$$= \frac{1}{2\Omega_0} \sum_{j \neq i}^{n} \left(\phi'' \left(r_{ij} \right) - \frac{1}{r_{ij}} \phi' \left(r_{ij} \right) \right) \frac{\mathbf{R}_{ij} \otimes \mathbf{R}_{ij} \otimes \mathbf{R}_{ij} \otimes \mathbf{R}_{ij}}{r_{ij}^2}. \tag{5.28}$$

In Equation (5.28), one may find that the elastic tensor obtained by using the pair potential and the Cauchy-Born rule yields the following relation, $C_{1122} = C_{1212}$, which is called the Cauchy relation. In fact, rare gases have $C_{1122} : C_{1212}$ closer to 1, but for metallic FCC crystals the ratio $C_{1122} : C_{1212}$ is usually between 2 and 4, which indicates a strong presence of many-atom interactions, and this is supported by the experimental results [17].

The Embedded Atom Method

Daw and Baskes [15], [16], [17], [27] proposed the Embedded Atom Method as a many-atom potential for FCC metals. In this approach, the energy of the metal is viewed as the energy obtained by embedding an atom into the local electron density provided by the remaining atoms of the system. In addition, there is an electrostatic interaction. The total energy is given by

$$E = \frac{1}{2} \sum_{i}^{n} \sum_{j \neq i}^{n} \phi \left(r_{ij} \right) + \sum_{i}^{n} F \left(\rho_i \right), \tag{5.29}$$

where $\phi \left(r_{ij} \right)$ is an electrostatic, pairwise interaction, $F \left(\rho_i \right)$ is the embedding energy, and ρ_i is the atomic electron density,

$$\rho_i = \sum_{j \neq i}^{n} \rho \left(r_{ij} \right). \tag{5.30}$$

The embedding energy is defined as the interaction of the atom with the background electron gas. The background density for each atom is determined by evaluating or superposing the electron density tails of the other atoms at its nucleus site. Each atom is embedded in a host electron gas cloud created by its neighboring atoms. Hence, the energy contribution of atom i is given by

$$E_i = \frac{1}{2} \sum_{j \neq i}^{n} \phi \left(r_{ij} \right) + F \left(\rho_i \right). \tag{5.31}$$

The first Piola-Kirchhoff stress for the Embedded Atom Method can be expressed by

$$\mathbf{P} = \frac{1}{\Omega_0} \left\{ \sum_{j \neq i}^{n} \left(\frac{1}{2} \phi' \left(r_{ij} \right) + F_i' \left(\rho_i \right) \rho' \left(r_{ij} \right) \right) \frac{\mathbf{r}_{ij} \otimes \mathbf{R}_{ij}}{r_{ij}} \right\}. \tag{5.32}$$

The higher order stresses are given by

$$\mathcal{Q} = \frac{1}{2\Omega_0}\left\{\sum_{j\neq i}^{n}\left(\frac{1}{2}\phi'\left(r_{ij}\right) + F_i'\left(\rho_i\right)\rho'\left(r_{ij}\right)\right)\frac{\mathbf{r}_{ij}\otimes\mathbf{R}_{ij}\otimes\mathbf{R}_{ij}}{r_{ij}}\right\}, \tag{5.33}$$

and

$$\mathbb{T} = \frac{1}{6\Omega_0}\left\{\sum_{j\neq i}^{n}\left(\frac{1}{2}\phi'\left(r_{ij}\right) + F_i'\left(\rho_i\right)\rho'\left(r_{ij}\right)\right)\frac{\mathbf{r}_{ij}\otimes\mathbf{R}_{ij}\otimes\mathbf{R}_{ij}\otimes\mathbf{R}_{ij}}{r_{ij}}\right\}. \tag{5.34}$$

The Cauchy stress is given by

$$\boldsymbol{\sigma} = \frac{1}{\Omega}\left\{\sum_{j\neq i}^{n}\left(\frac{1}{2}\phi'\left(r_{ij}\right) + F_i'\left(\rho_i\right)\rho'\left(r_{ij}\right)\right)\frac{\mathbf{r}_{ij}\otimes\mathbf{r}_{ij}}{r_{ij}}\right\}, \tag{5.35}$$

where Ω is a representative volume in the current configuration.

The elastic tensor in the reference configuration is given by

$$\begin{aligned}\mathbb{C} = \frac{1}{\Omega_0}\Bigg\{&\frac{1}{2}\sum_{j\neq i}\left(\phi''\left(r_{ij}\right) - \frac{1}{r_{ij}}\phi'\left(r_{ij}\right)\right)\frac{\mathbf{R}_{ij}\otimes\mathbf{R}_{ij}\otimes\mathbf{R}_{ij}\otimes\mathbf{R}_{ij}}{r_{ij}^2}\\ &+ F_i''\left(\rho_i\right)\left(\sum_{j\neq i}\rho'\left(r_{ij}\right)\frac{\mathbf{R}_{ij}\otimes\mathbf{R}_{ij}}{r_{ij}}\right)\otimes\left(\sum_{j\neq i}\rho'\left(r_{ij}\right)\frac{\mathbf{R}_{ij}\otimes\mathbf{R}_{ij}}{r_{ij}}\right)\\ &+F_i'\left(\rho_i\right)\sum_{j\neq i}\left(\rho''\left(r_{ij}\right) - \frac{1}{r_{ij}}\rho'\left(r_{ij}\right)\right)\frac{\mathbf{R}_{ij}\otimes\mathbf{R}_{ij}\otimes\mathbf{R}_{ij}\otimes\mathbf{R}_{ij}}{r_{ij}^2}\Bigg\}.\end{aligned} \tag{5.36}$$

For the Embedded Atom Method, C_{1122} is not equal to C_{1212} due to the existence of the second term on the right hand side in Equation (5.36). Several models of the pairwise interaction and embedding energy function are proposed, for example, Mishin et al. [45], [57], [58], Wadley et al. [92], [93], [101], [102], and Holian et al. [38], [39], [94]. These models are discussed in Appendix D.

5.3 The Gurtin-Murdoch Surface Elasticity Model

In this section, we discuss a constitutive model on the surface. One of few continuum surface mechanics models is the Gurtin-Murdoch surface elasticity model [30], [31], [32]. This model is widely discussed, and the following discussion mainly follows references [50] and [80].

Before the discussion of the constitutive model, construct the surface operators. A projection operator $\mathbf{P}$ which maps tensor fields from bulk to surface is defined as

$$\mathbf{P} = \mathbf{I} - \mathbf{n}\otimes\mathbf{n}, \tag{5.37}$$

where $\mathbf{I}$ is a unit second order tensor, $\mathbf{n}$ is the normal vector of the surface, and thus the projection tensor $\mathbf{P}$ is symmetric. A surface second order unit tensor is defined as the result of the projection of a unit second order tensor,

$$\mathbf{I}^S = \mathbf{P} \cdot \mathbf{I} \cdot \mathbf{P} \tag{5.38}$$

$$= \mathbf{P}. \tag{5.39}$$

Thus, a surface second order unit tensor $\mathbf{I}^S$ is exactly the same as the projection tensor $\mathbf{P}$. We now construct an interface differentiation operator or a gradient operator ∇^S. It is defined as

$$\nabla^S = \mathbf{P} \cdot \nabla \tag{5.40}$$

$$= \nabla - \mathbf{n} \left(\mathbf{n} \cdot \nabla \right). \tag{5.41}$$

The surface strain is defined as the projection of bulk strain field to the surface,

$$\boldsymbol{\epsilon}^S = \mathbf{P} \cdot \boldsymbol{\epsilon} \cdot \mathbf{P}, \tag{5.42}$$

where $\boldsymbol{\epsilon}^S$ is the surface strain, and $\boldsymbol{\epsilon}$ is the bulk strain. On the other hand, the Cauchy stress is not continuous across the surface. In addition, the unit of the surface stress $[N/m]$ and the bulk stress $[N/m^2]$ are different. Therefore, one cannot link the surface stress with the bulk stress by the projection operator. They have to be related with surface constitutive relations, which are different from the bulk material properties, or they are not the projection of bulk material properties either. The surface stress is related with the surface energy,

$$\boldsymbol{\sigma}^S = \gamma \mathbf{I}^S + \frac{\partial \Gamma}{\partial \boldsymbol{\epsilon}^S} + \gamma \nabla^S \mathbf{u}, \tag{5.43}$$

where $\boldsymbol{\sigma}^S$ is the surface stress tensor, γ is the (deformation-independent) surface energy, and Γ is the deformation-dependent surface energy. In the Gurtin-Murdoch theory, the surface energy may be understood as the residual surface stress due to the surface relaxation. For infinitesimal deformation cases, Gurtin and Murdoch proposed the following quadratic form of the surface energy,

$$\Gamma = \frac{1}{2} \boldsymbol{\epsilon}^S : \mathbb{C}^S : \boldsymbol{\epsilon}^S, \tag{5.44}$$

where $\mathbb{C}^S$ is the forth order surface elastic tensor. It is related to the (deformation-independent) surface energy γ and the surface lamé constants λ^S and μ^S,

$$\mathbb{C}^S = \left(\lambda^S + \gamma \right) \mathbf{I} \otimes \mathbf{I} + 2 \left(\mu^S - \gamma \right) \mathbb{I}, \tag{5.45}$$

where $\mathbb{I}$ is the symmetric forth order identity tensor,

$$\mathbb{I} = \frac{1}{2} \left(\delta_{ik} \delta_{jl} + \delta_{il} \delta_{jk} \right). \tag{5.46}$$

Thus, the surface stress is given by

$$\boldsymbol{\sigma}^S = \gamma \mathbf{I}^S + \left(\lambda^S + \gamma \right) \left(tr \boldsymbol{\epsilon}^S \right) \mathbf{I}^S + 2 \left(\mu^S - \gamma \right) \boldsymbol{\epsilon}^S + \gamma \nabla^S \mathbf{u}. \tag{5.47}$$

5.4 The Surface Cauchy-Born Rule

In this section, we discuss the surface Cauchy-Born rule [61], [64], [65] that the total atomistic potential energy of a body is represented by continuum energy densities with appropriate representations for surface energy densities. The total energy of the body is approximated as

$$E = \int_{\Omega} \phi\left(r_{ij}\right) d\Omega + \int_{\Gamma} \gamma\left(r_{ij}\right) d\Gamma, \tag{5.48}$$

where $\gamma\left(r_{ij}\right)$ is the surface energy density, Γ denotes the surface area. Not only the surface layer, but also the non-bulk layer do not have a full complement of atomic neighbors, shown in Figure 5.2. Hence, the surface energy density can be written as

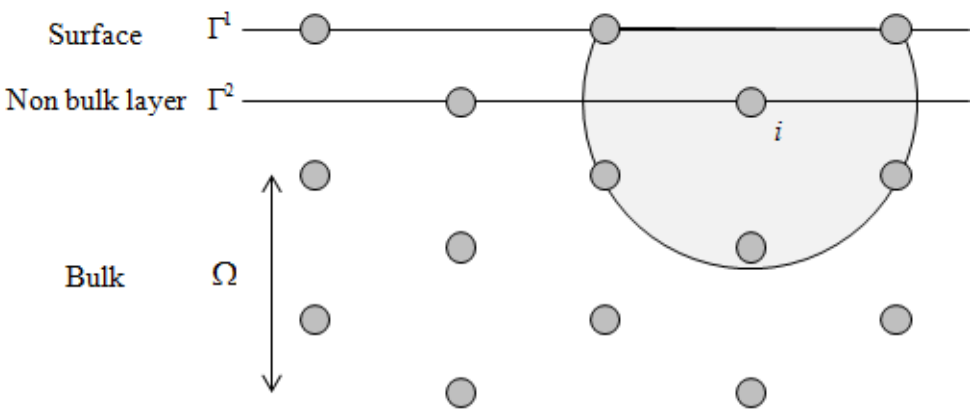

Figure 5.2: Illustration of the surface Cauchy-Born rule.

$$\int_{\Gamma} \gamma\left(r_{ij}\right) d\Gamma = \int_{\Gamma_{surface}} \gamma\left(r_{ij}\right) d\Gamma + \int_{\Gamma_{non-bulk}} \gamma\left(r_{ij}\right) d\Gamma. \tag{5.49}$$

The surface energy density can be expressed as

$$\gamma\left(r_{ij}\right) = \frac{1}{2\Gamma} \sum_{i}^{n} \sum_{j \neq i}^{nb_i} \phi\left(r_{ij}\right), \tag{5.50}$$

where nb_i is the number of bonds for surface atom i. The surface first Piola-Kirchhoff and Cauchy stress can be obtained by applying the Cauchy-Born rule, Equation (5.13), to Equation (5.50),

$$\mathbf{P}^s = \frac{1}{2\Gamma_0} \sum_{j \neq i}^{nb_i} \phi'\left(r_{ij}\right) \frac{\mathbf{r}_{ij} \otimes \mathbf{R}_{ij}}{r_{ij}}, \tag{5.51}$$

and

$$\boldsymbol{\sigma}^s = \frac{1}{2\Gamma} \sum_{j \neq i}^{nb_i} \phi' \left(r_{ij} \right) \frac{\mathbf{r}_{ij} \otimes \mathbf{r}_{ij}}{r_{ij}}. \tag{5.52}$$

Due to the un-even presence of atom distribution on the surface and non-bulk layer, the residual surface stress exists in the undeformed state. This residual surface stress is the surface energy in the Surface Cauchy-Born rule. The number of non-bulk layers depends on the cutoff distance, i.e. the number of non-bulk layers is two when the atom consider the third nearest neighbors. Hence, at least the second nearest neighbors must be considered to compute the surface stress in the surface Cauchy-Born rule. The surface stress in the surface Cauchy-Born rule has the normal components, and it allows the surface relaxation due to under co-ordinated atoms lying on material surfaces [65].

The Embedded Atom Method is applied to the surface Cauchy-Born rule for FCC metals [63], and the surface first Piola-Kirchhoff and Cauchy stress are given by

$$\mathbf{P}^s = \frac{1}{\Gamma_0} \left\{ \sum_{j \neq i}^{nb_i} \left(\frac{1}{2} \phi' \left(r_{ij} \right) + F_i' \left(\rho_i \right) \rho' \left(r_{ij} \right) \right) \frac{\mathbf{r}_{ij} \otimes \mathbf{R}_{ij}}{r_{ij}} \right\}, \tag{5.53}$$

and

$$\boldsymbol{\sigma}^s = \frac{1}{\Gamma} \left\{ \sum_{j \neq i}^{nb_i} \left(\frac{1}{2} \phi' \left(r_{ij} \right) + F_i' \left(\rho_i \right) \rho' \left(r_{ij} \right) \right) \frac{\mathbf{r}_{ij} \otimes \mathbf{r}_{ij}}{r_{ij}} \right\}. \tag{5.54}$$

Chapter 6

The Coarse Grained Contact Model

This section provides an overview of the Finite Element Method based Coarse Grained Contact Model developed by R. Sauer and S. Li [73], [74], [75], [76], [77]. Small scale contact phenomena is modelled by Johnson, Kendall and Roberts, JKR theory [44], and Derjaguin, Muller and Toporov, DMT theory [20]. These models have been successfully applied to study many areas, but they are restricted to infinitesimal deformations [43].

The objective of the Coarse Grained Contact Model is to describe repulsive and adhesive interactions based on atomic physics between bodies. The model is related to Molecular Dynamics and the continuum contact mechanics.

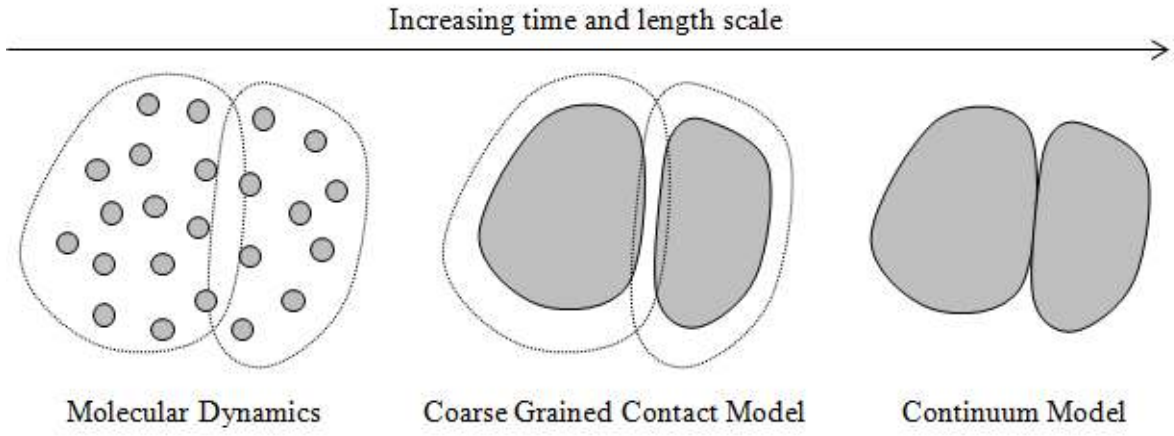

Figure 6.1: An overview of the Coarse Grained Contact Model.

At the atomic scale the behavior is governed by interactions among individual atoms. Molecular Dynamics is a discrete model, which describes the interaction of an assembly of point masses, molecules or atoms. The particle interaction is modelled by intermolecular interaction potentials. The inter-solid potential is often weak but long-range, for example,

the van der Waals interaction. The Molecular Dynamics simulations are less useful for large length and time scales because of the computational cost.

On the other hand, at large scale interactions between two bodies are described by continuum approach. Continuum mechanics offers a formulation which is well established for macroscale problems, and the contact of two bodies is often modelled as a global constrained problem. The classical continuum approaches to nanoscale problems are typically based on phenomenological models and lack the atomistic physics.

The basic idea of the Coarse Grained Contact Model is to enrich the continuum formulation with atomistic information. This is achieved by the coarse-graining, or homogenization, of the Molecular Dynamics model. The inter-solid interaction is homogenized so it may be represented by a continuum interaction energy. By the homogenization of the inter-solid potential, a continuous interaction energy that is surrounding each body is obtained.

The van der Waals force is a general name for three different dipole interactions: (1) the Keesom interaction based on the mutual alignment of permanent dipoles, (2) the Debye interaction for the coupling between the permanent dipole and the molecular polarizability at zero frequency, and (3) the London interaction for the correlation between inducible dipoles, occurring at all frequencies, all of which are attractive in vacuum and proportional to $1/r^6$ [42], [66]. In contrast to covalent, ionic or metallic bonds, which are short range and are the predominant interaction within solids, the van der Waals interactions are long range, and a suitable model for inter-solid interactions. Due to its proportionally to $1/r^6$, the van der Waals interaction is often modelled by the Lennard-Jones potential,

$$\phi(r) = \epsilon \left(\frac{r_0}{r}\right)^{12} - 2\epsilon \left(\frac{r_0}{r}\right)^{6}, \tag{6.1}$$

where the first term is the repulsion when two atoms become close, the second term is the contribution of the van der Waals force, ϵ is the depth of the potential well, r_0 is the equilibrium distance, and r is the distance between two atoms.

6.1 A Weak Form of the Coarse Grained Contact Model

Figure 6.2 shows the kinematics of two interacting bodies in the framework of continuum mechanics. The bodies are denoted by $\mathbf{x}_1 \in \Omega_1$ and $\mathbf{x}_2 \in \Omega_2$ in the current configuration, β_1 and β_2 are the atomic densities, and r is the distance between two points. Interaction over all points leads to the interaction energy Π^C for the two interacting bodies may be written as

$$\Pi^C = \int_{\Omega_1} \int_{\Omega_2} \beta_1 \beta_2 \phi(r)\, dv_2 dv_1, \tag{6.2}$$

where $\phi(r)$ is the inter-atomic potential, here we use the Lennard-Jones potential as the inter-atomic potential.

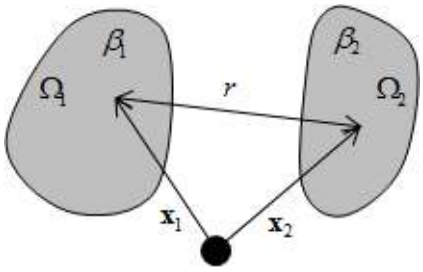

Figure 6.2: The kinematics of two interacting bodies.

Consider conservative systems. The total Lagrange of the system is given as

$$L = \sum_{I=1}^{2} \left[T_I - (\Pi_I^{int} - \Pi_I^{ext}) \right] - \Pi^C, \tag{6.3}$$

where $I = 1, 2$ denotes the two bodies, T_I are the kinetic energy, Π_I^{int} are the internal energy, and Π_I^{ext} are the external energy.

Consider the stationary condition $\delta L = 0$. We have

$$\delta L = \sum_{I=1}^{2} \left[\delta T_I - (\delta \Pi_I^{int} - \delta \Pi_I^{ext}) \right] - \delta \Pi^C = 0, \quad \forall \delta \mathbf{u}_1, \delta \mathbf{u}_2 \in H^1(\Omega_1) \cup H^1(\Omega_2), \tag{6.4}$$

where $\delta \mathbf{u}_1$ and $\delta \mathbf{u}_2$ are the variation of displacements. The variation of the kinetic energy is given by

$$\delta T_I = -\int_{\Omega_I} \frac{1}{2} \rho \mathbf{v}_I \cdot \delta \dot{\mathbf{u}}_I dv_I, \tag{6.5}$$

where ρ is the density in the current configuration, and $\mathbf{v}$ is the velocity. The variation of the internal energy is given by

$$\delta \Pi_I^{int} = \int_{\Omega_I} \boldsymbol{\sigma}_I : \frac{\partial \delta \mathbf{u}_I}{\partial \mathbf{x}_I} dv_I. \tag{6.6}$$

The variation of the external energy is expressed as

$$\delta \Pi_I^{ext} = \int_{\Omega_I} \rho_I \mathbf{b}_I \cdot \delta \mathbf{u}_I dv_I + \int_{\partial \Omega_I} \rho_I \mathbf{t}_I \cdot \delta \mathbf{u}_I ds_I, \tag{6.7}$$

where $\mathbf{b}$ is the body force, and $\mathbf{t}$ is the surface traction. The variation of the interaction energy is given by

$$\delta \Pi^C = \int_{\Omega_1} \int_{\Omega_2} \beta_1 \beta_2 \left(\frac{\partial \phi(r)}{\partial \mathbf{x}_1} \cdot \delta \mathbf{u}_1 + \frac{\partial \phi(r)}{\partial \mathbf{x}_2} \cdot \delta \mathbf{u}_2 \right) dv_2 dv_1. \tag{6.8}$$

Finally we obtain the following variational equation,

$$\sum_{I=1}^{2}\left[\int_{\Omega_I}\frac{1}{2}\rho_I\mathbf{v}_I\cdot\delta\dot{\mathbf{u}}_I dv_I+\int_{\Omega_I}\boldsymbol{\sigma}_I:\frac{\partial\delta\mathbf{u}_I}{\partial\mathbf{x}_I}dv_I-\int_{\Omega_I}\rho_I\mathbf{b}_I\cdot\delta\mathbf{u}_I dv_I-\int_{\partial\Omega_I}\rho_I\mathbf{t}_I\cdot\delta\mathbf{u}_I ds_I\right]$$
$$+\int_{\Omega_1}\int_{\Omega_2}\beta_1\beta_2\left(\frac{\partial\phi(r)}{\partial\mathbf{x}_1}\cdot\delta\mathbf{u}_1+\frac{\partial\phi(r)}{\partial\mathbf{x}_2}\cdot\delta\mathbf{u}_2\right)dv_2dv_1=0,\quad\forall\delta\mathbf{u}_1,\delta\mathbf{u}_2. \quad (6.9)$$

This is the basic weak formulation of the Coarse Grained Contact Model. Two of the main features of the Coarse Grained Contact Model are: (1) there is always a finite gap between the two contact surfaces because of repulsive forces, and (2) the Coarse Grained Contact Model theory is established for general nonlinear deformable solids. Therefore, even though there is stress concentration at the corner of contact line, there is no stress singularity at the corner of contact line as shown in Figure 6.3, which provide a potential remedy for the dilemma of previous hydrodynamic contact line theory.

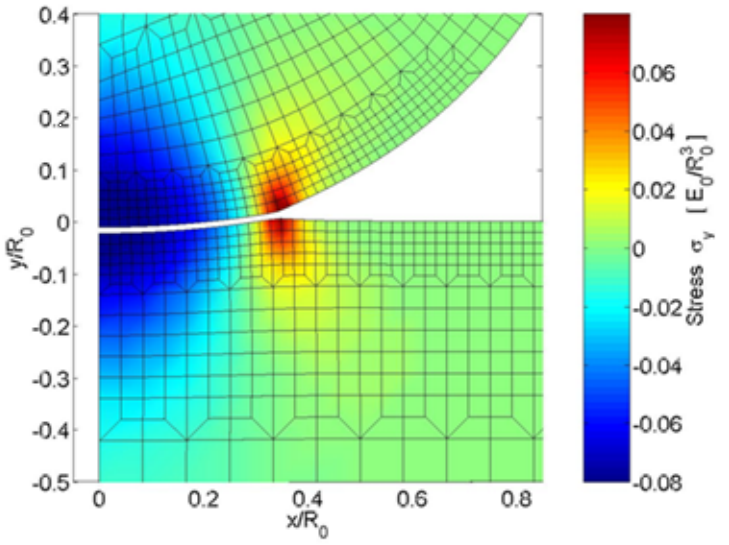

Figure 6.3: The Coarse Grained Contact Model simulation of adhesive contact [77].

6.2 A Finite Element Method Formulation of the Coarse Grained Contact Model

This section discusses the discretization of weak form of the Coarse Grained Contact Model into the Finite Element Method. The FEM interpolations are

$$\mathbf{u} = \sum_{i=1}^{nnode} N^i \mathbf{d}^i, \tag{6.10}$$

and

$$\delta\mathbf{u} = \sum_{i=1}^{nnode} N^i \delta\mathbf{d}^i, \tag{6.11}$$

where *nnode* is the number of nodes, N^i are FEM shape functions of the i-th node, and $\mathbf{d}^i$ and $\delta\mathbf{d}^i$ are the displacement of node i and its variation. We apply the FEM interpolations to weak form of the Coarse Grained Contact Model,

$$\begin{aligned}
0 = &\sum_{I=1}^{2}\sum_{e=1}^{nelem}\sum_{i=1}^{nnode}\sum_{j=1}^{nnode} \delta\mathbf{d}_I^i \cdot \int_{\Omega_{0eI}} \rho_{0I} N^i N^j \mathbf{a}_I^j dV_I + \sum_{I=1}^{2}\sum_{e=1}^{nelem}\sum_{i=1}^{nnode} \delta\mathbf{d}_I^i \cdot \int_{\Omega_{0eI}} \mathbf{P}_I \frac{\partial N^i}{\partial \mathbf{X}_I} dV_I \\
&- \sum_{I=1}^{2}\sum_{e=1}^{nelem}\sum_{i=1}^{nnode} \delta\mathbf{d}_I^i \cdot \int_{\Omega_{0eI}} \rho_{0I} N^i \mathbf{b}_I dV_I - \sum_{I=1}^{2}\sum_{e=1}^{nelem}\sum_{i=1}^{nnode} \delta\mathbf{d}_I^i \cdot \int_{\partial\Omega_{0eI}} \rho_{0I} N^i \mathbf{T}_I dS_I \\
&+ \sum_{I=1}^{2}\sum_{e_1=1}^{nelem}\sum_{e_2=1}^{nelem}\sum_{i=1}^{nnode} \delta\mathbf{d}_I^i \cdot \mathbf{f}_I^{C,i}, \quad \forall \delta\mathbf{d}_1, \delta\mathbf{d}_2,
\end{aligned} \tag{6.12}$$

where

$$\mathbf{f}_1^{C,i} = \int_{\Omega_{e1}} \int_{\Omega_{e2}} \beta_1 \beta_2 N_1^i \frac{\partial \phi(r)}{\partial \mathbf{x}_1} dv_2 dv_1, \tag{6.13}$$

and

$$\mathbf{f}_2^{C,i} = \int_{\Omega_{e1}} \int_{\Omega_{e2}} \beta_1 \beta_2 N_2^i \frac{\partial \phi(r)}{\partial \mathbf{x}_2} dv_2 dv_1, \tag{6.14}$$

where

$$\frac{\partial \phi(r)}{\partial \mathbf{x}_1} = \frac{\partial \phi(r)}{\partial r}\frac{\partial r}{\partial \mathbf{x}_1} \tag{6.15}$$

$$= \frac{\partial \phi(r)}{\partial r}\frac{\mathbf{x}_1 - \mathbf{x}_2}{r}, \tag{6.16}$$

and

$$\frac{\partial \phi(r)}{\partial \mathbf{x}_2} = \frac{\partial \phi(r)}{\partial r}\frac{\partial r}{\partial \mathbf{x}_2} \tag{6.17}$$

$$= \frac{\partial \phi(r)}{\partial r}\frac{\mathbf{x}_2 - \mathbf{x}_1}{r}. \tag{6.18}$$

Since $\delta\mathbf{d}_I$ is arbitrary, we can obtain the following equation,

$$\mathbf{M}_I\ddot{\mathbf{d}} = \mathbf{F}_I^{ext} - \mathbf{F}_I^{int} - \mathbf{F}_I^{cnt}, \tag{6.19}$$

where

$$\mathbf{M}_I = \sum_{e=1}^{nelem}\sum_{i=1}^{nnode}\sum_{j=1}^{nnode}\int_{\Omega_{0eI}} \rho_{0I} N^i N^j \mathbf{a}_I^j dV_I, \tag{6.20}$$

$$\mathbf{F}_I^{int} = \sum_{e=1}^{nelem}\sum_{i=1}^{nnode}\int_{\Omega_{0eI}} \mathbf{P}_I \frac{\partial N^i}{\partial \mathbf{X}_I} dV_I, \tag{6.21}$$

$$\mathbf{F}_I^{ext} = \sum_{e=1}^{nelem}\sum_{i=1}^{nnode}\int_{\Omega_{0eI}} \rho_{0I} N^i \mathbf{b}_I dV_I + \sum_{e=1}^{nelem}\sum_{i=1}^{nnode}\int_{\partial\Omega_{0eI}} \rho_{0I} N^i \mathbf{T}_I dS_I, \tag{6.22}$$

$$\mathbf{F}_I^{cnt} = \sum_{e_1=1}^{nelem}\sum_{e_2=1}^{nelem}\sum_{i=1}^{nnode} \mathbf{f}_I^{C,i}, \tag{6.23}$$

and $I = 1, 2$. This is the Finite Element Method formulation for the Coarse Grained Contact Model. As a characteristic of the Finite Element Method, the volume integration is carried out by the summation over small sub domains, i.e. the summation over elements.

6.3 The Numerical Integration of Two Bodies

In this section, we discuss the numerical integration to Equation (6.13) and (6.14). Since there are spatial integrations that involve two continuum bodies, for simplicity, we call this method body-body interaction method.

The Gaussian Quadrature Rule

The Gaussian quadrature rule is generally used as the numerical integration scheme in the Finite Element Method due to the high accuracy, which is $2n-1$, where n is the number of quadrature points. The Gaussian quadrature rule is stated as

$$\int_{-1}^{1} f(x) \approx \sum_{i=1}^{n} w_i f(x_i), \tag{6.24}$$

where w_i and x_i are the weight and position of quadrature point i. For $n = 2$, the weights are $w_1 = w_2 = 1$, and the positions are $x_1 = -1/\sqrt{3}$ and $x_2 = 1/\sqrt{3}$. Also, for $n = 3$, the weights are $w_1 = w_3 = 5/9$ and $w_2 = 8/9$, and the positions are $x_1 = -\sqrt{3/5}$, $x_2 = 0$ and $x_3 = \sqrt{3/5}$. Multi-dimensional integrals over product domains can be evaluated numerically using multiple summations. Figure 6.4 show the quadrature points of the Gaussian quadrature

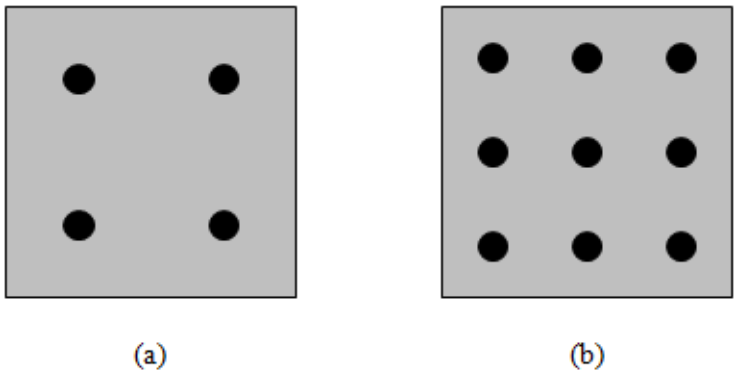

Figure 6.4: The quadrature points of the Gaussian quadrature rule in a two dimensional quadrilateral element: (a) $n = 2$, (b) $n = 3$.

rule for $n = 2, 3$ of a two dimensional quadrilateral element. Based on Equation (6.24), the function is evaluated at each quadrature point. Thus, the distance r in Equation (6.13) and (6.14) means the distance between quadrature points of two different elements in the body 1 and the body 2. For $n = 2$ of a two dimensional quadrilateral element case, we need

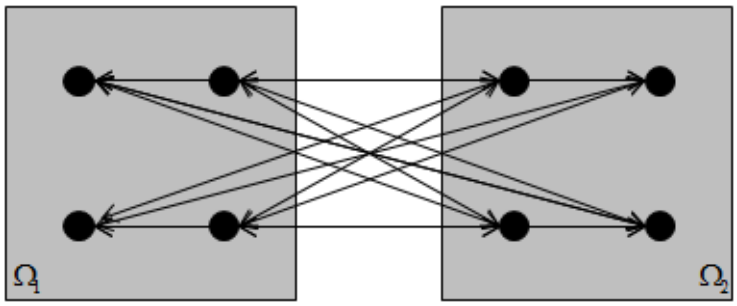

Figure 6.5: Volume integration of two bodies.

to evaluate $4 \times 4 = 16$ times, since there are two volume integrations, as shown in Figure 6.5. Thus, this body-body interaction method is actually law efficiency, and also there is an element size problem. Since the quadrature points of the Gaussian quadrature rule are inside of elements, elements of the body 1 and the body 2 penetrate when the element size is large compared to the equilibrium distance. Because the equilibrium distance r_0 of the Lennard-Jones potential is generally at the order of the angstrom $[10^{-10}m]$, the corresponding element size should also be at the order of the angstrom. Increasing the quadrature points can achieve accuracy, but it will increase the computational cost.

The Newton-Cotes Quadrature Rule

On the other hand, the Newton-Cotes quadrature rule is hardly used as the numerical volume integration in the Finite Element method, since the accuracy is only at the order of $n-1$, where n is the number of quadrature points. However, when the Newton-Cotes quadrature is used for the Coarse Grained Contact Model, it may provide computational efficiency. For $n=2$, called the trapezoidal rule, the weights are $w_1 = w_2 = 1/2$, and the positions are $x_1 = -1$ and $x_2 = 1$. Also, for $n=3$, called the Simpson's rule, the weights are $w_1 = w_3 = 1/3$ and $w_2 = 4/3$, and the positions are $x_1 = -1$, $x_2 = 0$ and $x_3 = 1$.

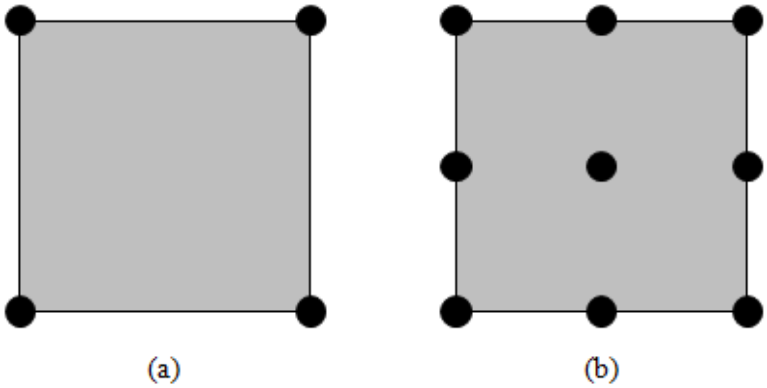

Figure 6.6: The quadrature points of the Newton-Cotes quadrature rule in a two dimensional quadrilateral element: (a) $n=2$, (b) $n=3$.

6.4 The Analytical Integration of the Master Body

In addition to the element size problem, there is an error which comes from the unbalance of the distance between quadrature points for both the Gaussian and Newton-Cotes quadrature rule. For simplicity, here we consider only the attraction force, the van der Waals force, of the Lennard-Jones potential in Figure 6.7. In case the surface of the master body is infinite flat surface, the force which acts on the slave quadrature point in the parallel direction must be zero analytically. Since the quadrature point b in Figure 6.7 is the closest to the slave quadrature point, the slave quadrature point attract to the quadrature point b strongly, and there exist the force in the parallel direction of the master body surface. This error comes from the unbalance of the distance between quadrature points.

To solve these problems, we developed the new method which we perform the analytical integration to the master body. In Equation (6.12), the body 2 is the master body from the

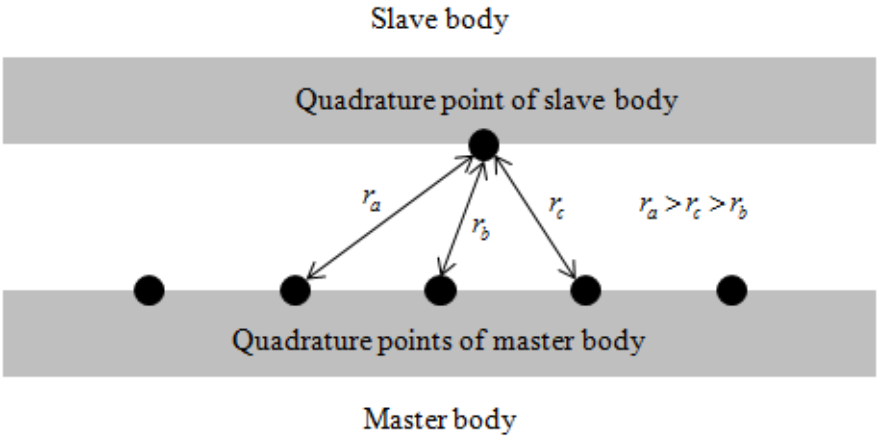

Figure 6.7: The unbalance of the distance between quadrature points.

view of the body 1, thus,

$$\begin{aligned}\mathbf{f}_1^{C,i} &= \int_{\Omega_1}\int_{\Omega_2} \beta_1\beta_2 N_1^i \frac{\partial\phi\left(r\right)}{\partial r}\frac{\mathbf{x}_1-\mathbf{x}_2}{r}dv_2dv_1 \\ &= \int_{\Omega_1} \beta_1 N_1^i \tilde{\mathbf{f}}_2^C dv_1, \end{aligned} \tag{6.25}$$

where

$$\tilde{\mathbf{f}}_2^C = \int_{\Omega_2} \beta_2 \frac{\partial\phi\left(r\right)}{\partial r}\frac{\mathbf{x}_1-\mathbf{x}_2}{r}dv_2. \tag{6.26}$$

We apply the numerical integration to Equation (6.13) and the analytical integration to Equation (6.14). Similarly, in Equation (6.12), the body 1 is the master body from the view of the body 2, thus,

$$\begin{aligned}\mathbf{f}_2^{C,i} &= \int_{\Omega_1}\int_{\Omega_2} \beta_1\beta_2 N_2^i \frac{\partial\phi\left(r\right)}{\partial r}\frac{\mathbf{x}_2-\mathbf{x}_1}{r}dv_2dv_1 \\ &= \int_{\Omega_2} \beta_2 N_2^i \tilde{\mathbf{f}}_1^C dv_2, \end{aligned} \tag{6.27}$$

where

$$\tilde{\mathbf{f}}_1^C = \int_{\Omega_1} \beta_1 \frac{\partial\phi\left(r\right)}{\partial r}\frac{\mathbf{x}_2-\mathbf{x}_1}{r}dv_1. \tag{6.28}$$

Since the integration methods of the slave and master body are different, the force comes from the body 2 to the body 1 and from the body 1 to the body 2 may not be the same, but here we neglect this difference.

In case the master body is large enough, or infinity, compared to the equilibrium distance of the Lennard-Jones potential, shown in Figure 6.8, the analytical integration of Equation (6.14) can be written as

$$\tilde{\mathbf{f}}_2^C = -\mathbf{R}\int_h^\infty \int_{-L_1}^{L_2} \beta_2 \frac{\partial \phi(r)}{\partial r}\frac{\boldsymbol{\xi}}{r} d\xi d\eta, \tag{6.29}$$

where $\mathbf{R}$ is the rotation matrix from ξ - η axis to x - y axis, and the quadrature point of the slave body is assumed to be the origin. In case that the atomic density can be assumed to

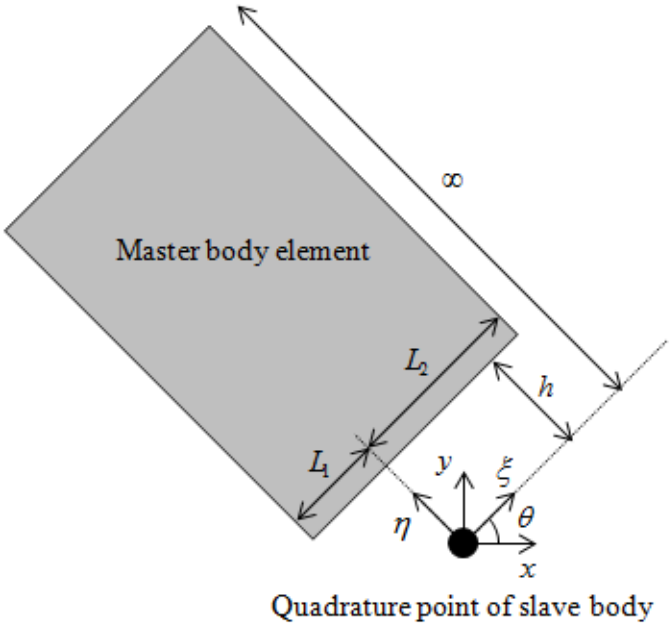

Figure 6.8: The analytical integration of the master body in two dimensions.

be constant in the master body,

$$\tilde{\mathbf{f}}_2^C = -\beta_2\mathbf{R}\left(-\int_h^\infty \int_0^{L_1} \frac{\partial \phi(r)}{\partial r}\frac{\boldsymbol{\xi}}{r} d\xi d\eta + \int_h^\infty \int_0^{L_2} \frac{\partial \phi(r)}{\partial r}\frac{\boldsymbol{\xi}}{r} d\xi d\eta\right) \tag{6.30}$$

$$= -\beta_2\mathbf{R}\left(-\hat{\mathbf{f}}^C(L_1, h) + \hat{\mathbf{f}}^C(L_2, h)\right), \tag{6.31}$$

where

$$\hat{\mathbf{f}}^C(L, h) = \int_h^\infty \int_0^{L} \frac{\partial \phi(r)}{\partial r}\frac{\boldsymbol{\xi}}{r} d\xi d\eta. \tag{6.32}$$

Similarly, Equation (6.25) is given by

$$\tilde{\mathbf{f}}_1^C = -\beta_1\mathbf{R}\left(-\hat{\mathbf{f}}^C(L_1, h) + \hat{\mathbf{f}}^C(L_2, h)\right). \tag{6.33}$$

In case the inter-solid potential is the Lennard-Jones potential,

$$\begin{aligned}\hat{f}_x^C(L,h) = \epsilon r_0^{12} \Bigg\{ & \frac{1}{11h^{11}} - \frac{63atan(L/h)}{256L^{11}} \\ & + h\frac{965L^8 + 2370h^2L^6 + 2688h^4L^4 + 1470h^6L^2 + 315h^8}{1280L^{10}\left(L^2+h^2\right)^5} \Bigg\} \\ & + 2\epsilon r_0^6 \left\{ \frac{3atan(L/h)}{8L^5} - \frac{1}{5h^5} - \frac{h\left(5L^2+3h^2\right)}{8L^4\left(L^2+h^2\right)^2} \right\}, \end{aligned} \tag{6.34}$$

and

$$\begin{aligned}\hat{f}_y^C(L,h) = \frac{\epsilon r_0^{12}}{h^{11}} \Bigg\{ & \frac{63atan(L/h)}{256} \\ & + hL\frac{315L^8 + 1470h^2L^6 + 2688h^4L^4 + 2370h^6L^2 + 965h^8}{1280\left(L^2+h^2\right)^5} \Bigg\} \\ & - \frac{\epsilon r_0^6}{4h^5} \left\{ 3atan(L/h) + hL\frac{3L^2+5h^2}{\left(L^2+h^2\right)^2} \right\}. \end{aligned} \tag{6.35}$$

This method would be applied to larger scale, since there are no penetration between slave and master bodies. In addition, this method is computationally efficient, because the integration of master body is already done.

Chapter 7

Numerical Analysis

7.1 A Validation of the Proposed FEM Surface Tension Model

In this section, the proposed FEM surface tension model is validated. A two dimensional model of a water drop is shown in Figure 7.1. The shape of the water drop is an ellipse, and

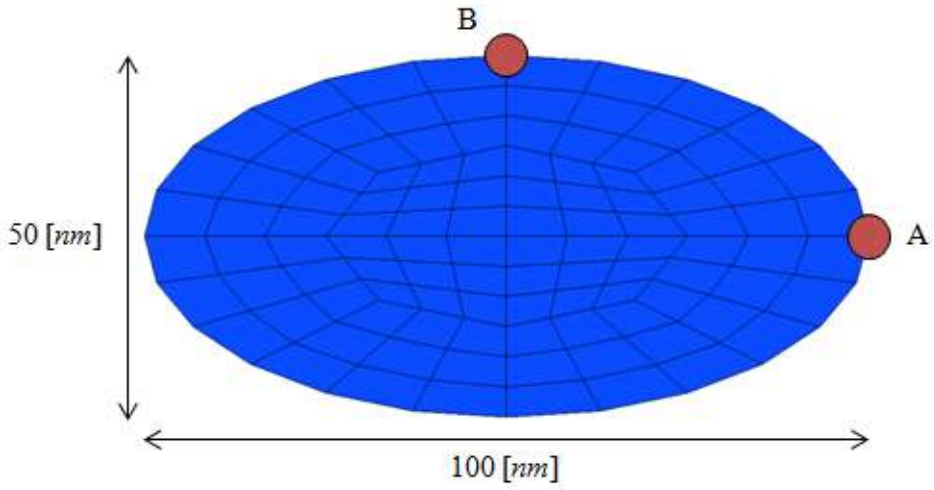

Figure 7.1: A two dimensional model for a validation of the proposed FEM surface tension model.

the radius are $100\,[nm]$ and $50\,[nm]$. The constitutive relation of the water drop is modelled by the Newtonian fluid, and the ambient space is modelled as the air. The bulk modulus and the viscosity of water are chosen as $\kappa = 2.2\,[GPa]$ and $\mu = 0.6\,[mPa \cdot s]$. The surface energy of water-air interface is $\gamma = 72.75\,[mN/m]$ (*see* [91]).

Figure 7.2 shows the time evolution of the distances between the center of the water drop and the points A, B on the surface of the water drop, as shown in Figure 7.1, by using the surface traction method and the proposed FEM surface tension method. The surface of a

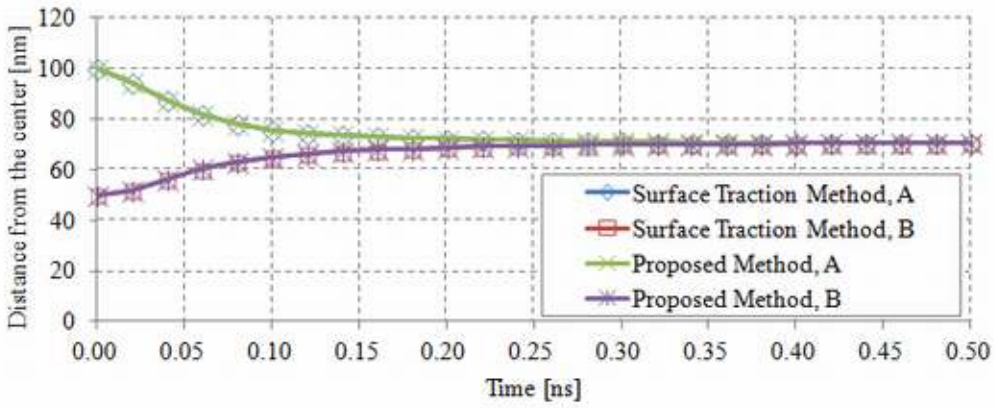

Figure 7.2: The time evolution of the distance between the points A, B and the center by the surface traction method and the proposed FEM surface tension method.

liquid drop tends to contract in order to have the smallest possible surface area, behaving as though its surface were a stretched elastic membrane. Small drops of liquid in a spray become spherical, since a sphere has the smallest surface area for a given volume [82]. Thus, the distance between point A and the center decreases, the distance between point B and the center increases, and finally these distances become the same, i.e. the body becomes a circle. Because the surface traction method and the proposed FEM surface tension method show completely the same results, the proposed method is validated here. The same validation in three dimensions is also peformed. Figure 7.3 and 7.4 show the deformation of an ellipse and an ellipsoid.

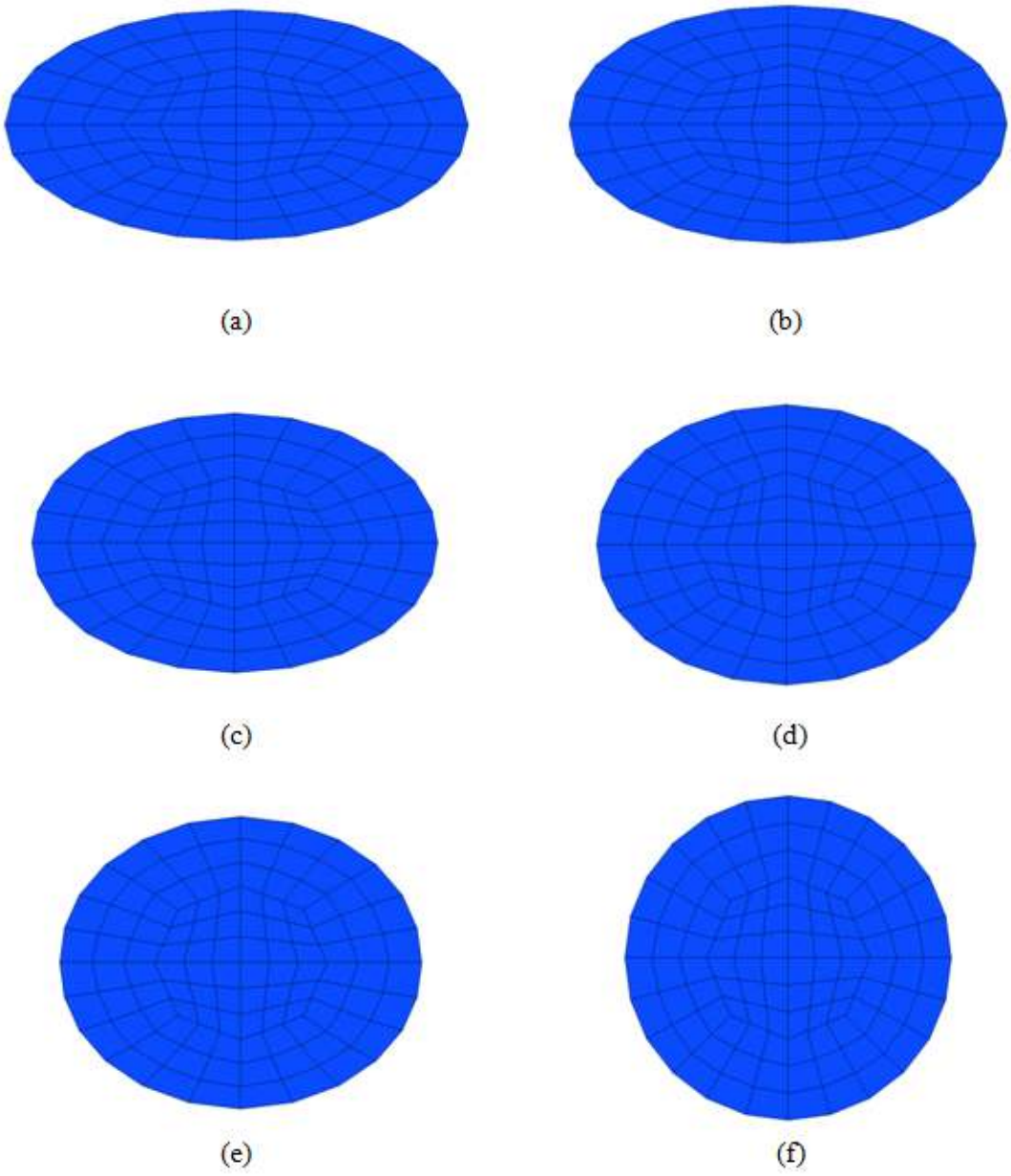

Figure 7.3: The deformation of an ellipse due to the surface tension: (a) $0\,[ns]$, (b) $20\,[ns]$, (c) $40\,[ns]$, (d) $60\,[ns]$, (e) $80\,[ns]$, (f) $500\,[ns]$.

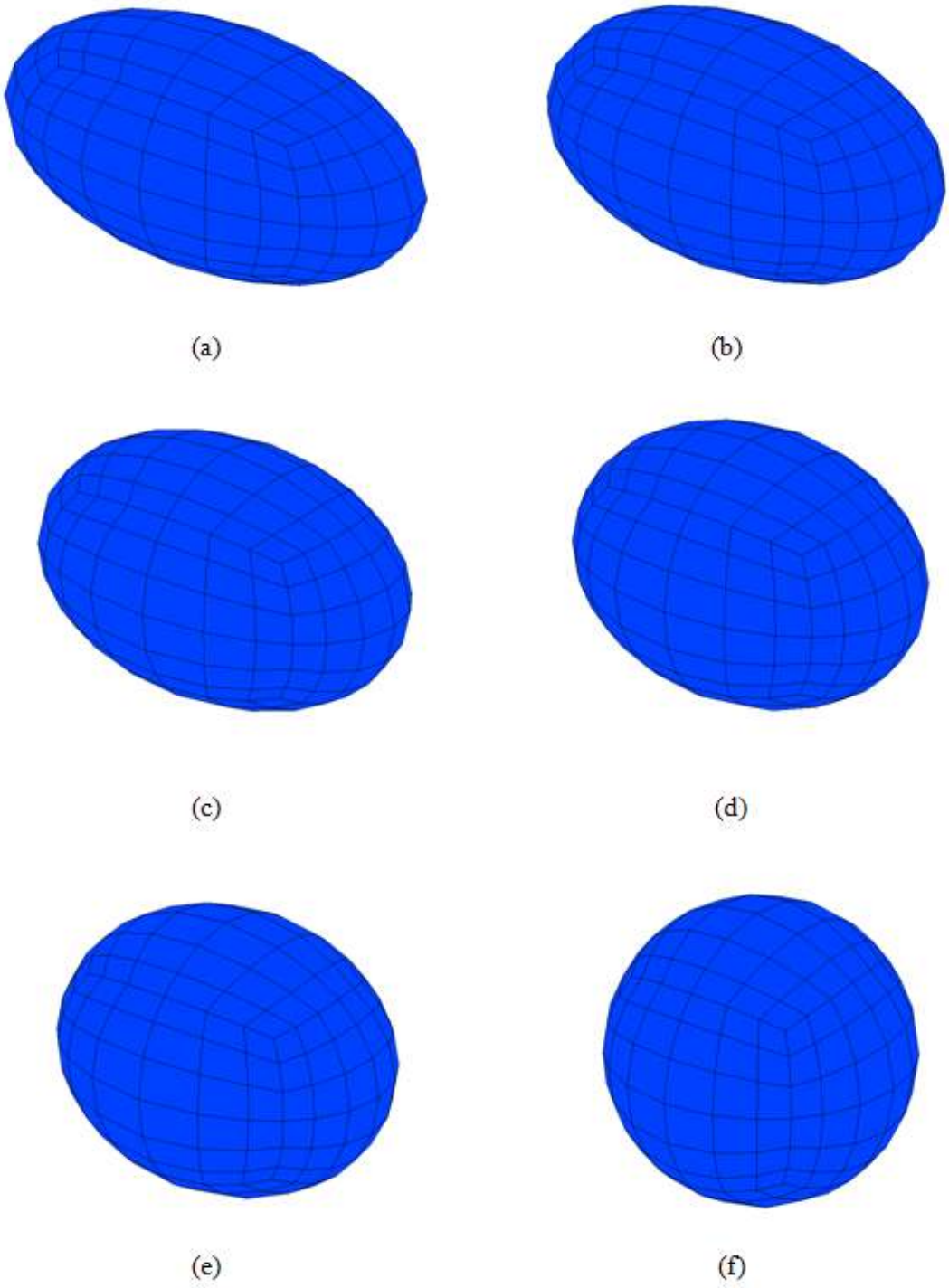

Figure 7.4: The deformation of an ellipsoid due to the surface tension: (a) $0\,[ns]$, (b) $20\,[ns]$, (c) $40\,[ns]$, (d) $60\,[ns]$, (e) $80\,[ns]$, (f) $500\,[ns]$.

7.2 A Restriction of the Coarse Grained Contact Model

It should be mentioned that the numerical integration carried out in Chapter 6 are using different quadrature rules, i.e. the Gaussian quadrature, the Newton-Cotes quadrature, or the analytical integration in the interacting body. Here, we discuss the differences of these methods and clarify the restriction of the Coarse Grained Contact Model imposed by the numerical integration.

Consider two bodies shown in Figure 7.5. Here, we use the Lennard-Jones potential

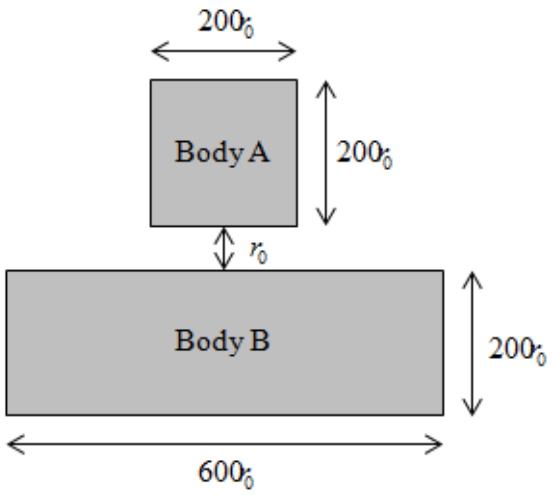

Figure 7.5: An analysis model for investigation of the Coarse Grained Contact Model.

as the interatomic potential. In Figure 7.5, r_0 is the equilibrium distance of the Lennard-Jones potential. Since the distance between two bodies is the equilibrium distance, only the attraction force, i.e. the van der Waals force, acts between two bodies.

Figure 7.6 shows the relationship between the attraction force of body A and the element size with the body-body interaction method, in which is the numerical integration is used to assess the interaction force of two bodies. In Figure 7.6, $n \times n$ means n quadrature points in both x and y directions. Note that the units of length and the energy are r_0 and ϵ, which is the depth of the potential well of the Lennard-Jones potential. The significance of the mesh size dependence is demonstrated in Figure 7.6. When the mesh size is around ten times of the equilibrium distance, the contact force cannot be computed by the body-body interaction method. To compute the contact force accurately, the element size must be less than two times of the equilibrium distance. Although increasing quadrature points reduces the restriction of the element size problem, the computational cost increases to the forth power of the number of quadrature points in two dimensions and to the ninth power of

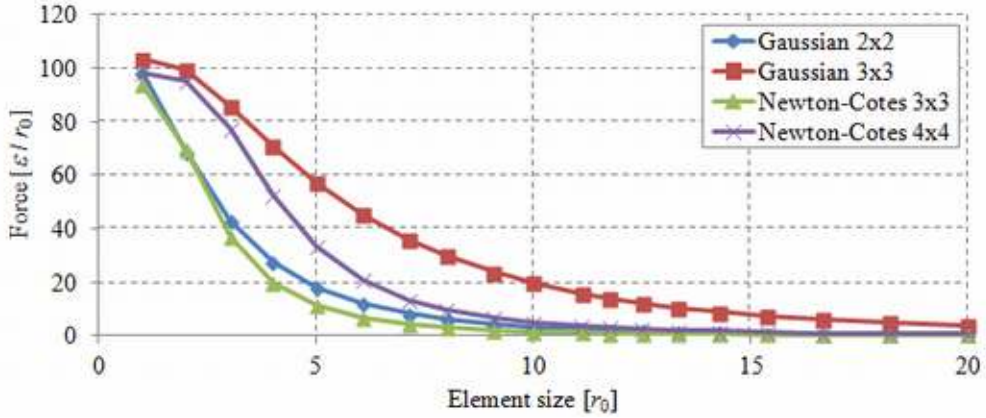

Figure 7.6: Element size dependence by the body-body interaction method.

the number of quadrature points in three dimensions in the numerical integration of two body interaction. Also, the Gaussian quadrature rule show better accuracy than that of the Newton-Cotes quadrature rule, even though the Newton-Cotes quadrature rule have quadrature points on the surface. Higher order quadrature integration may be considered, because the Lennard-Jones potential is the high order polynomial equation.

We show Figure 7.7 that shows the contact force calculated by using different depth of body B in Figure 7.5, i.e. we changed the depth from $200r_0$ to $1 \sim 10r_0$, in order to investigate the possibility to apply the body-surface interaction method that integrates the master body analytically but the slave body numerically. In this case, accodring to Figure

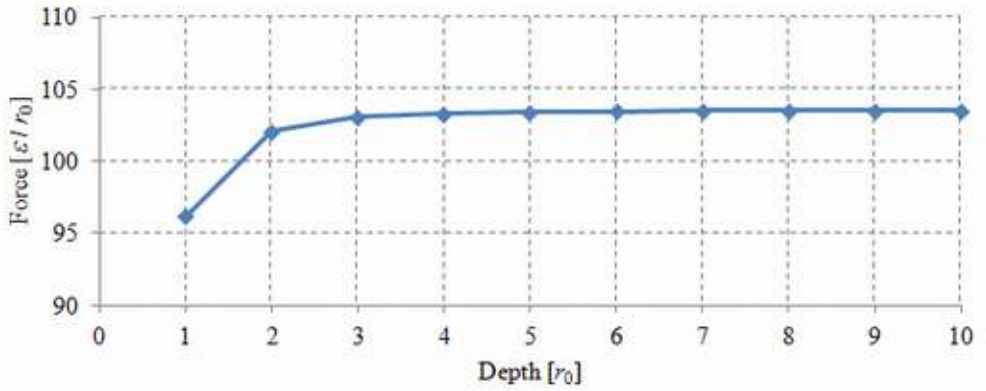

Figure 7.7: Contact force at different depth of body B.

7.7, the contact force is almost saturated at $3r_0$. Hence, the body-surface interaction method can be applied when the depth of body B is larger than about $3r_0$. Because the depth of

body B of the analysis model is large enough compared to $3r_0$, the body-surface interaction method can be applied.

Figure 7.8 shows the comparison between the body-body and body-surface interaction method for the Gaussian quadrature rule (3×3). Although the body-surface interaction

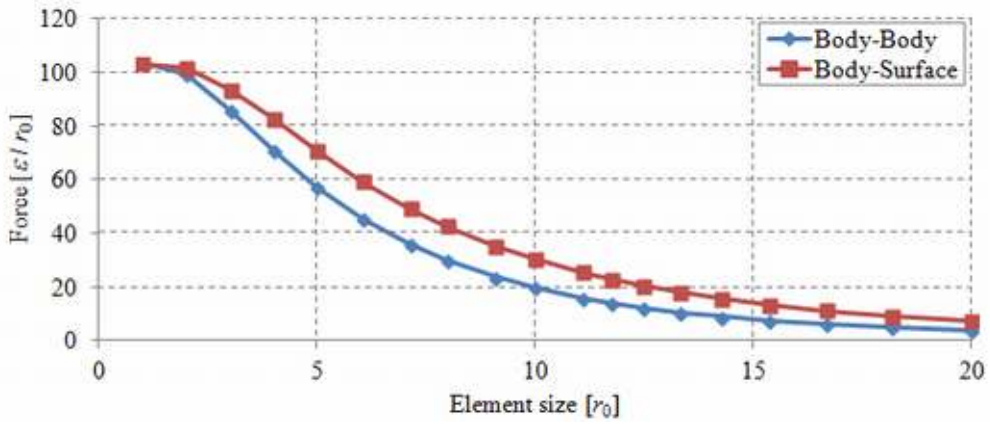

Figure 7.8: The comparison between the body-body and body-surface interaction method for the Gaussian quadrature rule (3×3).

method shows better accuracy than that of the body-body interaction method, the restriction of the mesh size is still significant. However, the calculation of the body-surface interaction method is much more efficient than that of the body-body interaction method, this is because the body-surface interaction method needs only one body integration. Hence, the number of quadrature points can be increased in the body-surface integration method without significantly increse of computational cost.

Figure 7.9 shows the comparison of quadrature points in the body-surface interaction method, and Table 7.1 shows the required mesh size in order to have the contact force error within 5%, where the result of quadrature points 8×8 and the element size r_0 is used as reference. In Table 7.1, the efficiency is defined as the element size per the number of quadrature points in one direction, and a higher value means more efficient. According to Table 7.1, increasing quadrature points is more efficient than decreasing element size.

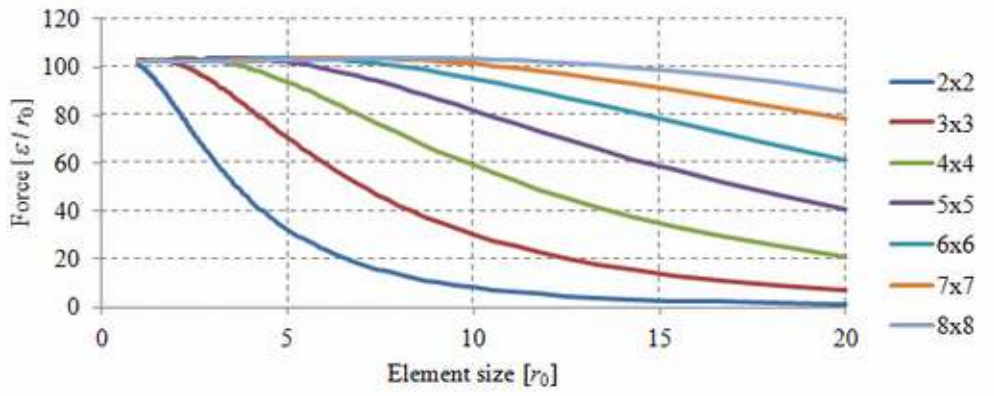

Figure 7.9: Comparison of quadrature points in the body-surface interaction method.

Number of quadrature points	Element size [r_0]	Efficiency
2×2	1.29	0.65
3×3	2.63	0.88
4×4	4.35	1.09
5×5	6.67	1.33
6×6	9.09	1.52
7×7	11.8	1.69
8×8	15.4	1.93

Table 7.1: Required element size to compute the contact force error within 5%.

7.3 Nanoindentation Analysis

In this section, we present an example of simulation of nanoindentation between a spherical rigid indenter and a flat substrate, which is usually performed to qualify the dislocation in single crystal copper. In this simulation, we employ the Cauchy-Born rule and the Coarse Grained Contact Model. This had been studied in the numerical simulations by using both Molecular Dynamics and the multiscale Finite Element Method, e.g. [100], [103].

The EAM potential developed by Mishin et al. [45], [57], [58] is used in combination with the Cauchy-Born rule (see Appendix D) to model the substrate of the nanoindentation. The nanoindentation test is carried out on a $20\,[nm] \times 10\,[nm]$ plane strain substrate, whose x and y axis are along $[1\ 1\ \bar{2}]$ and $[1\ 1\ 1]$ direction. The radius of the frictionless rigid indenter is $5\,[nm]$, shown in Figure 7.10. The contact between the indenter and substrate is modelled by the Coarse Grained Contact Model.

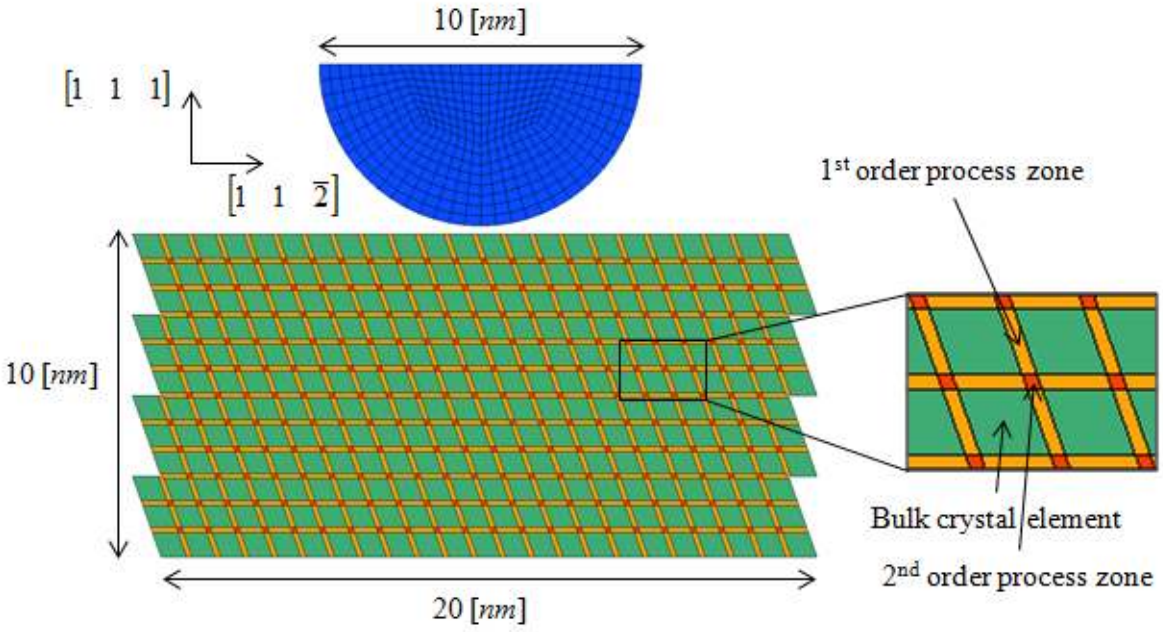

Figure 7.10: A nanoindentation analysis model.

We introduce the first and second order process zone as shown in Figure 7.10, as a finite thickness interphase zone, in which the deformation, stress and strain fields are non-linear. Material failure is no longer defined solely as cleavage surface or interface separation, but it is due to a general atomistic debonding and lattice defect evolution in a finite volume. In a single crystal, the bulk crystal element is modelled by the first order Cauchy-Born rule, and the process zone elements are modelled by the higher order Cauchy-Born rule, i.e. the

first and second order process zone are modelled by the second and third order Cauchy-Born rules respectively. This will induce specific length scale in the specific process zone according to the specific order of the strain gradients. The higher order element should be applied to compute the higher order derivatives of shape functions. However, we don't want to add nodes on the edge of the process zone elements, because the bulk crystal element should be a linear element. Hence, we applied the enriched element [37], shown in Figure 7.11, which adds a node at the center of the element. Shape functions at each node are given by

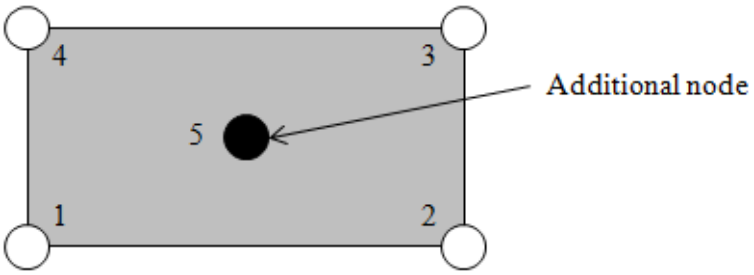

Figure 7.11: The enriched element [37] for the process zone elements.

$$N_1(\xi,\eta) = \frac{1}{4}(1-\xi)(1-\eta) - \frac{1}{4}\left(1-\xi^2\right)\left(1-\eta^2\right), \tag{7.1}$$

$$N_2(\xi,\eta) = \frac{1}{4}(1+\xi)(1-\eta) - \frac{1}{4}\left(1-\xi^2\right)\left(1-\eta^2\right), \tag{7.2}$$

$$N_3(\xi,\eta) = \frac{1}{4}(1+\xi)(1+\eta) - \frac{1}{4}\left(1-\xi^2\right)\left(1-\eta^2\right), \tag{7.3}$$

$$N_4(\xi,\eta) = \frac{1}{4}(1-\xi)(1+\eta) - \frac{1}{4}\left(1-\xi^2\right)\left(1-\eta^2\right), \tag{7.4}$$

$$N_5(\xi,\eta) = \left(1-\xi^2\right)\left(1-\eta^2\right). \tag{7.5}$$

This enriched element obviously satisfies the partition of unity $\sum_I^5 N_I = 1$.

Figure 7.12 shows load-deflection curve during indentation. Before dislocation, the material response is predicted by Molecular Dynamics [103], the interatomic potential Finite Element Method [103] and the proposed method are in good agreements. The Molecular Dynamics simulation shows that the load drops sharply at the indentation depth between $u = 6$ and 7, but the interatomic potential Finite Element Method cannot captured it. On the other hand, the proposed method can accurately predict dislocation nucleation induced elastic instability just like the Molecular Dynamics simulation. Also, the proposed method can capture the surface roughness of the substrate during the indentation, which is the manifestation of surface displacement burst caused by dislocation nucleation, and it is a distinct feature of nanoscale indentation. The deformation and surface roughness are shown in Figure 7.13.

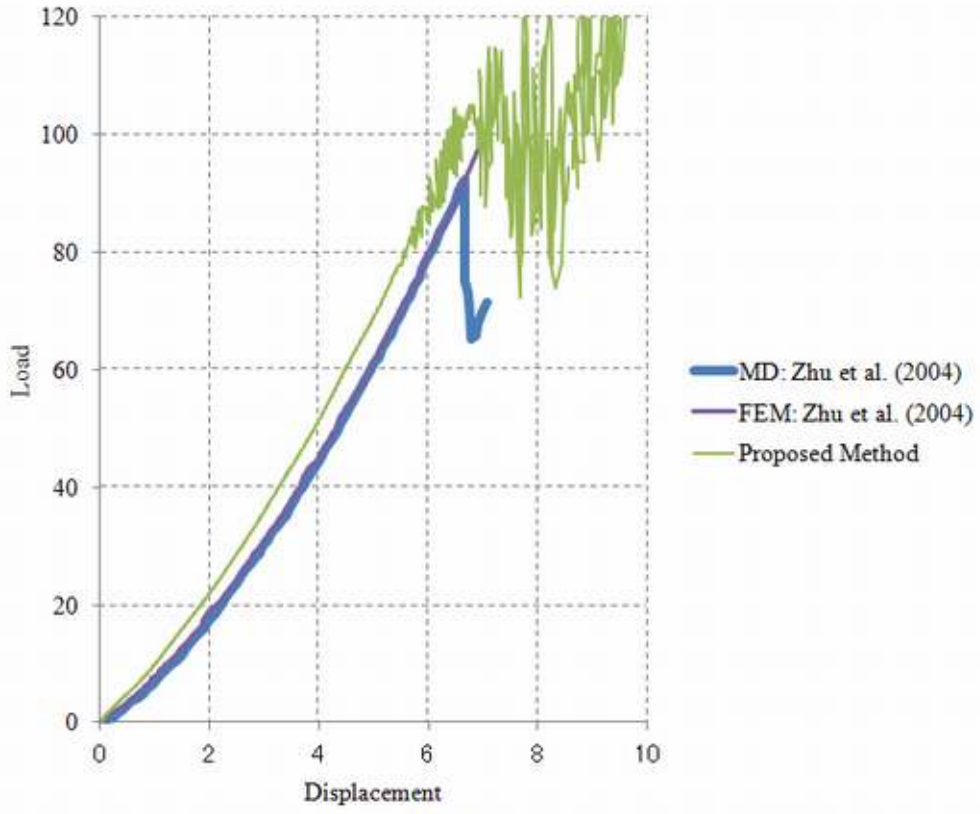

Figure 7.12: Load-deflection curve during indentation.

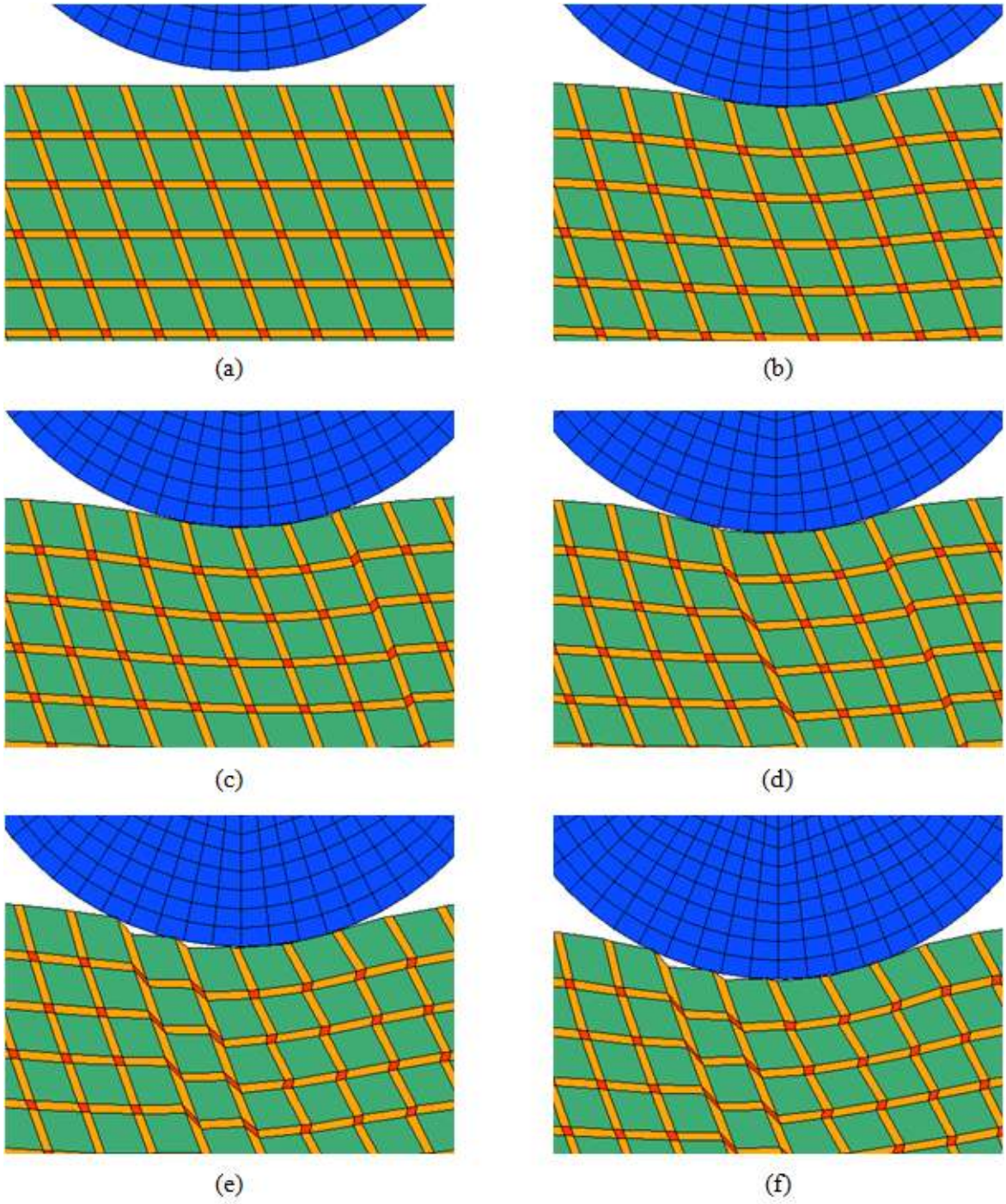

Figure 7.13: The deformation and surface roughness of the nanoindentation analysis: (a) $0\,[ns]$, (b) $0.03\,[ns]$, (c) $0.035\,[ns]$, (d) $0.04\,[ns]$, (e) $0.045\,[ns]$, (f) $0.05\,[ns]$.

7.4 Capillary Rise Analysis

In this section, the simulation of the capillary rise is performed. The analytical solution of the capillary rise in a tube is known as the Lucas-Washburn equation [53], [96],

$$h\left(t\right)=\sqrt{\frac{R\gamma\cos\theta}{2\mu}t}, \tag{7.6}$$

where $h\left(t\right)$ is the equilibrium hight, R is the radius of a tube, γ is the surface tension between the liquid and gas, θ is the contact angle, μ is the dynamic viscosity of the liquid, and t is the time. The equilibrium height is a function of time and proportional to the square root of time. In this section, two dimensional analysis is performed, and the analytical solution of the capillary rise between parallel walls is given by following equation, see Appendix E,

$$h\left(t\right)=\sqrt{\frac{2R\gamma\cos\theta}{3\mu}t}. \tag{7.7}$$

The equilibrium height is also proportional to the square root of time, and only the factor of proportionality is different from Equation (7.6). The symmetric model is used, because

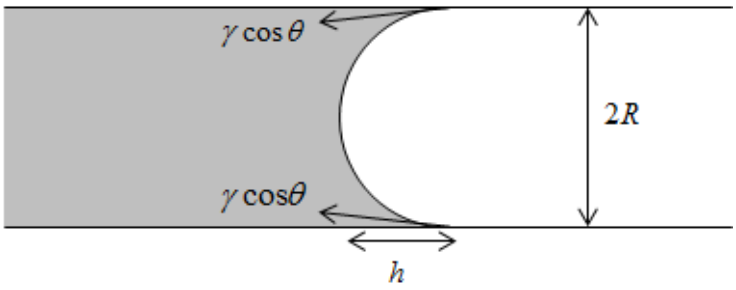

Figure 7.14: Illustration of the capillary rise between two walls.

the inflow condition or the construction of the water reservoir is difficult for the Lagrangian Finite Element Method. A FEM model is shown in Figure 7.15. The distance between two

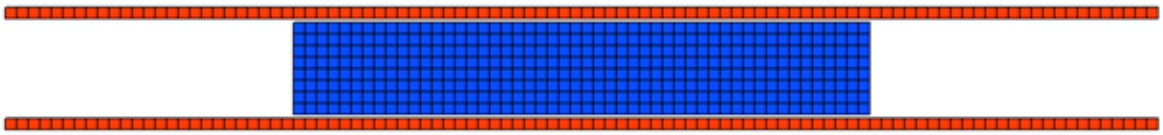

Figure 7.15: A FEM model of the capillary rise between two walls.

walls is $2R = 8\,[nm]$, the surface energy between the liquid and gas is $\gamma = 72.75\,[mN/m]$, the contact angle is $\theta = 50°$, the dynamic viscosity is $\mu = 1\,[mPa \cdot s]$, and the solid is rigid body. The body-surface interaction method of the Coarse Grained Contact Model is applied to the interaction between the liquid and solid.

When the Coarse Grained Contact Model is used in simulation, there is a gap between two contacting bodies. To check whether or not a node of liquid surface node is in contact with the solid surface, the following contact detection algorithm is applied in the computation: In case of two dimensional simulations, the solid surface equation may be represented as a linear equation $ax + by + c = 0$, where a, b and c are the coefficients, and the position of the liquid node is $\mathbf{x}_0 = (x_0, y_0)$, then, the distance between the liquid node and the solid surface D is given by

$$D = \frac{|ax_0 + by_0 + c|}{\sqrt{a^2 + b^2}}. \tag{7.8}$$

If $D < \epsilon$, where ϵ is the contact tolerance, the liquid node is in contact with the solid surface. In case of three dimensional simulations, the solid surface equation is $ax + by + cz + d = 0$, where a, b, c and d are the coefficients, and the position of the liquid node is $\mathbf{x}_0 = (x_0, y_0, z_0)$, then, the distance between the liquid node and the solid surface D is given by

$$D = \frac{|ax_0 + by_0 + cz_0 + d|}{\sqrt{a^2 + b^2 + c^2}}. \tag{7.9}$$

If $D < \epsilon$, the liquid node is in contact with the solid surface.

The comparison between the analytical solution and the numerical solution of the equilibrium height is shown in Figure 7.16. In Figure 7.16, Method 1 and 2 denote the proposed

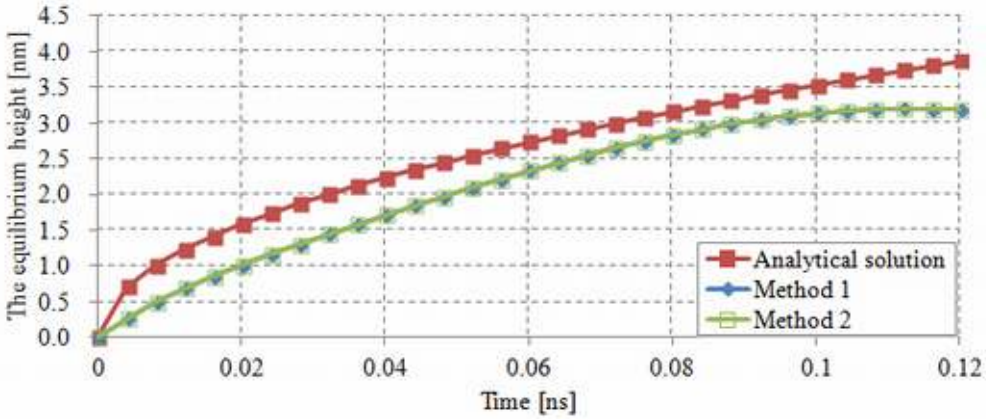

Figure 7.16: The analytical solution and the numerical solution of the equilibrium height.

dynamic wetting models based on the proposed FEM surface tension model and the FEM weak formulation of dynamic wetting. Both method 1 and 2 give the same results, but they

are different from the analytical solution at the begining of the simulation. The analytical solution, Equation (7.7), assumes the constant contact angle during the simulation, and this is the reason why the equilibrium height of the analytical solution sharply rises at the begining of the simulation. On the other hand, the contact angle is dynamically changed in the proposed dynamic wetting model. Hence, the analytical solution and the proposed method are different at the begining of the simulation. In addition, the equilibrium height of the analytical solution keeps increasing, because Equation (7.7) is simply a proportional expression, but the equilibrium height of the proposed method is saturated after $0.1\,[ns]$.

Figure 7.17 shows the relationship between the equilibrium height and the square root of time. The factor of proportionality of the analytical solution is $11.167\,[nm/\sqrt{ns}]$, and

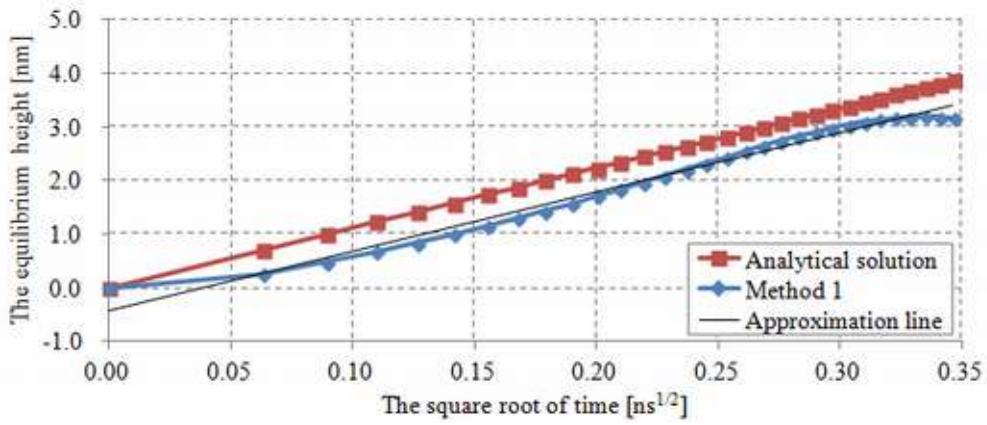

Figure 7.17: The relationship between the equilibrium height and the square root of time.

the slope of the approximation line of the numerical simulation result is $11.035\,[nm/\sqrt{ns}]$. Hence, the analytical solution and the proposed method are in good agreement at the middle of the simulation. The deformation at $0.1\,[ns]$ is shown in Figure 7.18.

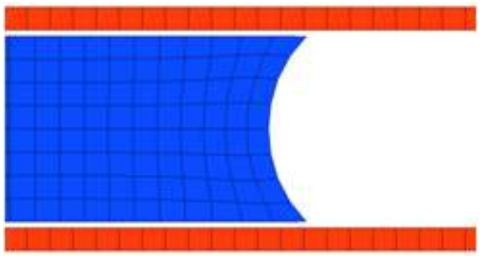

Figure 7.18: The deformation of the capillary rise at $0.1\,[ns]$.

7.5 Droplet Spreading Analysis

In this section, the simulation of droplet spreading is performed. A two dimensional simulation model is shown in Figure 7.19. The liquid is water, and it is modelled as the

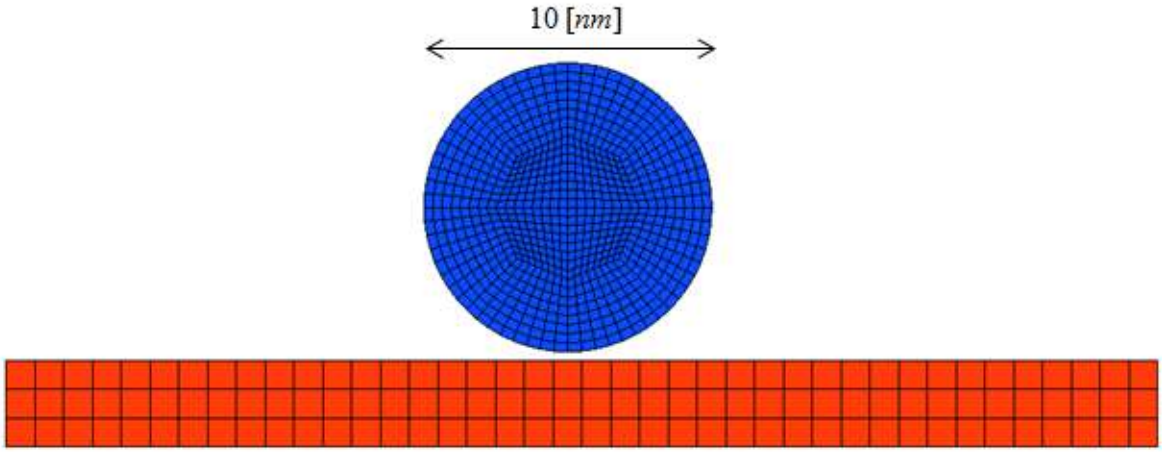

Figure 7.19: A simulation model of droplet spreading in two dimensions.

Newtonian fluid, the solid is copper, and it is modelled by the Embedded Atom Method, i.e. the EAM-Holian potential [38], [39], [94], in combination with the Cauchy-Born rule. The gas phase is taken as the air. The bulk modulus and the viscosity of water are $\kappa = 2.2\,[GPa]$ and $\mu = 0.6\,[mPa \cdot s]$. The material parameters of the EAM-Holian/Cauchy-Born rule are shown in Appendix D. The surface energy between the water and air is $\gamma^{LG} = 72.75\,[mN/m]$ [91], the surface energy between the copper and air is $\gamma^{SG} = 1780\,[mN/m]$ [88]. The surface energy between the water and copper is derived from the Young equation and the experimental contact angle which is about 40° [46],

$$\gamma^{LS} = 1780 - 72.75\cos 40 = 1724\,[mN/m]\,. \tag{7.10}$$

In this analysis, we applied Method 2, i.e. the proposed dynamic wetting Finite Element Method to solve the problem, however the solution appears to be independent from the surface strain, this agrees with the results in Section 7.4, in which we have showed that the results obtained via Method 1, which is based on the FEM surface tension model, and Method 2 are the same.

The parameters of the Lennard-Jones potential for the Coarse Grained Contact Model can be computed from the arithmetic and geometric mean,

$$\epsilon^{cw} = \sqrt{\epsilon^c \epsilon^w}, \tag{7.11}$$

and

$$r_0^{cw} = \frac{1}{2}\left(r_0^c + r_0^w\right). \tag{7.12}$$

The parameters of the Lennard-Jones potential for water are obtained from [6], $\epsilon^w = 0.0067\,[eV]$ and $r_0^w = 0.355\,[nm]$. The parameters of the Lennard-Jones potential for copper are $\epsilon^c = 0.073\,[eV]$ and $r_0^c = 0.260\,[nm]$. Hence, from these equation, $\epsilon^{cw} = 0.022\,[eV]$ and $r_0^{cw} = 0.3075\,[nm]$.

The history of the dynamic contact angle is shown in Figure 7.20. In this figure, the experimental contact angle shows the equilibrium contact angle. FEM results have many

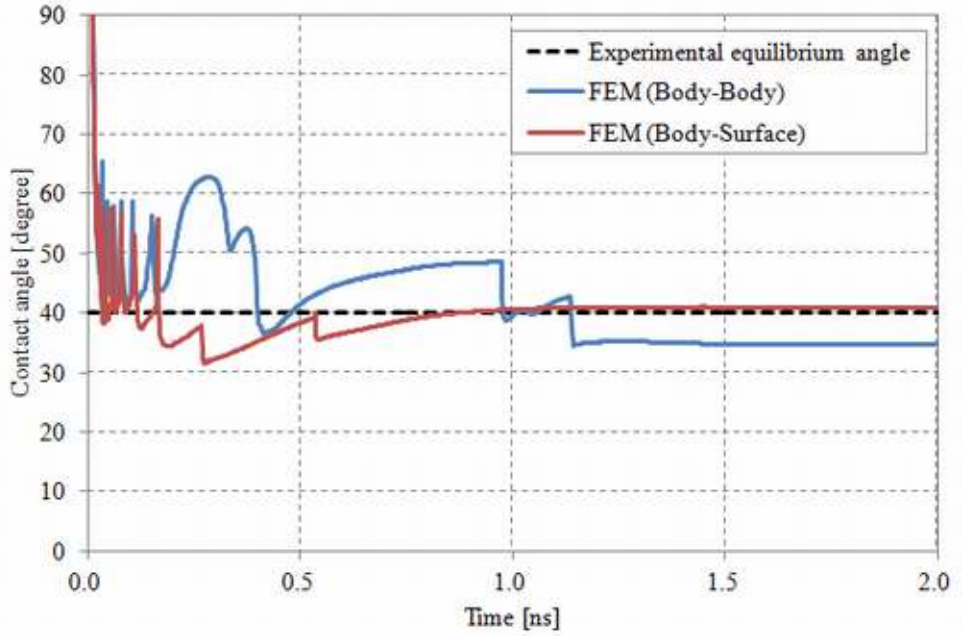

Figure 7.20: The history of the dynamic contact angle.

jumps, this is because the liquid elements makes contact with the solid surface one by one at time along the contact line at spreading front, which cause numerical fluctuation. The body-surface interaction method converges to 41°, which is almost the same as the experimental contact angle. On the other hand, the body-body interaction method converges to 35°. Figure 7.21 shows the contact force in the parallel direction of the solid surface at the contact line. Since copper is very stiff in comparison to water, the deformation of the copper substrate is almost negligible. In addition, since the solid surface is large enough, the contact force in the horizontal direction must be zero. Indeed, the body-surface interaction method shows zero horizontal force, but the body-body interaction method shows large horizontal force compared to the surface energy. Due to the existance of this unbalance force, the contact angle of the body-body interaction method converges to the different angle from the experiment. The spreading sequence of the water drop are shown in Figure 7.22.

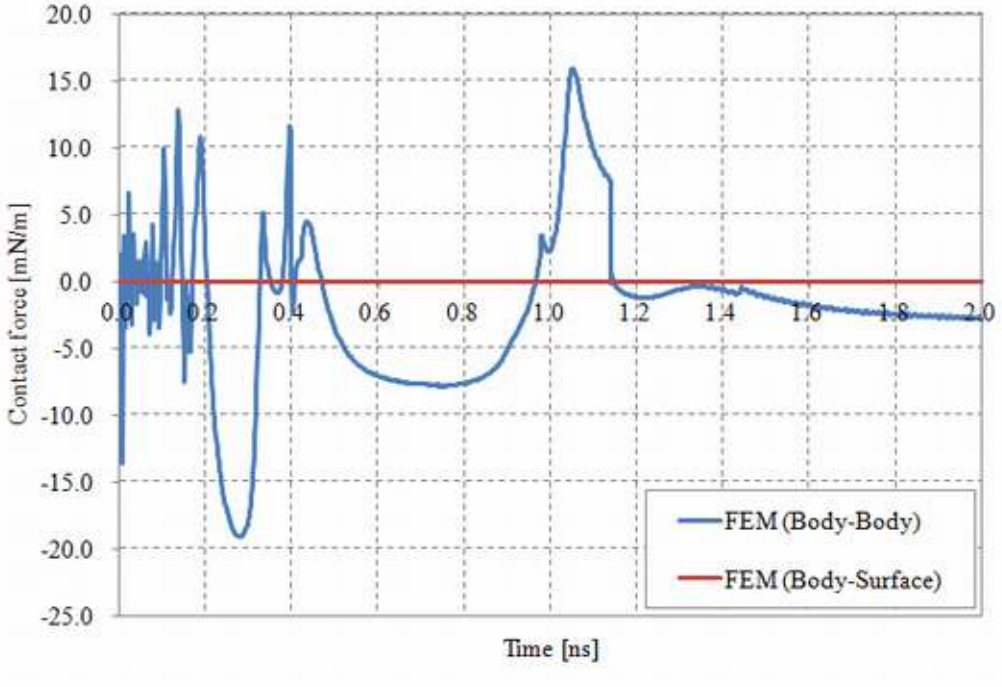

Figure 7.21: The contact force in the parallel direction of the solid surface at the contact line

In addition to the two dimensional analysis, three dimensional analysis is also performed. The simulation conditions of the three dimensional analysis are the same as the two dimensional analysis. The spreading sequence of the water drop in three dimensions are shown in Figure 7.23.

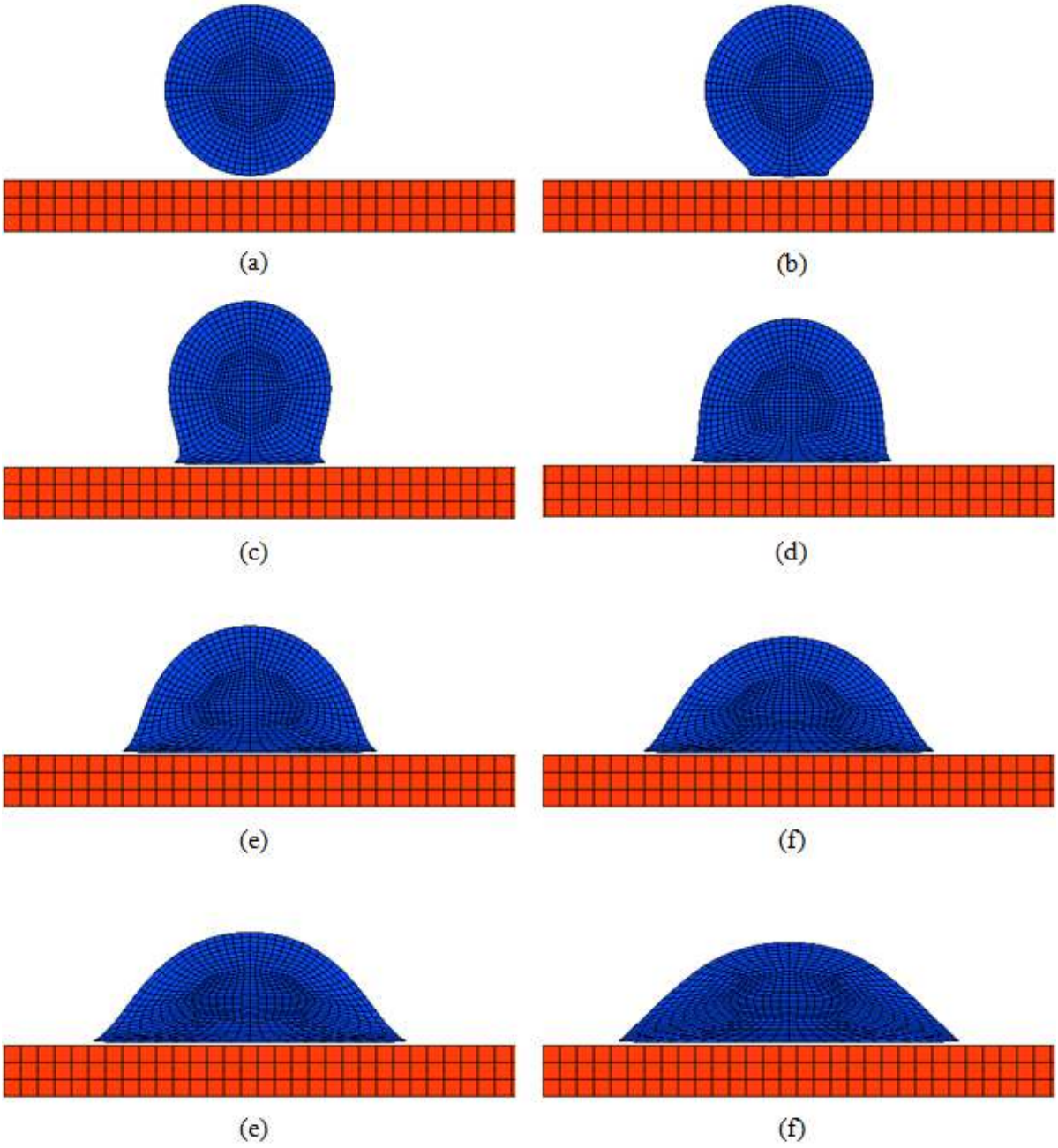

Figure 7.22: The deformation: (a) 0 $[ns]$, (b) 0.01 $[ns]$, (c) 0.03 $[ns]$, (d) 0.06 $[ns]$, (e) 0.10 $[ns]$, (f) 0.15 $[ns]$, (g) 0.20 $[ns]$, (h) 1.00 $[ns]$.

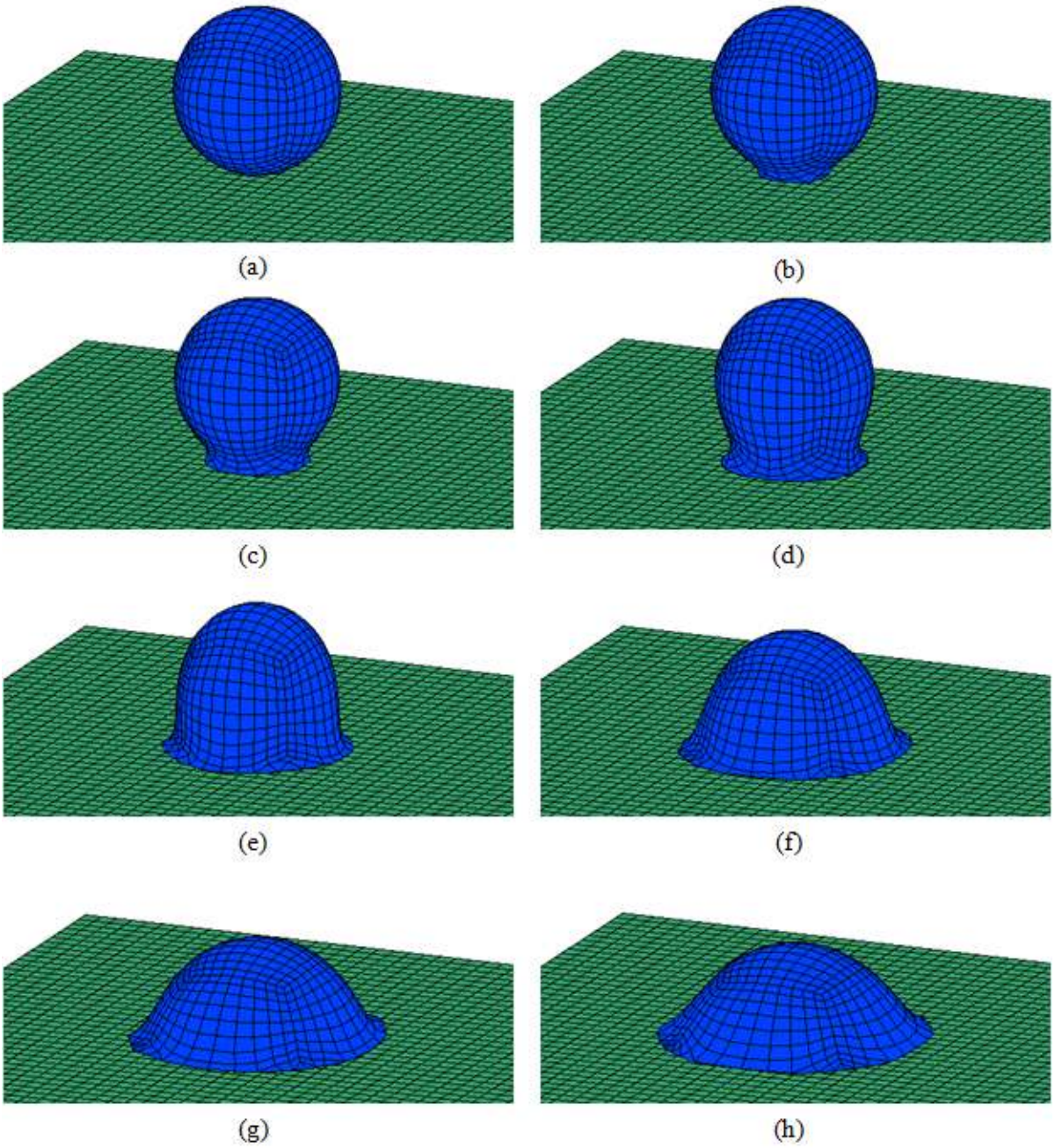

Figure 7.23: The deformation: (a) $0\,[ns]$, (b) $0.005\,[ns]$, (c) $0.01\,[ns]$, (d) $0.02\,[ns]$, (e) $0.04\,[ns]$, (f) $0.06\,[ns]$, (g) $0.08\,[ns]$, (h) $0.10\,[ns]$.

Secondly, the proposed method is compared with Molecular Dynamics which Blake et al. [7] [8] [19] simulated spreading of liquid droplets. The simulation model is the same as Figure 7.19. The liquid is assumed to be hexadecane, and the parameters of the Lennard-Jones potential between the liquid and solid are $\epsilon^{ls} = 0.0259\,[eV]$ and $r_0^{ls} = 0.39\,[nm]$. The viscosity of the liquid is $\mu = 5.82\,[mPa \cdot s]$, and the surface energy between the liquid and gas is $27.5\,[mN/m]$. Since the solid is not specified in [19], we assumed to be copper, $\gamma^{SG} = 1780\,[mN/m]$ [88]. In the case that the equilibrium contact angle is 120°, the surface energy between the liquid and gas is $\gamma^{LS} = 1794.25\,[mN/m]$ which is obtained from the Young equation. Similarly, in the case that the equilibrium contact angle are 90° and 50°, the surface energy between the liquid and gas are $\gamma^{LS} = 1780\,[mN/m]$ and $\gamma^{LS} = 1761.68\,[mN/m]$ respectively. In this simulation, the contact angle is defined as the average angle of three elements along the contact line, shown in Figure 7.24. The dynamic contact angle history

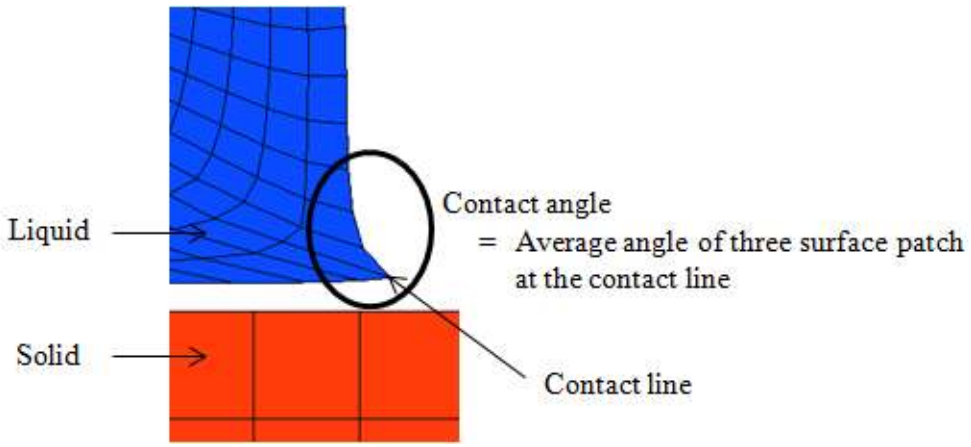

Figure 7.24: The contact angle is defined as the average angle of three elements along the contact line.

simulated by using the proposed method is displayed in Figure 7.25. Although the results obtained via the proposed method have several jumps due to the discrete nature of the Lagrangian Finite Element Method, the dynamic contact angle of the proposed method are in good agreement with the results obtained by using Molecular Dynamics.

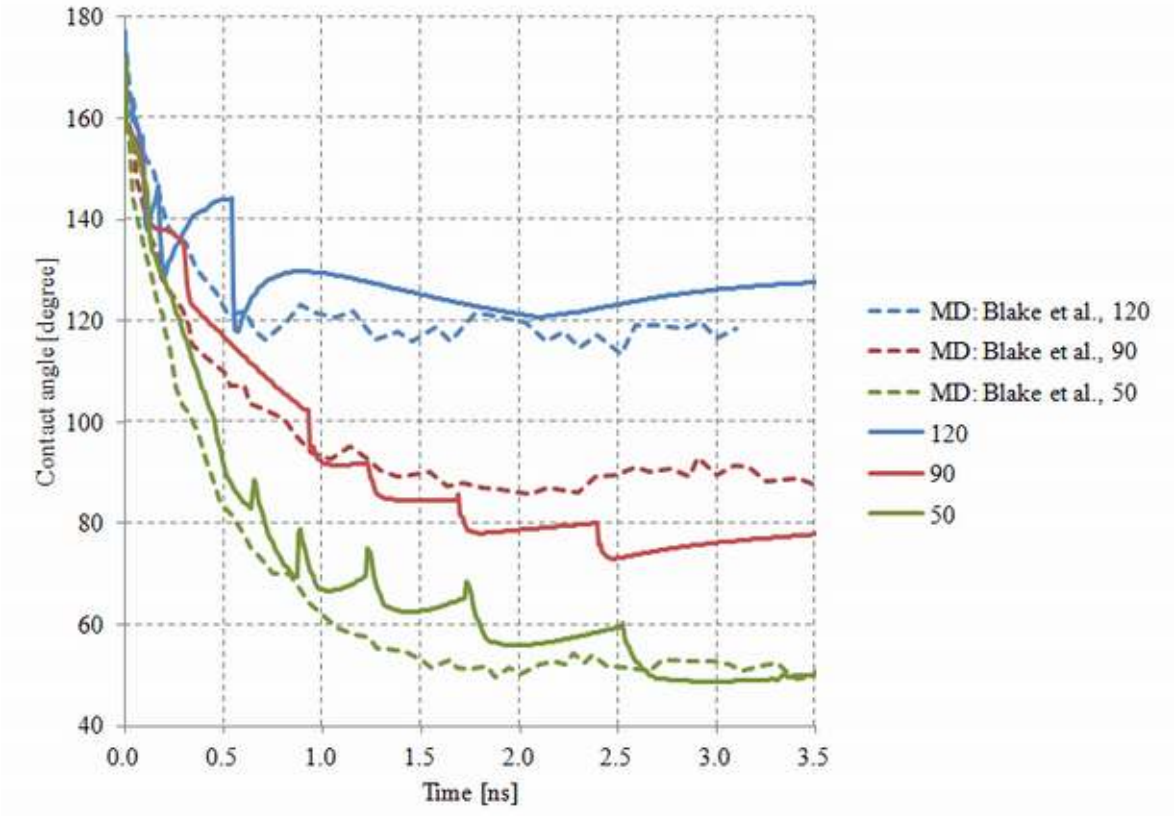

Figure 7.25: The dynamic contact angle history.

7.6 Comparison of the Surface Stresses

In this section, the surface stresses are calculated by using both the Gurtin-Murdoch surface elasticity model and the Surface Cauchy-Born rule. The crystallographic orientation of the substrate crystal lattice is shown in Figure 7.26.

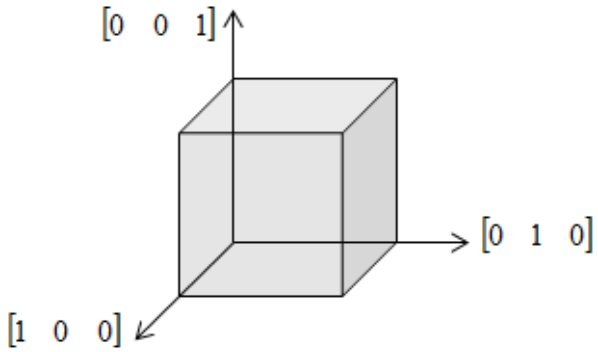

Figure 7.26: The crystallographic orientation of the substrate crystal lattice.

Table 7.2 shows the surface energy of copper by using several constitutive models. Since experimental measurements of the surface energy for the solid interface is difficult to perform, Tyson et al. [88] provide the estimation of the surface energy based on the surface energy of liquids. In this dissertation, material parameters used in the Gurtin-Murdoch model are obtained from [11], which are calculated by using Molecular Dynamics. Material parameters of atomic potentials are in Appendix D. The surface energy obtained by using the Lennard-

	Surface energy $[mN/m]$
Estimation [91]	1780
The Gurtin-Murdoch [11]	1507
The surface Cauchy-Born Lennard-Jones	-50
The surface Cauchy-Born EAM-Mishin	2308
The surface Cauchy-Born EAM-Wadley	2470
The surface Cauchy-Born EAM-Holian	1909

Table 7.2: The surface energy of copper.

Jones potential with the surface Cauchy-Born rule is -50, and it is completely different from the estimation of the surface energy. On the other hand, the surface energy obtained by using the Embedded Atom Method, especially the EAM-Holian, are close to the estimation. Hence, we must apply the EAM potential to simulate FCC metals' surface energy in addition to the elasticity tensor simulation.

Figure 7.27 shows the relationship between the surface strain and surface energy, in which one may find the surface strain change with the increasing of the surface energy. The results

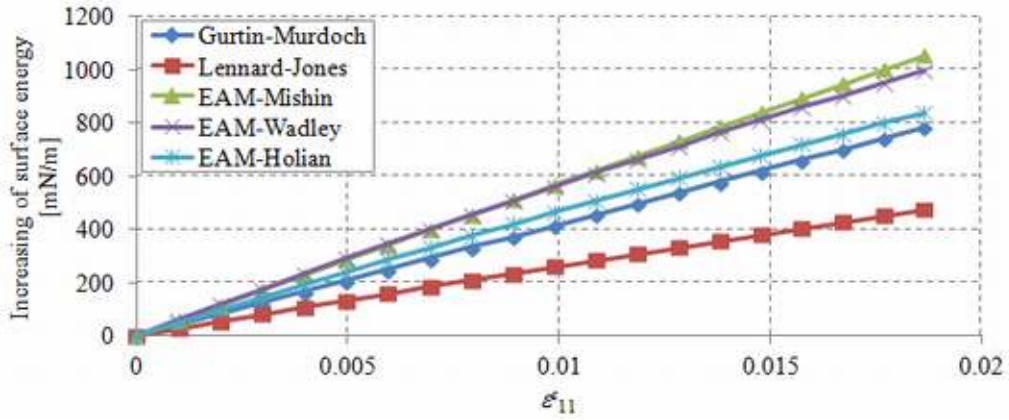

Figure 7.27: The relationship between the surface strain and the increasing of the surface energy.

obtained by using the surface Cauchy-Born rule are almost linear relations, and the slopes of the surface strain/surface energy relation obtained by the surface Cauchy-Born rule are close to that of the Gurtin-Murdoch elasticty model, especially when the EAM-Holian potential is used. According to these results, the EAM-Holian potential is good to describe the surface energy and stress. Table 7.3 shows the surface energy of several FCC metals. Material parameters are shown in Appendix D. Although the EAM-Holian overestimates the surface

	Estimation [91] $[mN/m]$	EAM-Holian $[mN/m]$
Ag	1240	1556
Al	1140	1214
Au	1500	2393
Ni	2370	2637

Table 7.3: The surface energy of FCC metals.

energy, the rank order of the surface energy are the same as the estimation. Although we showed the possibility of fully numerical simulation by applying the surface Cauchy-Born rule, both the surface Cauchy-Born rule and the Gurtin-Murdoch surface elasticity model cannot be applied in the proposed dynamic wetting model based on the Galerkin weak formulation, because the surface Cauchy-Born rule cannot be applied to compute the surface stress between the liquid and solid.

Chapter 8

Conclusions

In this work we have presented, derived and studied a large deformation, computational, multiscale dynamic wetting and droplet spreading. The Finite Element Method based surface tension models is introduced, and two different implementations of the dynamic wetting model are proposed, the dynamic wetting model based on the proposed FEM surface tension model and the Galerkin weak formulation of dynamic wetting.

As outlined in Section 2, the FEM surface tension model is developed based on the definition of the surface tension in the macroscopic, which the surface tension is the force along a line of unit length, where the force is parallel to the surface but perpendicular to the line. The proposed method is more computationally efficient than the surface traction method that the surface traction, which is equivalent to the surface tension, is applied to surfaces.

In Chapter 3, the wetting and droplet spreading problems on the rigid substrate based on the proposed FEM surface tension model are formulated. This result in equilibrium state is consistent with the Young equation. The implementations of the Finite Element Method in both two and three dimensions are also discussed.

In Chapter 4, a Galerkin weak formulation of the surface tension model based on the surface stress and surface deformation is presented. Because the above method considers only the surface energy, it can be applied to only the rigid substrate. To simulate various deformable substrate, a Galerkin weak formulation that takes into account the surface stress is constructed. For the Finite Element Method, the virtual solid surface is introduced in order to solve the dilemma which the positions of the liquid and solid nodes are generally different, because we don't prescribe non-slip boundary condition between the liquid and solid. The solid-gas interface element is introduced to take into account the surface stress between the solid and gas.

In Chapter 5, several constitutive models are illustrated. The Cauchy-Born rule, which relates the stress state of a uniformly deformed crystalline solid to the change of lattice vectors, is discussed, and formulated for the pair potential and Embedded Atom Method. As the mesoscale constitutive models of the surface stress, the Gurtin-Murdoch surface elasticity model and the Surface Cauchy-Born rule are discussed.

In Chapter 6, the Coarse Grained Contact Model as the contact method is introduced between the liquid and solid, and the efficient and high accuracy method which is the analytical integration method of the master body is investigated.

In Chapter 7, the proposed FEM surface tension model is validated by a water droplet problem, and the restrictions of the Coarse Grained Contact Model is investigated carefully. An example of simulation of nanoindentation between a spherical rigid indenter and a flat substrate is presented, and the proposed method can accurately predict dislocation nucleation induced elastic instability just like the Molecular Dynamics simulation. In addition, the proposed method can capture the surface roughness of the substrate during the indentation, which is the manifestation of surface displacement burst caused by dislocation nucleation, and it is a distinct feature of nanoscale indentation. The proposed dynamic wetting Finite Element Method model is validated by numerical analysis compared with the experiment, Molecular Dynamics and theoretical solution. Although the time history of dynamic contact angle by using the proposed model have oscillation due to the Lagrangian method but are in good agreement with that of Molecular Dynamics, and the equilibrium contact angle compare well with that of the experiment.

Bibliography

[1] Allen, M. P. and Tildesley, D. J. (1989). *Computer Simulation of Liquids*. Oxford University Press.

[2] Anderson, Jr., J. D. (1995). *Computational Fluid Dynamics*. McGraw-Hill Science/Engineering/Math, 1st edition.

[3] Arroyo, M. and Belytschko, T. (2002). An atomistic-based finite deformation membrane for single layer crystalline films. *Journal of the Mechanics and Physics of Solids*, 50 (9), pp. 1941–1977.

[4] Bathe, K.-J. (1996). *Finite Element Procedures*. Prentice Hall.

[5] Belytschko, T., Liu, W. K., and Moran, B. (2000). *Nonlinear Finite Elements for Continua and Structures*. Wiley, 1st edition.

[6] Berendsen, H. J. C., Grigera, J. R., and Straatsma, T. P. (1987). The missing term in effective pair potentials. *The Journal of Physical Chemistry*, 91 (24), pp. 6269–6271.

[7] Blake, T. D., Clarke, A., Coninck, J. D., de Ruijter, M., and Voue, M. (1999). Droplet spreading: A microscopic approach. *Colloids and Surfaces A: Physicochemical and Engineering Aspects*, 149 (1-3), pp. 123–130.

[8] Blake, T. D., Clarke, A., Coninck, J. D., and de Ruijter, M. J. (1997). Contact angle relaxation during droplet spreading: Comparison between molecular kinetic theory and molecular dynamics. *Langmuuir*, 13 (17), pp. 2164–2166.

[9] Brackbill, J. U., Kothe, D. B., and Zemach, C. (1992). A continuum method for modeling surface tension. *Journal of Computational Physics*, 100 (2), pp. 335–354.

[10] Cho, J. R., Lee, H. W., and Yoo, W. S. (2007). A wet-road braking distance estimate utilizing the hydroplaning analysis of patterned tire. *International Journal for Numerical Methods in Engineering*, 69 (7), pp. 1423–1445.

[11] Choi, J., Cho, M., and Kim, W. (2010). Surface effects on the dynamics behavior of nanosized thin film resonator. *Applied Physics Letters*, 97 (17), pp. 171901–1–171901–3.

[12] Choy, M. M., Cook, W. R., Hearmon, R. F. S., Jaff, J., Jerphagnon, J., Kurtz, S. K., Liu, S. T., and Nelson, D. F. (1971). *Landolt-Bornstein: Numerical data and functional relationships in science and technology new series. Group III: Crystal and solid state physics. Volume 11 (Revised and extented edition of volume III/1 and III/2). Elastic, Piezoelectric, Pyroelectric, Piezooptic, Electrooptic constants, and nonlinear dielectric susceptibilities of crystals*. Springer-Verlag Berlin.

[13] Crowe, C. T., Elger, D. F., Roberson, J. A., and Williams, B. C. (2008). *Engineering Fluid Mechanics*. Wiley, 9th edition.

[14] Daan Frenkel, B. S. (2001). *Understanding Molecular Simulation: From Algorithms to Applications*. Academic Press, 2nd edition.

[15] Daw, M. S. and Baskes, M. I. (1983). Semiempirical, quantum mechanical calculation of hydrogen embrittlement in metals. *Physical Review Letters*, 50 (17), pp. 1285–1288.

[16] Daw, M. S. and Baskes, M. I. (1984). Embedded-atom method: Derivation and application to impurities, surfaces, and other defects in metals. *Physical Review B*, 29 (12), pp. 251–310.

[17] Daw, M. S., Foiles, S. M., and Baskes, M. I. (1993). The embedded-atom method a review of theory and applications. *Materials Science Reports*, 9 (7-8), pp. 251–310.

[18] de Gennes, P. G. (1985). Wetting: Statics and dynamics. *Reviews of Modern Physics*, 57 (3), pp. 827–863.

[19] de Ruijter, M. J., Blake, T. D., and Coninck, J. D. (1999). Dynamic wetting studied by molecular modeling simulations of droplet spreadint. *Langmuuir*, 15 (22), pp. 7836–7847.

[20] Derjaguin, B. V., Muller, V. M., and Toporov, Y. P. (1975). Effect of contact deformation on the adhesion of particles. *Journal of Colloid and Interface Science*, 53 (2), pp. 314–326.

[21] Dussan, V., E. B. (1976). The moving contact line: The slip boundary condition. *Journal of Fluid Mechanics*, 77 (4), pp. 665–684.

[22] Dussan, V., E. B. (1979). On the spreading of liquids on solid surfaces: Static and dynamics contact lines. *Annual Review of Fluid Mechanics*, 11, pp. 371–400.

[23] Ericksen, J. L. (2008). On the cauchy-born rule. *Mathematics and Mechanics of Solids*, 13 (3-4), pp. 199–220.

[24] Fan, C. F. and Cagin, T. (1995). Wetting of crystalline polymer surfaces: A molecular dynamics simulation. *Journal of Chemical Physics*, 103 (20), pp. 9053–9061.

[25] Feng, X.-Q., Gao, X., Wu, Z., Jiang, L., and Zheng, Q.-S. (2007). Superior water repellency of water strider legs with hierarchical structures: Experiments and analysis. *Langmuir*, 23 (9), pp. 4892–4896.

[26] Feng, Z. G., Domaszewski, M., Montavon, G., and Coddet, C. (2002). Finite element analysis of effect of substrate surface roughness on liquid droplet impact and flattening process. *Journal of Thermal Spray Technology*, 11 (1), pp. 62–68.

[27] Foiles, S. M., Baskes, M. I., and Daw, M. S. (1986). Embedded-atom-method functions for the fcc metals cu, ag, au, ni, pd, pt, and their alloys. *Physical Review B*, 33 (12), pp. 7983–7991.

[28] Fukai, J., Zhao, Z., Poulikakos, D., Megaridis, C. M., and Miyatake, O. (1993). Modeling of the deformation of a liquid droplet impinging upon a flat surface. *Physics of Fluids*, 5 (11), pp. 2588–2599.

[29] Guo, X., Wang, J. B., and Zhang, H. W. (2006). Mechanical properties of single-walled carbon nanotubes based on higher order cauchy-born rule. *International Journal of Solids and Structures*, 43 (5), pp. 1276–1290.

[30] Gurtin, M. E., Weissmuller, J., and Larche, F. (1998). A general theory of curved deformable interfaces in solids at equilibrium. *Philosophical Magazine A*, 78 (5), pp. 1093–1109.

[31] Gurtin, M. E. and Murdoch, A. I. (1975). A continuum theory of elastic material surfaces. *Archive for Rational Mechanics and Analysis*, 57 (4), pp. 291–323.

[32] Gurtin, M. E. and Murdoch, A. I. (1978). Surface stress in solids. *International Journal of Solids and Structures*, 14 (6), pp. 431–440.

[33] Haile, J. M. (1997). *Molecular Dynamics Simulation: Elementary Methods*. Wiley-Interscience, 1st edition.

[34] Hata, S., Kai, Y., Yamanaka, I., Oosaki, H., Hirota, K., and Yamazaki, S. (2000). Development of hydrophilic outside mirror coated with titania photocatalyst. *JSAE Review*, 21 (1), pp. 97–102.

[35] Hautman, J. and Klein, M. L. (1991). Microscopic wetting phenomena. *Physical Review Letters*, 67 (13), pp. 1763–1766.

[36] Hisada, T. and Noguchi, H. (1995). *Basis and Application of Nonlinear Finite Element Method (in Japanese)*. Maruzen.

[37] Ho, S.-P. P. and Yeh, Y.-L. (2006). The use of 2d enriched elements with bubble functions for finite element analysis. *Computers and Structures*, 84 (29-30), pp. 2081–2091.

[38] Holian, B. L., Voter, A. F., Wagner, N. J., Ravelo, R. J., Chen, S. P., Hoover, W. G., Hoover, C. G., Hammerberg, J. E., and Dontje, T. D. (1991). Effects of pairwise versus many-body forces on high-stress plastic deformation. *Physical Review A*, 43 (6), pp. 2655–2661.

[39] Holian, B. L. and Ravelo, R. (1995). Fracture simulations using large-scale molecular dynamics. *Physical Review B*, 51 (7), pp. 11275–11288.

[40] Hughes, T. J. R. (2000). *The Finite Element Method: Linear Static and Dynamic Finite Element Analysis*. Dover Publications.

[41] Huh, C. and Scriven, L. E. (1971). Hydrodynamic model of steady movement of a solid/liquid/fluid contact line. *Journal of Colloid and Interface Science*, 35 (1), pp. 85–101.

[42] Israelachvili, J. (1985). *Intermolecular and Surface Forces*. Academic Press.

[43] Johnson, K. L. (1985). *Contact Mechanics*. Cambridge University Press.

[44] Johnson, K., Kendall, K., and Roberts, A. D. (1971). Surface energy and the contact of elastic solids. *Proceedings of the Royal Society A*, 324 (1558), pp. 301–313.

[45] Johnson, R. A. (Springer Verlag, Berlin, 1990). Many atom interactions. *Physics*, 48, p. 85.

[46] Kandlikar, S. G. and Steinke, M. E. (2002). Contact angles and interface behavior during rapid evaporation of liquid on a heated surface. *International Journal of Heat and Mass Transfer*, 45 (18), pp. 3771–3780.

[47] Khoo, B. C., Li, Z., and Lin, P. (2008). *Moving Interface Problems And Applications In Fluid Dynamics: Program On Moving Interface Problems And Applications In Fluid Dynamics*. American Mathematical Society.

[48] Landau, L. D. and Lifshitz, E. M. (1959). *Fluid Mechanics*. Pergamon Press, 2nd edition.

[49] Levich, V. G. and Krylov, V. S. (1969). Surface tension driven phenomena. *Annual Review of Fluid Mechanics*, 1, pp. 293–316.

[50] Li, S. and Wang, G. (2008). *Introduction to Micromechanics and Nanomechanics*. World Scientific Publishing Company.

[51] Li, S. and Sun, B. (2011). *Advances in Cell Mechanics*. Springer.

[52] Li, S. and Sun, B. (2012). *Advances in Soft Matter Mechanics*. Springer.

[53] Lucas, V. R. (1918). Ueber das zeitgesetz des kapillaren aufstiegs von flussigkeiten. *Journal of Nanoscience and Nanotechnology*, 23 (1), pp. 15–22.

[54] Madasu, S. and Cairncross, R. A. (2003). Effect of substrate flexibility on dynamic wetting: A finite element model. *Computer Methods in Applied Mechanics and Engineering*, 192 (25), pp. 2671–2702.

[55] Manservisi, S. and Scardovelli, R. (2009). A variational approach to the contact angle dynamics of spreading droplets. *Computers and Fluids*, 38 (2), pp. 406–424.

[56] Marchand, A., Weijs, J. H., Snoeijer, J. H., and Andreotti, B. (2011). Why is surface tension a force parallel to the interface? *American Journal of Physics*, 79 (10), pp. 999–1008.

[57] Mishin, Y., Farkas, D., Mehl, M. J., and Papaconstantopoulos, D. A. (1999). Interatomic potentials for al and ni from experimental data and ab initio calculations. *Materials Research Society Symposium Proceedings*, 538, pp. 535–540.

[58] Mishin, Y., Mehl, M. J., Papaconstantopoulos, D., Voter, A. F., and Kress, J. D. (2001). Structural stability and lattice defects in copper: Ab initio, tight-binding, and elmbedded-atom calculations. *Physical Review B*, 63 (22), pp. 1–16.

[59] Moffatt, H. K. (1963). Viscous and resistive eddies near a sharp corner. *Journal of Fluid Mechanics*, 18 (1), pp. 1–18.

[60] Nikrityuk, P. A. (2011). *Computational Thermo-Fluid Dynamics: In Materials Science and Engineering*. Wiley-VCH, 1st edition.

[61] Olsson, P. A. T. and Park, H. S. (2012). On the importance of surface elastic contributions to the flexural rigidity of nanowaires. *Journal of the Mechanics and Physics of Solids*, 60 (12), pp. 2064–2083.

[62] Pal Jen Wei, Sheng Chao Chen, J. F. L. (2009). Adhesion forces and contact angles of water strider legs. *Proceedings of the Robotics: Science and Systems*, , pp. 1526–1528.

[63] Park, H. S. and Klein, P. A. (2007). Surface cauchy-born analysis of surface stress effects on metallic nanowires. *Physical Review B*, 75 (8), pp. 085408–1–085408–9.

[64] Park, H. S. and Klein, P. A. (2008). Surface stress effects on the resonant properties of metal nanowires: The importance of finite deformation kinematics and the impact of the residual surface stress. *Journal of the Mechanics and Physics of Solids*, 56 (11), pp. 3144–3166.

[65] Park, H. S., Klein, P. A., and Wagner, G. J. (2006). A surface cauchy-born model for nanoscale materials. *International Journal for Numerical Methods in Engineering*, 68 (10), pp. 1072–1095.

[66] Parsegian, V. A. (2006). *Van Der Waals Forces*. Cambridge University Press, Cambridge.

[67] Peters, J. M. H. (2001). Total curvature of surfaces (via the divergence of the normal). *International Journal of Mathematical Education in Science and Technology*, 32 (6), pp. 795–810.

[68] Qian, T., Wang, X.-P., and Sheng, P. (2006). A variational approach to moving contact line hydrodynamics. *Journal of Fluid Mechanics*, 564, pp. 333–360.

[69] Rapaport, D. C. (2004). *The Art of Molecular Dynamics Simulation*. Cambridge University Press, 2nd edition.

[70] Reddy, J. N. and Gartling, D. K. (2010). *The Finite Element Method in Heat Transfer and Fluid Dynamics, Third Edition*. CRC Press, 3rd edition.

[71] Rehfeldt, F., Engler, A. J., Eckhardt, A., Ahmed, F., and Discher, D. E. (2007). Cell responses to the mechanochemical microenvironment - implications for regenerative medicine and drug delivery. *Advanced Drug Delivery Reviews*, 59 (13), pp. 1329–1339.

[72] Roy, D. N. (1998). *Applied Fluid Mechanics*. Ellis Horwood Ltd.

[73] Sauer, R. A. and Li, S. (2007). An atomic interaction-based continuum model for adhesive contact mechanics. *Finite Elements in Analysis and Design*, 43 (5), pp. 384–396.

[74] Sauer, R. A. and Li, S. (2007). An atomiscically enriched continuum model for nanoscale contact mechanics and its application to contact scaling. *Journal of Nanoscience and Nanotechnology*, 8 (4), pp. 1–17.

[75] Sauer, R. A. and Li, S. (2007). A contact mechanics model for quasi-continua. *International Journal for Numerical Methods in Engineering*, 71 (8), pp. 931–962.

[76] Sauer, R. A. and Wriggers, P. (2009). Formulation and analysis of a three-dimensional finite element implementation for adhesive contact at the nanoscale. *Computer Methods in Applied Mechanics and Engineering*, 198, pp. 3871–3883.

[77] Sauer, R. A. *An Atomic Interaction Based Continuum Model for Computational Multiscale Contact Mechanics*. PhD thesis, University of California, Berkeley, (2006).

[78] Schobeiri, M. T. (2010). *Fluid Mechanics for Engineers: A Graduate Textbook*. Springer.

[79] Shames, I. H. (1992). *Mechanics of Fluids*. Mcgraw-Hill College, 3rd edition.

[80] Sharma, P. and Ganti, S. (2004). Size-dependent eshelby's tensor for embedded nano-inclusions incorporating surface/interface energies. *Journal of Applied Mechanics*, 71 (5), pp. 663–671.

[81] Sikkenk, J. H., Indekeu, J. O., van Leeuwen, J. M. J., and Vossnack, E. O. (1987). Molecular-dynamics simulation of wetting and drying at solid-fluid interfaces. *Physical Review Letters*, 59 (1), pp. 98–101.

[82] Smits, A. J. (1999). *A Physical Introduction to Fluid Mechanics*. Wiley, 1st edition.

[83] Spurk, J. and Aksel, N. (2008). *Fluid Mechanics*. Springer, 2nd edition.

[84] Suhr, S. H., Song, Y. S., Lee, S. J., and Sitti, M. (2005). Biologically inspired miniature water strider robot. *Langmuir*, 25 (3), pp. 1–7.

[85] Sunyk, R. and Steinmann, P. (2003). On higher gradients in continuum-atomistic modelling. *International Journal of Solids and Structures*, 40 (24), pp. 6877–6896.

[86] Tadmor, E. B., Oritz, M., and Phillips, R. (1996). Quasicontinuum analysis of defects in solids. *Philosophical Magazine A*, 73 (6), pp. 1529–1563.

[87] Truesdell, C. A. (1976). *A First Course in Rational Continuum Mechanics (Pure and applied mathematics, a series of monographs and textbooks)*. Academic Press.

[88] Tyson, W. R. and Miller, W. A. (1977). Surface free energies of solid metals estimation from liquid surface tension measurements. *Surface Science*, 62 (1), pp. 267–276.

[89] V., E. B. D. and Davis, S. H. (1974). On the motion of a fluid-fluid interface along a solid surface. *Journal of Fluid Mechanics*, 65 (1), pp. 71–95.

[90] van Swol, F. and Henderson, J. R. (1986). Wetting at a fluid-wall interface. *Journal of the Chemical Society, Faraday Transactions 2*, 82, pp. 1685–1699.

[91] Vargaftik, N. B., Volkov, B. N., and Voljak, L. D. (1983). International tables of the surface tension of water. *Journal of Physical and Chemical Reference Data*, 12 (3), pp. 817–820.

[92] Wadley, H. N. G., Zhou, X., Johnson, R. A., and Neurock, M. (2001). Mechanisms, models and methods of vapor deposition. *Progess in Materials Science*, 46 (3-4), pp. 329–377.

[93] Wadley, H. N. G., Zhou, X., and Johnon, R. A. (2001). Atomic assembly of giant magnetoresistive multilayers. *MRS Proceedings*, 672, pp. O4.1.1–O4.1.14.

[94] Wagner, N. J., Holian, B. L., and Voter, A. F. (1992). Molecular-dynamics simulations of two-dimensional materials at high strain rates. *Physical Review A*, 45 (12), pp. 8457–8470.

[95] Wang, X., Peng, X., and Lee, D. (2003). Dynamic wetting and stress singularity on contact line. *Science in China*, 46 (4), pp. 407–417.

[96] Washburn, E. W. (1921). The dynamics of capillary flow. *Physical Review*, 17 (3), pp. 273–283.

[97] Young, T. (1805). An essay on the cohesion of fluids. *Philosophical Transactions of the Royal Society*, 95, pp. 65–87.

[98] Zanzotto, G. (1996). The cauchy-born hypothesis, nonlinear elasticity and mechanical twinning in crystals. *Acta Crystallographica Section A*, 52, pp. 839–849.

[99] Zeng, X. and Li, S. (2011). Multiscale modeling and simulation of soft adhesion and contact of stem cells. *Journal of the Mechanical Behavior of Biomedical Materials*, 4 (2), pp. 180–189.

[100] Zhong, Y. and Zhu, T. (2008). Simulating nanoindentation and predicting dislocation nucleation using interatomic potential finite element method. *Computer Methods in Applied Mechanics and Engineering*, 197 (41-42), pp. 3174–3181.

[101] Zhou, X. W., Johnson, R. A., and Wadley, H. N. G. (2004). Misfit-energy-increasing dislocations in vapor-deposited cofe/nife multilayers. *Physical Review B*, 69 (14), pp. 144113–1–144113–10.

[102] Zhou, X. W., Wadley, H. N. G., Johnson, R. A., Larson, D. J., Tabata, N., Cerezo, A., Petford-Long, A. K., Smith, G. D. W., Clifton, P. H., Martens, R. L., and Kelly, T. F. (2001). Atomic scale structure of sputtered metal multilayers. *Acta Materialia*, 49 (19), pp. 4005–4015.

[103] Zhu, T., Li, J., Vliet, K. J. V., Ogata, S., Yip, S., and Suresh, S. (2004). Predictive modeling of nanoindentation-induced homogeneous dislocation nucleation in copper. *Journal of the Mechanics and Physics of Solids*, 52 (3), pp. 691–724.

Appendix A

The Total Curvature

A.1 A Relationship Between the Total Curvature and the Normal Vector

Here, we discuss a relationship between the total curvature and the normal vector. Consider an infinitesimal part of a curve, shown in Figure A.1. If ab is an arc, Δs can be

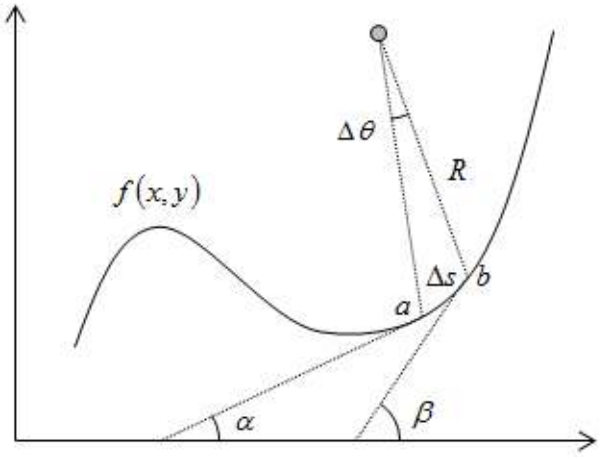

Figure A.1: An infinitesimal part of a curve.

approximated as $\Delta s = R\Delta\theta$. Δs and $\Delta\theta$ can be whiten as

$$\Delta s = \sqrt{\Delta x^2 + \Delta y^2}, \tag{A.1}$$

and

$$\Delta\theta = \beta - \alpha \tag{A.2}$$
$$\approx \tan(\beta - \alpha) \tag{A.3}$$
$$= \frac{\tan\beta - \tan\alpha}{1 + \tan\beta\tan\alpha} \tag{A.4}$$
$$= \frac{\frac{dy}{dx}(b) - \frac{dy}{dx}(a)}{1 + \frac{dy}{dx}(b)\frac{dy}{dx}(a)}. \tag{A.5}$$

Thus, the radius R is given by

$$R = \frac{\left\{1 + \frac{dy}{dx}(b)\frac{dy}{dx}(a)\right\}\sqrt{1 + \left(\frac{\Delta y}{\Delta x}\right)^2}}{\frac{\frac{dy}{dx}(b) - \frac{dy}{dx}(a)}{\Delta x}}. \tag{A.6}$$

Taking the limit $\Delta \to 0$, we have

$$\lim_{\Delta\to 0} R = \frac{\left(1 + \frac{d^2y}{dx^2}\right)^{3/2}}{\frac{d^2y}{dx^2}} \tag{A.7}$$
$$= -\frac{\left(1 + \left(-\frac{f_{,x}}{f_{,y}}\right)^2\right)^{3/2}}{-\frac{\partial}{\partial x}\frac{f_{,x}}{f_{,y}} + \frac{\partial}{\partial y}\frac{f_{,x}}{f_{,y}}\frac{dy}{dx}} \tag{A.8}$$
$$= -\frac{\left(f_{,x}^2 + f_{,y}^2\right)^{3/2}}{f_{,x}^2 f_{,yy} - 2f_{,x}f_{,y}f_{,xy} + f_{,y}^2 f_{,xx}}, \tag{A.9}$$

where the implicit function theorem is applied. Since the total curvature κ is defined as $\kappa = \frac{1}{R}$,

$$\kappa = \frac{f_{,x}^2 f_{,yy} - 2f_{,x}f_{,y}f_{,xy} + f_{,y}^2 f_{,xx}}{\left(f_{,x}^2 + f_{,y}^2\right)^{3/2}}. \tag{A.10}$$

On the other hand, the normal vector is given by

$$\mathbf{n} = \frac{1}{\sqrt{f_{,x}^2 + f_{,y}^2}}\begin{pmatrix} f_{,x} \\ f_{,y} \end{pmatrix}. \tag{A.11}$$

Thus, the divergence of the normal vector can be obtained as

$$\nabla \cdot \mathbf{n} = \frac{f_{,x}^2 f_{,yy} - 2 f_{,x} f_{,y} f_{,xy} + f_{,y}^2 f_{,xx}}{\left(f_{,x}^2 + f_{,y}^2\right)^{3/2}}. \tag{A.12}$$

Comparing Equation (A.10) and (A.12), we obtain the relationship between the curvature and the normal vector,

$$\kappa = |\nabla \cdot \mathbf{n}|. \tag{A.13}$$

A.2 An Analytical Formulation of the Total Curvature Based on Nanson's Formula

The normal vector in the current configuration can be obtained by Nanson's formula, and its index notation is given by

$$n_i = \sqrt{N_A C_{AB}^{-1} N_B} F_{Ci}^{-1} N_C. \tag{A.14}$$

The total curvature is given by

$$\begin{aligned}
\frac{\partial n_i}{\partial x_i} &= -\frac{\left(\frac{\partial N_A}{\partial x_i} C_{AB}^{-1} N_B + N_A \frac{\partial C_{AB}^{-1}}{\partial x_i} N_B + N_A C_{AB}^{-1} \frac{\partial N_B}{\partial x_i}\right) F_{Ci}^{-1} N_C}{2\left(N_A C_{AB}^{-1} N_B\right)^{3/2}} \\
&\quad + \sqrt{N_A C_{AB}^{-1} N_B} \frac{\partial F_{Ci}^{-1}}{\partial x_i} N_C + \sqrt{N_A C_{AB}^{-1} N_B} F_{Ci}^{-1} \frac{\partial N_C}{\partial x_i} \qquad \text{(A.15)} \\
&= -\frac{\left(\frac{\partial N_A}{\partial X_D} F_{Di}^{-1} C_{AB}^{-1} N_B + N_A \frac{\partial C_{AB}^{-1}}{\partial X_D} F_{Di}^{-1} N_B + N_A C_{AB}^{-1} \frac{\partial N_B}{\partial X_D} F_{Di}^{-1}\right) F_{Ci}^{-1} N_C}{2\left(N_A C_{AB}^{-1} N_B\right)^{3/2}} \\
&\quad + \sqrt{N_A C_{AB}^{-1} N_B} \frac{\partial F_{Ci}^{-1}}{\partial X_D} F_{Di}^{-1} N_C + \sqrt{N_A C_{AB}^{-1} N_B} F_{Ci}^{-1} \frac{\partial N_C}{\partial X_D} F_{Di}^{-1} \qquad \text{(A.16)} \\
&= -\frac{\left(N_A \frac{\partial C_{AB}^{-1}}{\partial X_D} N_B + 2 N_A C_{AB}^{-1} \frac{\partial N_B}{\partial X_D}\right) C_{DC}^{-1} N_C}{2\left(N_A C_{AB}^{-1} N_B\right)^{3/2}} \\
&\quad + \sqrt{N_A C_{AB}^{-1} N_B} \frac{\partial F_{Ci}^{-1}}{\partial X_D} F_{Di}^{-1} N_C + \sqrt{N_A C_{AB}^{-1} N_B} C_{CD}^{-1} \frac{\partial N_C}{\partial X_D}. \qquad \text{(A.17)}
\end{aligned}$$

The derivative of the inverse of the deformation gradient tensor can be obtained as

$$\begin{aligned}
F_{Ci}^{-1} F_{iB} &= \delta_{CB} && \text{(A.18)} \\
\frac{\partial F_{Ci}^{-1}}{\partial X_D} F_{iB} + F_{Cj}^{-1} \frac{\partial F_{jB}}{\partial X_D} &= 0 && \text{(A.19)} \\
&= -F_{Cj}^{-1} G_{jBD} F_{Bi}^{-1}, && \text{(A.20)}
\end{aligned}$$

where

$$G_{iAB} = \frac{\partial F_{iA}}{\partial X_B}. \tag{A.21}$$

Similarly, the derivative of the inverse of the Right-Cauchy Green tensor is given by

$$C^{-1}_{AB} C_{BC} = \delta_{AC} \tag{A.22}$$

$$\frac{\partial C^{-1}_{AB}}{\partial X_D} C_{BC} + C^{-1}_{AE} \frac{\partial C_{EC}}{\partial X_D} = 0 \tag{A.23}$$

$$\frac{\partial C^{-1}_{AB}}{\partial X_D} = -C^{-1}_{AE} \frac{\partial C_{EC}}{\partial X_D} C^{-1}_{CB} \tag{A.24}$$

$$= -C^{-1}_{AE} \left(\frac{\partial F_{iE}}{\partial X_D} F_{iC} + F_{iE} \frac{\partial F_{iC}}{\partial X_D} \right) C^{-1}_{CB} \tag{A.25}$$

$$= -2 C^{-1}_{AE} G_{iED} F_{iC} C^{-1}_{CB}. \tag{A.26}$$

Thus, the total curvature is given by

$$\frac{\partial n_i}{\partial x_i} = \frac{\left(N_A C^{-1}_{AE} G_{iED} F_{iC} C^{-1}_{CB} N_B - N_A C^{-1}_{AB} \frac{\partial N_B}{\partial X_D} \right) C^{-1}_{DC} N_C}{\left(N_A C^{-1}_{AB} N_B \right)^{3/2}} - n_j G_{jBD} C^{-1}_{BD} + \sqrt{N_A C^{-1}_{AB} N_B} C^{-1}_{CD} \frac{\partial N_C}{\partial X_D}. \tag{A.27}$$

In vector notation, the total curvature is given by

$$\nabla \cdot \mathbf{n} = \frac{\mathbf{F}^T \mathcal{G} \vdots (\mathbf{C}^{-1}\mathbf{N} \otimes \mathbf{C}^{-1}\mathbf{N} \otimes \mathbf{C}^{-1}\mathbf{N}) - \nabla_{\mathbf{X}} \mathbf{N} : (\mathbf{C}^{-1}\mathbf{N} \otimes \mathbf{C}^{-1}\mathbf{N})}{(\mathbf{N} \cdot \mathbf{C}^{-1}\mathbf{N})^{3/2}} - \left(\mathbf{n}^T \mathcal{G} \right) : \mathbf{C}^{-1} + \sqrt{\mathbf{N} \cdot \mathbf{C}^{-1}\mathbf{N}} \mathbf{C}^{-1} : \nabla_{\mathbf{X}} \mathbf{N}. \tag{A.28}$$

Appendix B

A Validation of the Galerkin Weak Formulation of Dynamic Wetting

Consider a two dimensional wettability problem shown in Figure B.1. There are three

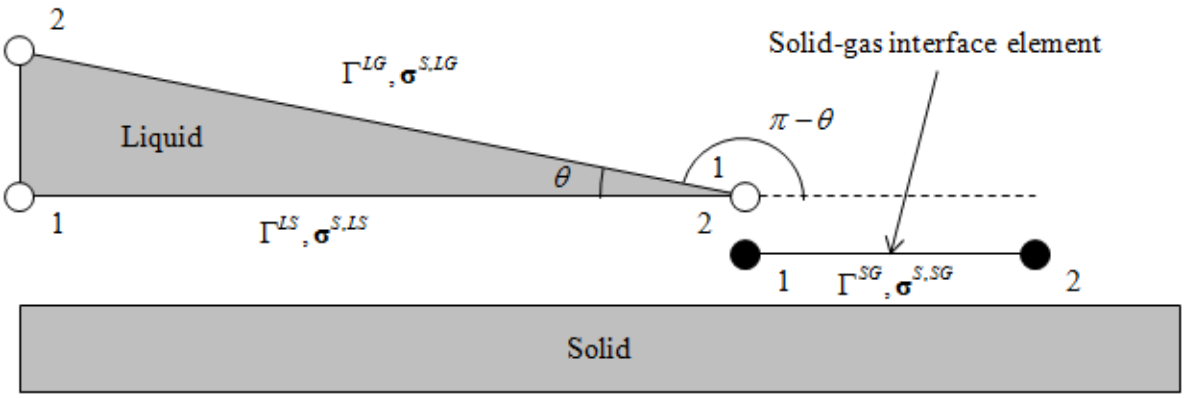

Figure B.1: A two dimensional wettability problem.

elements, between the liquid and gas, between the liquid and gas, and between the solid and gas, Γ^{LG}, Γ^{LS} and Γ^{SG}. The surface stresses are assumed to be only the first term of the Gurtin-Murdoch surface elasticity model,

$$\boldsymbol{\sigma}^{S,LG} = \gamma^{LG}\mathbf{P}^{LG} \tag{B.1}$$

$$= \begin{pmatrix} \gamma^{LG}\cos^2\theta & -\gamma^{LG}\cos\theta\sin\theta \\ -\gamma^{LG}\cos\theta\sin\theta & \gamma^{LG}\sin^2\theta \end{pmatrix}, \tag{B.2}$$

and

$$\boldsymbol{\sigma}^{S,LS} = \gamma^{LS}\mathbf{P}^{LS} \tag{B.3}$$

$$= \begin{pmatrix} \gamma^{LS} & 0 \\ 0 & 0 \end{pmatrix}, \tag{B.4}$$

and

$$\boldsymbol{\sigma}^{S,SG} = \gamma^{SG}\mathbf{P}^{SG} \tag{B.5}$$

$$= \begin{pmatrix} \gamma^{SG} & 0 \\ 0 & 0 \end{pmatrix}. \tag{B.6}$$

One dimensional shape functions, which are functions of the local coordinate x', are given by

$$N_1(x') = \frac{1}{\Gamma}(\Gamma - x'), \tag{B.7}$$

and

$$N_2(x') = \frac{1}{\Gamma}x', \tag{B.8}$$

where Γ is the length, and $x' = 0$ at node 1 and $x' = \Gamma$ at node 2. The derivatives of shape functions with respect to the local coordinate are given by

$$\frac{\partial N_1}{\partial x'} = -\frac{1}{\Gamma}, \tag{B.9}$$

and

$$\frac{\partial N_2}{\partial x'} = \frac{1}{\Gamma}. \tag{B.10}$$

First, consider the element between the liquid and solid. Since the rotation matrix is the unit matrix $\mathbf{R} = \mathbf{I}$, the derivatives of shape functions with respect to the global and local coordinate are the same. The nodal surface inertia force at node 2 which comes from the element between the liquid and solid is given by

$$\mathbf{F}^{S,LS,2} = -\int_{\Gamma^L S} \boldsymbol{\sigma}^{S,LS}\frac{\partial N^i}{\partial \mathbf{x}}ds \tag{B.11}$$

$$= -\Gamma \begin{pmatrix} \gamma^{LS} & 0 \\ 0 & 0 \end{pmatrix} \begin{pmatrix} \frac{1}{\Gamma} \\ 0 \end{pmatrix} \tag{B.12}$$

$$= -\begin{pmatrix} \gamma^{LS} \\ 0 \end{pmatrix}. \tag{B.13}$$

Second, consider the element between the liquid and gas. The rotation matrix is given by

$$\mathbf{R} = \begin{pmatrix} -\cos\theta & -\sin\theta \\ \sin\theta & -\cos\theta \end{pmatrix}, \tag{B.14}$$

where θ is the contact angle. Hence, the derivatives of shape functions with respect to the global coordinate at node 1 are given by

$$\begin{pmatrix} \frac{\partial N_1}{\partial x} \\ \frac{\partial N_1}{\partial y} \end{pmatrix} = \mathbf{R} \cdot \begin{pmatrix} \frac{\partial N_1}{\partial x'} \\ 0 \end{pmatrix} \tag{B.15}$$

$$= \begin{pmatrix} \frac{1}{\Gamma}\cos\theta \\ -\frac{1}{\Gamma}\sin\theta \end{pmatrix}. \tag{B.16}$$

Thus, the nodal surface inertia force at node 1 which comes from the element between the liquid and gas is given by

$$\mathbf{F}^{S,LG,1} = -\int_{\Gamma^L G} \boldsymbol{\sigma}^{S,LG} \frac{\partial N^i}{\partial \mathbf{x}} ds \tag{B.17}$$

$$= -\Gamma^{LG} \begin{pmatrix} \gamma^{LG}\cos^2\theta & -\gamma^{LG}\cos\theta\sin\theta \\ -\gamma^{LG}\cos\theta\sin\theta & \gamma^{LG}\sin^2\theta \end{pmatrix} \begin{pmatrix} \frac{1}{\Gamma^{LG}}\cos\theta \\ -\frac{1}{\Gamma^{LG}}\sin\theta \end{pmatrix} \tag{B.18}$$

$$= \begin{pmatrix} -\gamma^{LG}\cos\theta \\ \gamma^{LG}\sin\theta \end{pmatrix}. \tag{B.19}$$

Third, the rotation matrix of the solid gas interaction element is the unit matrix. The nodal surface inertia force at node 1 which comes from the solid gas interaction is given by

$$\mathbf{F}^{S,SG,1} = -\boldsymbol{\sigma}^{S,SG}\mathbf{R}^T \begin{pmatrix} -1 \\ 1 \end{pmatrix} \tag{B.20}$$

$$= -\begin{pmatrix} \gamma^{SG} & 0 \\ 0 & 0 \end{pmatrix} \begin{pmatrix} 1 & 0 \\ 0 & 1 \end{pmatrix} \begin{pmatrix} -1 \\ 0 \end{pmatrix} \tag{B.21}$$

$$= \begin{pmatrix} \gamma^{SG} \\ 0 \end{pmatrix}. \tag{B.22}$$

Thus, the resultant force at the contact line is given by

$$\mathbf{F}^{S,LS,2} + \mathbf{F}^{S,LG,1} + \mathbf{F}^{S,SG,1} = \begin{pmatrix} \gamma^{SG} - \gamma^{LG}\cos\theta - \gamma^{LS} \\ \gamma^{LG}\sin\theta \end{pmatrix}. \tag{B.23}$$

Since this result is completely the same as Equation, Galerkin weak formulation is validated.

Appendix C

Higher Order Deformation Gradient Tensors

In this appendix, the computational method of the curvature and the higher order Cauchy-Born rule in the Finite Element Method is discussed. The second and third order deformation gradient tensors are defined as

$$\mathcal{G} = \frac{\partial^2 \mathbf{x}}{\partial \mathbf{X} \otimes \partial \mathbf{X}}, \tag{C.1}$$

and

$$\mathbb{H} = \frac{\partial^3 \mathbf{x}}{\partial \mathbf{X} \otimes \partial \mathbf{X} \otimes \partial \mathbf{X}}. \tag{C.2}$$

The higher order deformation gradient tensors can be computed by using FEM shape functions,

$$\mathcal{G} = \sum_{I}^{nnode} \frac{\partial^2 N^I}{\partial \mathbf{X} \otimes \partial \mathbf{X}} \mathbf{x}^I, \tag{C.3}$$

and

$$\mathbb{H} = \sum_{I}^{nnode} \frac{\partial^3 N^I}{\partial \mathbf{X} \otimes \partial \mathbf{X} \otimes \partial \mathbf{X}} \mathbf{x}^I, \tag{C.4}$$

where *nnode* is the total number of nodes, N^I is FEM shape function for the I-th node, and $\mathbf{x}^I$ is nodal coordinate in the current configuration. Hence, the derivatives of shape functions with respect to the coordinates in the reference configuration $\mathbf{X}$ are necessary. Here, shape functions are assumed to be the function of the natural coordinates $\boldsymbol{\xi}$ in the following sections.

Note that a four node linear quadrilateral element can be applied to compute the higher order deformation gradient tensor, because it has a bilinear term $\xi\eta$. Since the second order derivatives of shape functions with respect to the same variable are zero, the element can compute the higher order deformation gradient tensor when only the higher order shear

deformation exist. Thus, the higher order element should be applied to compute the higher order derivatives accurately.

C.1 The First Order Derivatives of Shape Functions

By using the chain rule, the first order derivatives of shape functions with respect to the natural coordinates $\boldsymbol{\xi}$ in index notation can be written as

$$\frac{\partial N^I}{\partial \xi_i} = \frac{\partial N^I}{\partial X_j}\frac{\partial X_j}{\partial \xi_i}. \tag{C.5}$$

Thus,

$$\frac{\partial N^I}{\partial X_j} = \frac{\partial N^I}{\partial \xi_i}\frac{\partial \xi_i}{\partial X_j}, \tag{C.6}$$

where

$$\frac{\partial \xi_i}{\partial X_j} = \left(\frac{\partial X_j}{\partial \xi_i}\right)^{-1} \tag{C.7}$$

$$= \left(\sum_J^{nnode} \frac{\partial N^J}{\partial \xi_i} X_j^J\right)^{-1}. \tag{C.8}$$

C.2 The Second Order Derivatives of Shape Functions

By using the chain rule and the first order derivatives of shape functions, the second order derivatives of shape functions with respect to the natural coordinates $\boldsymbol{\xi}$ are given by

$$\frac{\partial^2 N^I}{\partial \xi_i \partial \xi_j} = \frac{\partial^2 N^I}{\partial X_m \partial X_k}\frac{\partial X_m}{\partial \xi_i}\frac{\partial X_k}{\partial \xi_j} + \frac{\partial N^I}{\partial X_\ell}\frac{\partial^2 X_\ell}{\partial \xi_i \partial \xi_j}. \tag{C.9}$$

Thus,

$$\frac{\partial^2 N^I}{\partial X_m \partial X_k} = \left(\frac{\partial^2 N^I}{\partial \xi_i \partial \xi_j} - \frac{\partial N^I}{\partial X_\ell}\frac{\partial^2 X_\ell}{\partial \xi_i \partial \xi_j}\right)\frac{\partial \xi_i}{\partial X_m}\frac{\partial \xi_j}{\partial X_k}, \tag{C.10}$$

where

$$\frac{\partial^2 X_\ell}{\partial \xi_i \partial \xi_j} = \sum_J^{nnode} \frac{\partial^2 N^J}{\partial \xi_i \partial \xi_j} X_\ell^J. \tag{C.11}$$

C.3 The Third Order Derivatives of Shape Functions

By using the chain rule, and the first and second order derivatives of shape functions, the second order derivatives of shape functions with respect to the natural coordinates $\boldsymbol{\xi}$ are

given by

$$\frac{\partial^3 N^I}{\partial\xi_i\partial\xi_j\partial\xi_k} = \frac{\partial^3 N^I}{\partial X_n\partial X_m\partial X_\ell}\frac{\partial X_n}{\partial\xi_i}\frac{\partial X_m}{\partial\xi_j}\frac{\partial X_\ell}{\partial\xi_k} + \frac{\partial^2 N^I}{\partial X_m\partial X_\ell}\frac{\partial^2 X_m}{\partial\xi_i\partial\xi_j}\frac{\partial X_\ell}{\partial\xi_k} + \frac{\partial^2 N^I}{\partial X_m\partial X_\ell}\frac{\partial X_m}{\partial\xi_j}\frac{\partial^2 X_\ell}{\partial\xi_i\partial\xi_k} + \frac{\partial^2 N^I}{\partial X_n\partial X_m}\frac{\partial X_n}{\partial\xi_i}\frac{\partial^2 X_m}{\partial\xi_j\partial\xi_k} + \frac{\partial N^I}{\partial X_m}\frac{\partial^3 X_m}{\partial\xi_i\partial\xi_j\partial\xi_k}. \tag{C.12}$$

Thus,

$$\begin{aligned}\frac{\partial^3 N^I}{\partial X_i\partial X_j\partial X_k} = {} & \frac{\partial^3 N^I}{\partial\xi_n\partial\xi_m\partial\xi_\ell}\frac{\partial\xi_n}{\partial X_i}\frac{\partial\xi_m}{\partial X_j}\frac{\partial\xi_\ell}{\partial X_k} - \frac{\partial^2 N^I}{\partial X_\ell\partial X_k}\frac{\partial^2 X_\ell}{\partial\xi_n\partial\xi_m}\frac{\partial\xi_n}{\partial X_i}\frac{\partial\xi_m}{\partial X_j} \\ & - \frac{\partial^2 N^I}{\partial X_j\partial X_m}\frac{\partial^2 X_m}{\partial\xi_n\partial\xi_\ell}\frac{\partial\xi_n}{\partial X_i}\frac{\partial\xi_\ell}{\partial X_k} - \frac{\partial^2 N^I}{\partial X_i\partial X_n}\frac{\partial^2 X_n}{\partial\xi_m\partial\xi_\ell}\frac{\partial\xi_m}{\partial X_j}\frac{\partial\xi_\ell}{\partial X_k} \\ & - \frac{\partial N^I}{\partial X_o}\frac{\partial^3 X_o}{\partial\xi_n\partial\xi_m\partial\xi_\ell}\frac{\partial\xi_n}{\partial X_i}\frac{\partial\xi_m}{\partial X_j}\frac{\partial\xi_\ell}{\partial X_k},\end{aligned} \tag{C.13}$$

where

$$\frac{\partial^3 X_o}{\partial\xi_n\partial\xi_m\partial\xi_\ell} = \sum_J^{nnode}\frac{\partial^3 N^J}{\partial\xi_n\partial\xi_m\partial\xi_\ell}X_o^J. \tag{C.14}$$

Appendix D

The Embedded Atom Method

D.1 The Embedded Atom Method: Mishin et al.

In this section, the Embedded Atom Method developed by Mishin et al. [57] [58] is introduced, and it is called EAM-Mishin in this dissertation. In this scheme, the potential is generated directly in the effective pair format [45]. The pairwise interaction function is parametrized as

$$\begin{aligned}\phi(r) = &\left[E_1 M\left(r, r_0^{(1)}, \alpha_1\right) + E_2 M\left(r, r_0^{(2)}, \alpha_2\right) + \delta\right] \psi\left(\frac{r - r_c}{h}\right) \\ &- \sum_{n=1}^{3} H\left(r_s^{(n)} - r\right) S_n \left(r_S^{(n)} - r\right)^4,\end{aligned} \tag{D.1}$$

where

$$M(r, r_0, \alpha) = \exp\left[-2\alpha(r - r_0)\right] - 2\exp\left[-\alpha(r - r_0)\right] \tag{D.2}$$

is the Morse function, and

$$\psi(x) = \begin{cases} 0 & x \geq 0 \\ \dfrac{x^4}{1 + x^4} & x < 0 \end{cases} \tag{D.3}$$

is the cutoff function, and $H(x)$ is the unit step function. The last term in Equation (D.1) is added to control the strength of pairwise repulsion between atoms at short distances. Here, E_1, E_2, $r_0^{(1)}$, $r_0^{(2)}$, α_1, α_2, δ, r_c, h, $r_s^{(1)}$, $r_s^{(2)}$, $r_s^{(3)}$, S_1, S_2, and S_3 are the material parameters.

The derivatives of each function are followings,

$$\begin{aligned}\frac{\partial\phi(r)}{\partial r} &= \left[E_1\frac{\partial M}{\partial r}\left(r,r_0^{(1)}\right)+E_2\frac{\partial M}{\partial r}\left(r,r_0^{(2)}\right)\right]\psi\left(\frac{r-r_c}{h}\right)\\ &+\left[E_1 M\left(r,r_0^{(1)}\right)+E_2 M\left(r,r_0^{(2)}\right)+\delta\right]\frac{\partial\psi}{\partial r}\left(\frac{r-r_c}{h}\right)\\ &+\sum_{n=1}^{3}\left\{4H\left(r_s^n-r\right)S_n\left(r_S^{(n)}-r\right)^3\right\},\end{aligned} \tag{D.4}$$

and

$$\frac{\partial M}{\partial r}(r,r_0,\alpha) = -2\alpha\exp\left[-2\alpha\left(r-r_0\right)\right]+2\alpha\exp\left[-\alpha\left(r-r_0\right)\right], \tag{D.5}$$

and

$$\frac{\partial\psi}{\partial x}(x) = \begin{cases} 0 & x\geq 0 \\ \dfrac{4x^3}{\left(1+x^4\right)^2} & x<0 \end{cases}. \tag{D.6}$$

The electron density function is taken in the form,

$$\rho(r) = \left[a\exp\left(-\beta_1\left(r-r_0^{(3)}\right)^2\right)+\exp\left(-\beta_2\left(r-r_0^{(4)}\right)\right)\right]\psi\left(\frac{r-r_c}{h}\right), \tag{D.7}$$

and a, $r_0^{(3)}$, $r_0^{(4)}$, β_1 and β_2 are the additional material parameters. The derivative of the electron density function is given by

$$\begin{aligned}\frac{\partial\rho(r)}{\partial r} &= -\left[2a\beta_1\left(r-r_0^{(3)}\right)\exp\left(-\beta_1\left(r-r_0^{(3)}\right)^2\right)+\beta_2\exp\left(-\beta_2\left(r-r_0^{(4)}\right)\right)\right]\psi\left(\frac{r-r_c}{h}\right)\\ &+\left[a\exp\left(-\beta_1\left(r-r_0^{(3)}\right)^2\right)+\exp\left(-\beta_2\left(r-r_0^{(4)}\right)\right)\right]\frac{\partial\psi}{\partial r}\left(\frac{r-r_c}{h}\right).\end{aligned} \tag{D.8}$$

The embedding energy function is represented by a polynomial,

$$F(\rho+1) = \begin{cases} F^{(0)}+\dfrac{1}{2}F^{(2)}\rho^2+\displaystyle\sum_{n=1}^{4}q_n\rho^{n+2} & \rho\leq 0 \\ \dfrac{F^{(0)}+\frac{1}{2}F^{(2)}\rho^2+q_1\rho^3+Q_1\rho^4}{1+Q_2\rho^3} & \rho>0 \end{cases}, \tag{D.9}$$

where $F^{(0)}$, $F^{(2)}$, q_1, q_2, q_3, q_4, Q_1 and Q_2 are the additional material parameters. The derivative of the embedding energy function is given by

$$\frac{\partial F}{\partial\rho}(\rho+1) = \begin{cases} F^{(2)}\rho+\displaystyle\sum_{n=1}^{4}(n+2)\,q_n\rho^{n+1} & \rho\leq 0 \\ \dfrac{F^{(2)}+3q_1\rho^2+4Q_1\rho^3}{1+Q_2\rho^3}-3Q_2\rho^2\dfrac{F^{(0)}+\frac{1}{2}F^{(2)}\rho^2+q_1\rho^3+Q_1\rho^4}{\left(1+Q_2\rho^3\right)^2} & \rho>0 \end{cases}. \tag{D.10}$$

Finally, there are twenty eight material parameters. Table D.1 shows the material parameters of the EAM-Mishin for copper [57].

Parameter		Value	Parameter		Value
r_c	$[\mathring{A}]$	5.50679	S_3	$[eV/\mathring{A}^4]$	1.15000×10^3
h	$[\mathring{A}]$	0.50037	a		3.80362
E_1	$[eV]$	2.01458×10^2	$r_0^{(3)}$	$[\mathring{A}]$	-2.19885
E_2	$[eV]$	6.59288×10^{-3}	$r_0^{(4)}$	$[\mathring{A}]$	-2.61984×10^2
$r_0^{(1)}$	$[\mathring{A}]$	0.83591	β_1	$[\mathring{A}^{-2}]$	0.17394
$r_0^{(2)}$	$[\mathring{A}]$	4.46867	β_2	$[\mathring{A}^{-1}]$	5.35661×10^2
α_1	$[\mathring{A}^{-1}]$	2.97758	$F^{(0)}$	$[eV]$	-2.28235
α_2	$[\mathring{A}^{-1}]$	1.54927	$F^{(2)}$	$[eV]$	1.35535
δ	$[eV]$	0.86225×10^{-2}	q_1	$[eV]$	-1.27775
$r_s^{(1)}$	$[\mathring{A}]$	2.24000	q_2	$[eV]$	-0.86074
$r_s^{(2)}$	$[\mathring{A}]$	1.80000	q_3	$[eV]$	1.78804
$r_s^{(3)}$	$[\mathring{A}]$	1.20000	q_4	$[eV]$	2.97571
S_1	$[eV/\mathring{A}^4]$	4.00000	Q_1		0.40000
S_2	$[eV/\mathring{A}^4]$	40.0000	Q_2		0.30000

Table D.1: The material parameters of the EAM-Mishin for copper [57].

Figure D.1, D.2 and D.3 show the pairwise interaction, electron density and embedding energy function of copper for the EAM-Mishin.

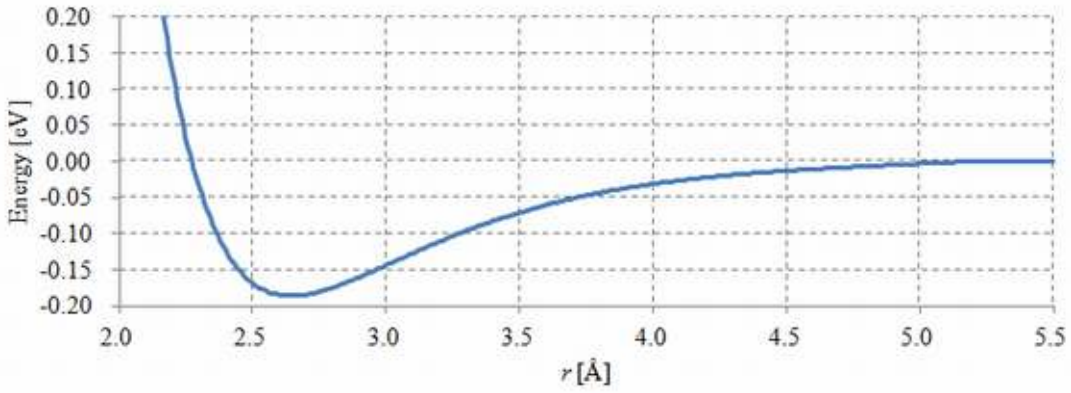

Figure D.1: The pairwise interaction function of copper for the EAM-Mishin.

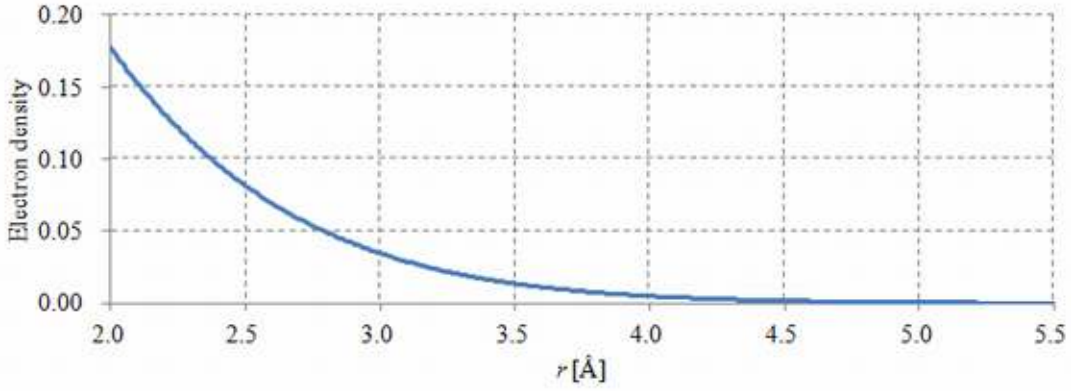

Figure D.2: The electron density function of copper for the EAM-Mishin.

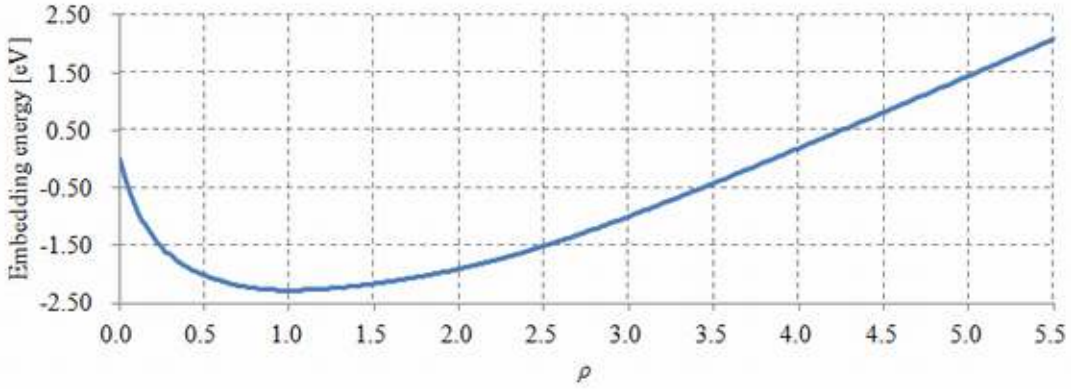

Figure D.3: The embedding energy function of copper for the EAM-Mishin.

D.2 The Embedded Atom Method: Wadley et al. Model

In this section, the Embedded Atom Method developed by Wadley et al. [93], [101], [102] is introduced. This method is called EAM-Wadley in this dissertation.

The alloy Embedded Atom Mothod can be constructed from the elemental Embedded Atom Method if the potentials are normalized [92], and unified cutoff functions are used. To fit the Embedded Atom Method set, the generalized pairwise interaction function for a given element is chosen to have the form,

$$\phi(r) = \frac{A\exp\left[-\alpha\left(\frac{r}{r_e}-1\right)\right]}{1+\left(\frac{r}{r_e}-\kappa\right)^{20}} - \frac{B\exp\left[-\beta\left(\frac{r}{r_e}-1\right)\right]}{1+\left(\frac{r}{r_e}-\lambda\right)^{20}}, \tag{D.11}$$

where r_e is the equilibrium distance between nearest neighbors, A, B, α and β are four adjustable parameters, and κ and λ are two additional parameters for the cutoff. The derivative of the pairwise interaction function is given by

$$\begin{aligned}\frac{\partial\phi}{\partial r}(r) = &-20\left(\frac{r}{r_e}-\kappa\right)^{19}\frac{A\exp\left[-\alpha\left(\frac{r}{r_e}-1\right)\right]}{r_e\left(1+\left(\frac{r}{r_e}-\kappa\right)^{20}\right)^2} - \frac{\alpha A\exp\left[-\alpha\left(\frac{r}{r_e}-1\right)\right]}{r_e\left(1+\left(\frac{r}{r_e}-\kappa\right)^{20}\right)} \\ &+20\left(\frac{r}{r_e}-\lambda\right)^{19}\frac{B\exp\left[-\beta\left(\frac{r}{r_e}-1\right)\right]}{r_e\left(1+\left(\frac{r}{r_e}-\lambda\right)^{20}\right)^2} + \frac{\beta B\exp\left[-\beta\left(\frac{r}{r_e}-1\right)\right]}{r_e\left(1+\left(\frac{r}{r_e}-\lambda\right)^{20}\right)}.\end{aligned} \tag{D.12}$$

The electron density function is taken with the same form as the attractive term in the pair potential with the same values of β and λ,

$$\rho(r) = \frac{f_e\exp\left[-\beta\left(\frac{r}{r_e}-1\right)\right]}{1+\left(\frac{r}{r_e}-\lambda\right)^{20}}. \tag{D.13}$$

The derivative of the electron density is given by

$$\frac{\partial\rho}{\partial r}(r) = -20\left(\frac{r}{r_e}-\lambda\right)^{19}\frac{f_e\exp\left[-\beta\left(\frac{r}{r_e}-1\right)\right]}{r_e\left(1+\left(\frac{r}{r_e}-\lambda\right)^{20}\right)^2} - \frac{\beta f_e\exp\left[-\beta\left(\frac{r}{r_e}-1\right)\right]}{r_e\left(1+\left(\frac{r}{r_e}-\lambda\right)^{20}\right)}. \tag{D.14}$$

To have embedding energy functions that can work well over a wide range of electron density, three equations are used to separately fit to different electron density ranges. For a smooth variation of the embedding energy, these equations are required to match values and slopes at their junctions. These equations are listed in the following,

$$F(\rho) = \begin{cases} \sum_{i=0}^{3} F_{ni} \left(\frac{\rho}{\rho_n} - 1 \right)^i & \rho < \rho_n \\ \sum_{i=0}^{3} F_i \left(\frac{\rho}{\rho_e} - 1 \right)^i & \rho_n \leq \rho < \rho_0 \\ F_e \left[1 - \ln \left(\frac{\rho}{\rho_s} \right)^\eta \right] \left(\frac{\rho}{\rho_s} \right)^\eta & \rho_0 \leq \rho \end{cases}, \tag{D.15}$$

where $\rho_n = 0.85\rho_e$ and $\rho_0 = 1.15\rho_e$. The derivative of the embedding energy function is given by

$$\frac{\partial F}{\partial \rho}(\rho) = \begin{cases} \sum_{i=1}^{3} i \frac{F_{ni}}{\rho_n} \left(\frac{\rho}{\rho_n} - 1 \right)^{i-1} & \rho < \rho_n \\ \sum_{i=0}^{3} i \frac{F_i}{\rho_e} \left(\frac{\rho}{\rho_e} - 1 \right)^{i-1} & \rho_n \leq \rho < \rho_0 \\ \eta \frac{F_e}{\rho} \left[1 - \eta \ln \left(\frac{\rho}{\rho_s} \right) \right] \left(\frac{\rho}{\rho_s} \right)^\eta - \eta \frac{F_e}{\rho} \left(\frac{\rho}{\rho_s} \right)^\eta & \rho_0 \leq \rho \end{cases}. \tag{D.16}$$

Finally, there are twenty material parameters.

Table D.2 shows the material parameters of the EAM-Wadley for copper [101].

Parameter		Valiue	Parameter		Value
r_e	$[\mathring{A}]$	2.556162	f_e		1.554485
ρ_e		21.175871	ρ_s		21.175395
α		8.127620	β		4.334731
A	$[eV]$	0.396620	B	$[eV]$	0.548085
κ		0.308782	λ		0.756515
F_{n0}	$[eV]$	-2.170269	F_{n1}	$[eV]$	-0.263788
F_{n2}	$[eV]$	1.088878	F_{n3}	$[eV]$	-0.817603
F_0	$[eV]$	-2.19	F_1	$[eV]$	0.0
F_2	$[eV]$	0.561830	F_3	$[eV]$	-2.100595
η		0.310490	F_e	$[eV]$	-2.186568

Table D.2: The material parameters of the EAM-Wadley for copper [101].

Figure D.4, D.5 and D.6 show the pairwise interaction, electron density and embedding energy function of copper for the EAM-Wadley.

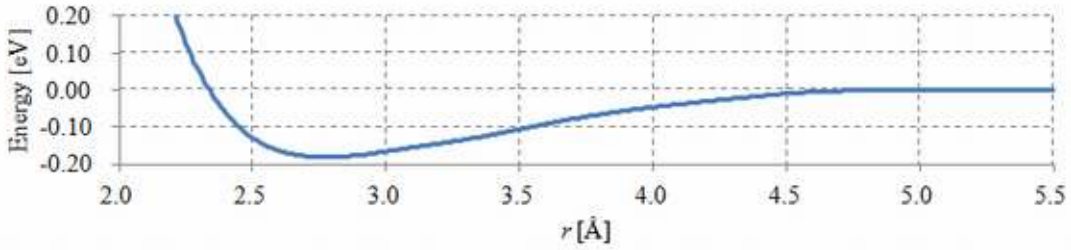

Figure D.4: The pairwise interaction function of copper for the EAM-Wadley.

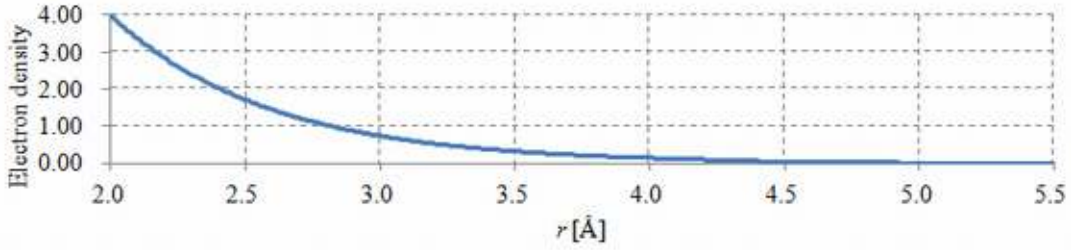

Figure D.5: The electron density function of copper for the EAM-Wadley.

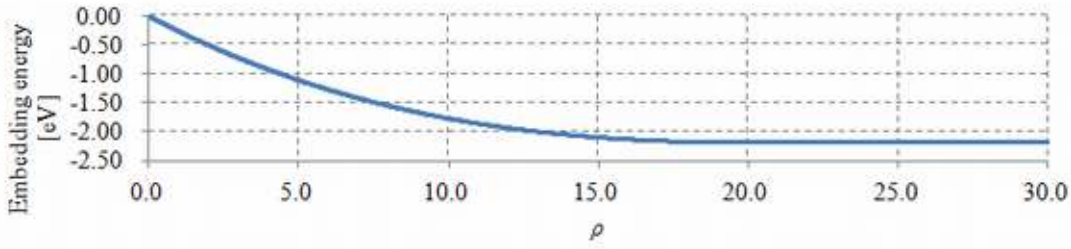

Figure D.6: The embedding energy function of copper for the EAM-Wadley.

D.3 The Embedded Atom Method: Holian et al. Model

In this section, the Embedded Atom Method developed by Holian et al. [38], [39], [94] is introduced. This method is called EAM-Holian in this dissertation.

The pairwise interaction function has the cutoff form,

$$\phi(r) = \begin{cases} \chi\psi(r) & r < r_{spl} \\ \chi\left\{\psi(r_{spl}) + \dfrac{\partial\psi}{\partial r}(r_{spl})(r - r_{spl}) - \dfrac{1}{6}A(r - r_{spl})^3\right\} & r_{spl} \le r < r_{max} \\ 0 & r_{max} \le r \end{cases}, \quad \text{(D.17)}$$

where χ is a weighting parameter between zero and one, the parameter value $\chi = 1/3$ is taken for the Embedded Atom Method, r_{spl} is the inflection point in the potential, r_{max} is the cutoff distance,

$$\psi(r) = \epsilon\left\{\left(\frac{r_0}{r}\right)^{12} - 2\left(\frac{r_0}{r}\right)^{6}\right\}, \quad \text{(D.18)}$$

and

$$A = \frac{8\left(\dfrac{\partial\psi}{\partial r}(r_{spl})\right)^3}{9\left(\psi(r_{spl})\right)^2}, \quad \text{(D.19)}$$

where ϵ is the depth of the potential well, r_0 is the equilibrium distance. The inflection point r_{spl} can be obtained by

$$\frac{\partial^2\psi}{\partial r^2}(r_{spl}) = 0, \quad \text{(D.20)}$$

and the value is $r_{spl} = 1.244455r_0$. The cutoff distance is given by

$$r_{max} = r_{spl} - \frac{3\psi(r_{spl})}{2\frac{\partial\psi}{\partial r}(r_{spl})}, \quad \text{(D.21)}$$

and the value is $r_{max} = 1.547537r_0$. For $r < r_{spl}$, the pairwise interaction function is the exactly same as the Lennard-Jones potential, and the intermediate-range cubic spline [39] for $r_{spl} \le r \le r_{max}$. The derivative of the pairwise interaction function is

$$\phi(r) = \begin{cases} \chi\dfrac{\partial\psi}{\partial r}(r) & r < r_{spl} \\ \chi\left\{\dfrac{\partial\psi}{\partial r}(r_{spl}) - \dfrac{1}{2}A(r - r_{spl})^2\right\} & r_{spl} \le r < r_{max} \\ 0 & r_{max} \le r \end{cases}, \quad \text{(D.22)}$$

where

$$\frac{\partial\psi}{\partial r}(r) = -12\frac{\epsilon}{r}\left\{\left(\frac{r_0}{r}\right)^{12} - \left(\frac{r_0}{r}\right)^{6}\right\}. \quad \text{(D.23)}$$

The electron density function is given by

$$\rho(r) = \begin{cases} \dfrac{1}{d(d+1)} \left(\dfrac{r_{max}^2 - r^2}{r_{max}^2 - r_0^2} \right)^2 & r < r_{max} \\ 0 & r_{max} \leq r \end{cases}, \tag{D.24}$$

where d is the dimensionality. The derivative of the electron density is given by

$$\frac{\partial \rho}{\partial r}(r) = \begin{cases} -\dfrac{4}{d(d+1)} \dfrac{r\left(r_{max}^2 - r^2\right)}{\left(r_{max}^2 - r_0^2\right)^2} & r < r_{max} \\ 0 & r_{max} \leq r \end{cases}. \tag{D.25}$$

The embedding energy function is chosen to be a nonlinear function of the form,

$$F(\rho) = (1-\chi)\,\epsilon \frac{d(d+1)}{2} e\rho \ln \rho, \tag{D.26}$$

where e is the base of the natural logarithms. Clearly, at normal density, where the local embedding energy is $\rho = 1/e$, the embedding energy contributes a fraction $1-\chi$ to the total cohesive energy. The derivative of the embedding energy function is given by

$$\frac{\partial F}{\partial \rho}(\rho) = (1-\chi)\,\epsilon \frac{d(d+1)}{2} e\,(\ln \rho + 1)\,. \tag{D.27}$$

Finally, there are only two material parameters, the depth of the potential well ϵ and the equilibrium distance r_0. These parameters are not shown in references and are obtained by following way in this dissertation. First, the equilibrium distance r_0 is determined as $\boldsymbol{\sigma} = \mathbf{0}$ when there is no deformation, $\mathbf{F} = \mathbf{I}$. The Cauchy stress is computed from the Cauchy-Born rule. In this calculation, ϵ is taken to be unity, $\epsilon = 1$, and up to the third nearest neighbors on FCC lattice are considered. Second, the depth of the potential well ϵ is obtained by least squares method,

$$\left(C_{1111}^{exp} - \epsilon C_{1111}^{CB}\right)^2 + \left(C_{1122}^{exp} - \epsilon C_{1122}^{CB}\right)^2 + \left(C_{1212}^{exp} - \epsilon C_{1212}^{CB}\right)^2 = Min, \tag{D.28}$$

where C_{1111}^{exp}, C_{112}^{exp} and C_{1212}^{exp} are the experimental values, and C_{1111}^{CB}, C_{112}^{CB} and C_{1212}^{CB} are obtained from the Cauchy-Born rule. By taking the derivative with respect to ϵ, we have

$$\epsilon = \frac{C_{1111}^{exp} C_{1111}^{CB} + C_{1122}^{exp} C_{1122}^{CB} + C_{1212}^{exp} C_{1212}^{CB}}{\left(C_{1111}^{CB}\right)^2 + \left(C_{1122}^{CB}\right)^2 + \left(C_{1212}^{CB}\right)^2}. \tag{D.29}$$

Table D.3 shows the fitting results and the material parameters. The experimental data are obtained from [12].

Figure D.7, D.8 and D.9 show the pairwise interaction, electron density and embedding energy function of copper for the EAM-Holian.

	Parameter		Experiment	EAM-Holian
Cu	C_{1111}	$[GPa]$	169	168.2
	C_{1122}	$[GPa]$	122	117.5
	C_{1212}	$[GPa]$	75.3	83.2
	ϵ	$[eV]$		0.43894774
	r_0	$[\mathring{A}]$		2.57110688
Ag	C_{1111}	$[GPa]$	123	121.0
	C_{1122}	$[GPa]$	92	84.5
	C_{1212}	$[GPa]$	45.3	59.8
	ϵ	$[eV]$		0.45921505
	r_0	$[\mathring{A}]$		2.91297151
Al	C_{1111}	$[GPa]$	108	95.4
	C_{1122}	$[GPa]$	62	66.7
	C_{1212}	$[GPa]$	28.3	47.2
	ϵ	$[eV]$		0.35153936
	r_0	$[\mathring{A}]$		2.88448279
Au	C_{1111}	$[GPa]$	190	186.7
	C_{1122}	$[GPa]$	161	130.4
	C_{1212}	$[GPa]$	42.3	92.3
	ϵ	$[eV]$		0.70311064
	r_0	$[\mathring{A}]$		2.90584933
Ni	C_{1111}	$[GPa]$	247	239.1
	C_{1122}	$[GPa]$	153	167.0
	C_{1212}	$[GPa]$	122	119.2
	ϵ	$[eV]$		0.58932496
	r_0	$[\mathring{A}]$		2.47623650

Table D.3: The material parameters of the EAM-Holian. The experimental data are obtained from [12].

.

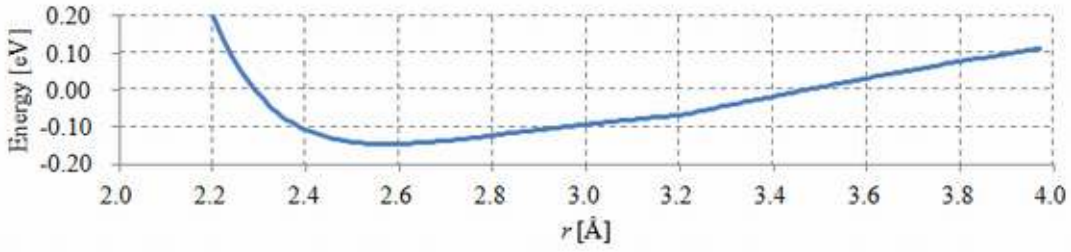

Figure D.7: The pairwise interaction function of copper for the EAM-Holian.

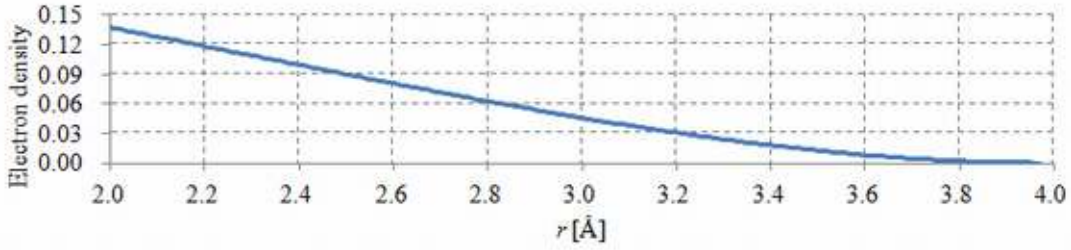

Figure D.8: The electron density function of copper for the EAM-Holian.

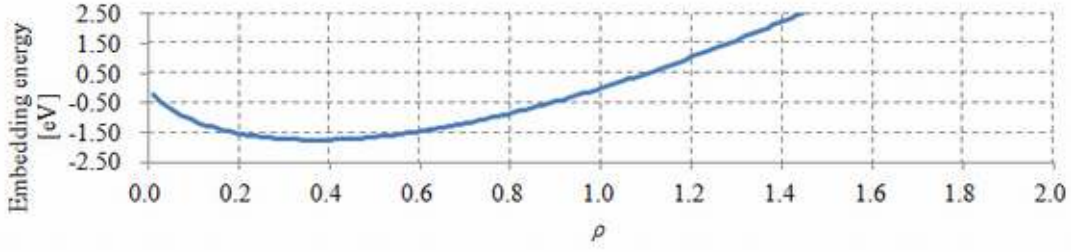

Figure D.9: The embedding energy function of copper for the EAM-Holian.

Appendix E

Analytical Solutions of Capillary Rise

Figure E.1 shows that plane Poiseuille flow between parallel walls. The Navier-Stokes

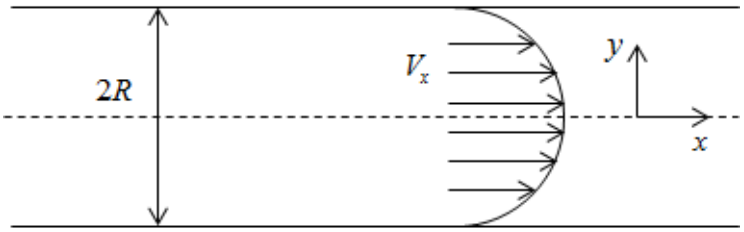

Figure E.1: Plane Poiseuille flow between parallel walls.

equation in x direction is given by

$$\frac{\partial V_x}{\partial t} + V_x \frac{\partial V_x}{\partial x} + V_y \frac{\partial V_x}{\partial y} = -\frac{\partial p}{\partial x} + \mu \left(\frac{\partial^2 V_x}{\partial x^2} + \frac{\partial^2 V_x}{\partial y^2} \right), \tag{E.1}$$

where V_x and V_y are the velocity in x and y direction respectively, p is the pressure, and μ is the dynamic viscosity of a fluid.

Here, assume steady flow, i.e. $\frac{\partial V_x}{\partial t} = 0$, $\frac{\partial V_x}{\partial x} = 0$, and $V_y = 0$. Then, the Navier-Stokes equation can be simplified to

$$\frac{\partial^2 V_x}{\partial y^2} = \frac{1}{\mu} \frac{dp}{dx}, \tag{E.2}$$

where $\frac{\partial p}{\partial x}$ is replaced by $\frac{dp}{dx}$ since pressure is distributed only in x direction. By taking the integral with respect to y and applying the boundary condition, i.e.

$$\frac{\partial V_x}{\partial y} = 0 \quad at \quad y = 0, \tag{E.3}$$

and

$$V_x = 0 \quad at \quad y = \pm R. \tag{E.4}$$

The velocity distribution is obtained by

$$V_x = \frac{1}{2\mu}\frac{dp}{dx}\left(y^2 - R^2\right). \tag{E.5}$$

The volumetric flow rate Q is obtained by integrating the velocity distribution,

$$Q = \int_{-R}^{R} V_x dy \tag{E.6}$$

$$= -\frac{2}{3\mu}\frac{dp}{dx}R^3. \tag{E.7}$$

The volumetric flow rate is defined by the cross sectional area times velocity,

$$Q = 2Rh', \tag{E.8}$$

where h' is the velocity. Pressure can be obtained by substituting Equation (E.8) into (E.7),

$$\frac{dp}{dx} = -\frac{3\mu}{R^2}h', \tag{E.9}$$

and

$$p = -\frac{3\mu}{R^2}hh', \tag{E.10}$$

where $\frac{dp}{dx}$ is approximated by

$$\frac{dp}{dx} \approx \frac{p}{h}, \tag{E.11}$$

and h is the displacement in x direction.

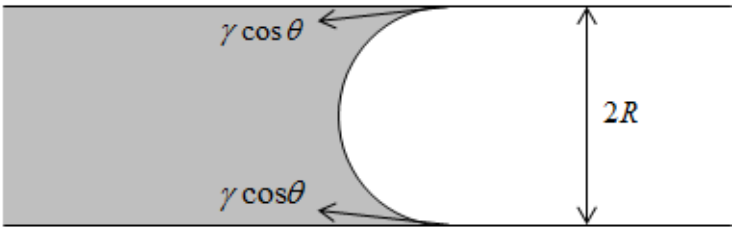

Figure E.2: Illustration of capillary rise between parallel walls.

There is the surface tension γ at the contact line, and the force in x direction is given by $2\gamma\cos\theta$, where θ is the contact angle. The pressure is the force divided by the area $2R$,

$$p = \frac{\gamma\cos\theta}{R}. \tag{E.12}$$

Since Equation (E.10) and (E.12) are balanced, the balance equation is

$$\frac{3\mu}{R^2} h h' = \frac{\gamma \cos\theta}{R} \tag{E.13}$$

$$h = \sqrt{\frac{2R\gamma \cos\theta}{3\mu} t}. \tag{E.14}$$

This is the analytical solution of capillary rise between parallel walls. The analytical solution of capillary rise in a tube is known as Lucas-Washburn equation [53], [96],

$$h = \sqrt{\frac{R\gamma \cos\theta}{2\mu} t}. \tag{E.15}$$

Both Equation (E.14) and (E.15) state capillary rise h is in proportion to the square root of time, and the factor of proportionality depends on only the radius, surface tension, contact angle and viscosity.